RESEARCH ARTICLE

Adsorption of CI Basic Blue 3 Dye Molecules from Aqueous Media by Sulfuric Acid-Activated Montmorillonite Mineral

This article was produced from a poster or oral contribution to the ICAIE Congress, 2017.

Şeyda TAŞAR[1,*], Fatih KAYA[1], Ahmet ÖZER[1]

[1] Department of Chemical Engineering, Firat University, Elazig/Turkey

Abstract: Many industries (especially textile, paper, plastic) which use chemicals and colorants, generate considerable amount of waste water since they use excessive amounts of water in their operations. and they These waste waters form a significant reason of worldwide water pollution, and if they are released before being treated, they bring an important harm to these waters. Therefore, In this paper, adsorption kinetics and equilibrium of CI Basic Blue 3 (BB3) from aqueous media using sulfuric acid-activated montmorillonite mineral (SAM) was investigated. For this aim, firstly the natural montmorillonite mineral (NM) was activated by treating with a 6 M H_2SO_4 solution for 4 hours at 395 K. After sulfuric acid treatment the SAM samples were characterized using a BET surface analyzer and FTIR spectroscopy. The adsorption experiments in different conditions such as i.e., contact times (0-120 min), initial pH values (2-8), temperatures (298-318 K), and initial dye concentrations (100-350 mg/l) were performed in a thermostatic water bath at an agitation speed of 180 rpm. The experimental maximum adsorption capacity (q_e) was determined to be 277 mg/g at 60 min, 6 ± 0.02, 298 K and 350 ppm initial dye concentration. For adsorption of CI Basic Blue 3 (BB3) molecules from aqueous media by the sulfuric acid activated montmorillonite mineral (SAM) is determined that Lagergren's kinetic model (pseudo first order) simulated the kinetic data better than the Ho's kinetic model (pseudo second order) and the Freundlich isotherm is the best fitting isotherm model equation. Also, the thermodynamic parameters calculated using Van't Hoff equation show that the adsorption process is spontaneous and exothermic. The experimental results of the study indicated that, the acid activated mineral is suitable for adsorption of BB3 dye molecules from aqueous media.

Keywords: Adsorption, CI Basic Blue 3, sulfuric acid-activated montmorillonite mineral (SAM), thermodynamic and kinetic parameters

Cite This: Taşar Ş, Kaya F, Özer A. Adsorption of CI Basic Blue 3 Dye Molecules from Aqueous Media by Sulfuric Acid-Activated Montmorillonite Mineral. JOTSCB. 2017;1(Sp. is. 1):1–16.

*Corresponding author. E-mail: sydtasar@firat.edu.tr.

INTRODUCTION

Color removal from wastewaters is an important environmental aspect in textile industry. which is one of the fastest-growing major industries in Turkey. The wastewaters released from this industry contain high amounts of dyes and pigments, which generally have been synthesized and contain complex aromatic molecules. They contain a lot of double bonds and various functional groups (1). Therefore these dyes and pigments are not biologically decomposed due to their stable structures, so they accumulate easily in natural bodies of water (2). When these wastewaters are discharged into aquatic media, serious environmental problems may be occurred such as impairment of the aesthetic nature, the reduction of the degree of penetration of light and decrease in the solubility of gases (3). These wastewaters can cause a variety of health problems such as skin irritations, allergic reactions and cancer on the living beings. (2–4). For these reasons, the removal of dye materials and pigments from waste water is important with respect to the protection of the health of the ecosystem and the living organisms that may be exposed to these wastewaters. Colored wastewater is known as one of the most difficult wastewater to be improved because of the present disadvantages expressed. Treatment difficulties are based on stability of recalcitrant dyes and their ability to bestow good coloring in very low concentrations. Many treatment techniques can be used for the removal of these pigments and dyes from colored wastewater before they are discharged to aquatic media. These techniques include adsorption (5–11), membrane processes (12), oxidation processes (13), ion exchange (7,8), reverse osmosis (14), electrocoagulation (2), and coagulation (15). Unlike other remediation techniques, because of simplicity, ease of use and high efficiency, adsorption process is considered one of the most attractive treatment options for the removal of the dye and pigments from the wastewater (16–18). It is known that the cost, sustainable resource, accessibility and adsorptive capacity of the adsorbent are very significant parameters that affect the efficiency, effectiveness, and costs of the process.

The aim of this research was to investigate the adsorption of CI Basic Blue 3 (BB3) from aqueous media by sulfuric acid-activated montmorillonite mineral (SAM). To do this, the SAM samples were firstly produced from natural montmorillonite mineral and characterized with FTIR and BET techniques. Secondly, the effects of the efficiency and rate of adsorption of BB3 on the SAM samples were studied in a batch system. Then the kinetic and thermodynamic parameters were calculated using experimental data and appropriate models equations.

MATERIAL AND METODS

Preparation and characterization of adsorbent

CI Basic Blue 3 dye molecules was provided from Sigma Aldrich and used in experiments without any purification. The molecule structure of BB3 and some specific properties were given Table 1 and Fig. 1.

The natural montmorillonite mineral (NAM) which was supplied by a local industry in Elazig/Turkey, The natural montmorillonite mineral was dried firstly under atmospheric condition, then at 105 ℃ in an oven and then divided into fractions based on the particle sizes. The fraction between 50 and 100 mesh was activated using 6 M H_2SO_4 solution at 97 ºC for 6 hr. And then sulphuric-activated montmorillonite mineral (SAM) which was washed with water until the sulphate ions were completely removed, were dried after the washing in an over same temperature and the samples stored in desiccators for subsequent use in the study.

BET Surface Area Analyzer (ASAP 2020, Micromeritics Inc., USA) and FTIR spectrometer (ATI Unicam Mattson 1000) were used to characterized of SAM samples. Besides, to the same aim, the pH of zero point of charge (pH_{zpc}) of the activated montmorillonite mineral was measured by using the pH drift methods (19,20).

Table 1: Computed properties of BB3.

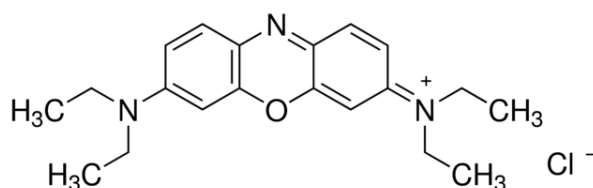| Empirical Formula	Molecular Weight	λ_{max}	composition
$C_{20}H_{26}ClN_3O$	359.89	654 nm	Dye content, 25%

Figure 1: 2D structure of BB3.

Experimental Procedure

The dye stock solution of CI Basic Blue 3 (BB3) was prepared from 25 % dye content, Sigma Aldrich in a concentration of 1000 mg/L. During the experimental studies, all working dilute solutions were prepared using the stock solution and distilled water. The pH values of the dilute working solutions which were used in the experiment, were adjusted using 0.1 M solutions of NaOH and HCl especially in studies in which the effects of pH were investigated.

3

The experiments were performed in 14 parallel erlenmeyer flasks using a thermostatic water bath at an agitation speed of 180 rpm. The effect of various parameters such as initial pH (2-8), contact time (5-120 min), temperature (298-318 K), and initial concentration of BB3 (100-350 ppm) on adsorption yield was investigated in the study. All of the experiment series were conducted by mixing 50 mL of the BB3 solution with a certain amount of SAM in 100-mL erlenmeyer flasks which were prepared in the same conditions. At the end of the planned contact time of experiment each flask was removed from the water bath and the SAM particles were separated from the aqueous phase by centrifugation at 5000 rpm for three minutes. To calculate the adsorption yield and capacity of adsorption, the final concentration of BB3 in the filtrate was determined with analyzed by a UV-Vis spectrophotometer. All the experiments series were performed in duplicate, and the average results were reported. According to experimental results and working line, the adsorption efficiency and capacity of adsorption were calculated using Eqs. (1) and Eqs (2).

$$Adsorption\ efficiency(\%) = \frac{C_o - C_e}{C_o} \times 100 \qquad \text{(Eq. 1)}$$

$$q_e = \frac{v \times (C_o - C_e)}{m}, \qquad \text{(Eq. 2)}$$

Where q_t (mg/g) is the amount of BB3 molecules per mass unit of SAM at t = t. C_0, C_t and C_e (mg/L) are the initial, at time t and final (equilibrium) concentration of BB3 molecules, respectively. m (g) is the mass of SAM and V is the volume of the BB3 solution (L)

RESULT AND DISCUSSION

Characterization Results of the Adsorbent

The average pore diameter and BET surface area were determined by the nitrogen adsorption method as 21.2 Å and 113.3 m^2/g for the sulfuric acid-activated montmorillonite mineral (SAM). Same quantities for the natural montmorillonite mineral (NM), were obtained as 65.4 Å and 73.6 m^2/g.

The functional groups on the surface of montmorillonite mineral before and after activation process were identified using the Fourier transform infrared (FTIR) spectroscopy. Wavenumber and vibration type of the significant peaks of the samples are given in Table 2. Liu *et al*. and Öztürk *et al*. in their researches (21,22) have reported similar peaks and assignment for other clay mineral.

Table 2: FTIR spectral data of the SAM and NM.

Frequency (cm^{-1})		Assignment
Acid-activated montmorillonite mineral (SAM)	Natural Montmorillonite mineral (NAM)	
433	-	Si–O deformation
469	469	Si–O–Si deformation
525	530	Al–O–Si deformation
690	690	Si–O perpendicular
794	-	Si–O
1013	-	In-plane Si–O stretching
1074	1043	Si–O stretching
-	1262	C-H bending
1415	1420	Aromatic methyl (-CH_3) group vibrations
-	1516	C=C stretching vibrations of aromatic ring
1639	1633	OH deformation of water
-	2930	Aliphatic C-H stretching
3435	3403	OH stretching of inner hydroxyl groups
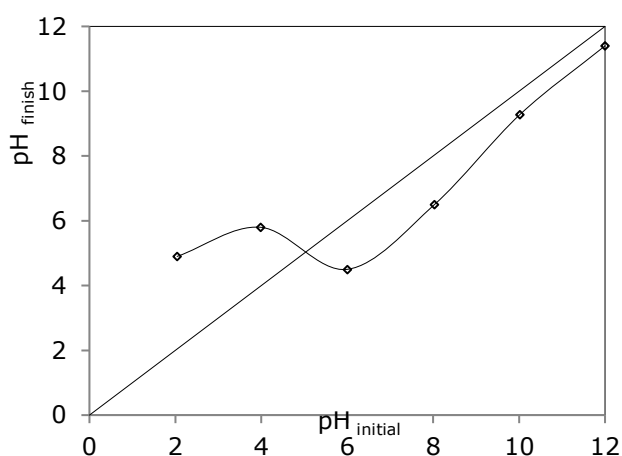
Figure 2: The point of zero charge of SAM.

It is well known that the point of zero charge (pH_{zpc}), which is indicative of the types of surface active centers and the adsorption mobility of surface, is an important factor in adsorption processes (23). Fig.2, which was drawn using the drift method, shows that the value of pH_{zpc} was 5.1. The experimental results indicated that, when the pH of the BB3 solution was less than 5.1, the surface of the SAM was positively charged and could attract anions from the solution.

When the pH of the solution was greater than 5.1, the surface of the SAM was negatively charged and attracted cations.

Effect of The Initial pH of The BB3 Dye Solution Depending on The Contact Time

Figure 3 shows the relationship between initial pH values of BB3 dye solutions and adsorption capacity, depending on the duration of contact. Figure 3 shows that the adsorption of the BB3 molecules was very high in the first 30 min. After that period, the adsorption efficiency declined because the active sites on the surface area available for adsorption was decreased. Also, the high adsorption efficiency during the initial stage have been due to the higher driving force's producing faster transfer of BB3 molecules to the surface of the SAM.
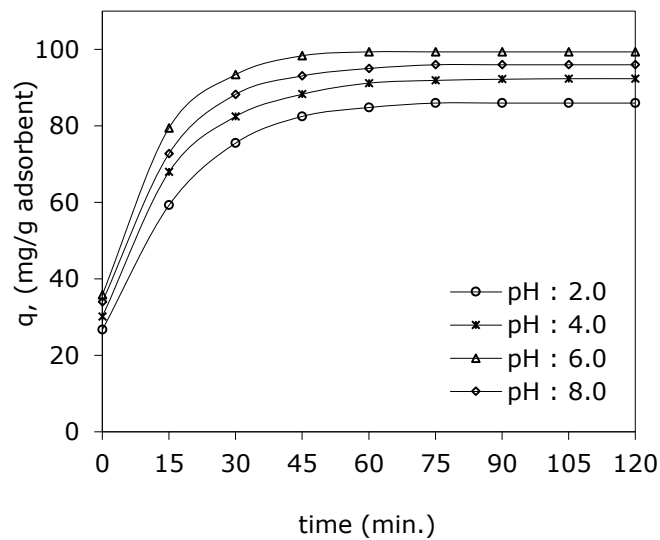

Figure 3: Effect of contact time on adsorption capacity of SAM (initial BB3 conc. 100 ppm; contact time: 120 min; SAM conc. 2 g/L; temperature: 298 K)

In addition, the adsorption capacity of the SAM increased with contact time and reached its maximum value in the range of 85-99 mg/g for different initial pH values after approximately 60 min. After this time, the adsorption capacity remained almost constant, for that reason contact time of 60 min was considered the equilibrium time for BB3 adsorption. It can be observed that the adsorption capacity of SAM increased linearly up to pH 6, reaching a maximum value (99 mg/g) at pH 6 (Figure 4). After that point, the adsorption capacity decreased. It was concluded that the results obtained were in accordance with previous studies and the result that the initial pH of the dye solution affected the concentration of counter ions in the functional groups of SAM, the surface charge of SAM and the degree of dissociation /ionization of SAM during adsorption process (24–26). These results are consistent with the pH_{zpc} value of the SAM samples (pH_{zpc} = 5.1). Vijayaraghavan *et al.* (27) have reported similar results in their research.
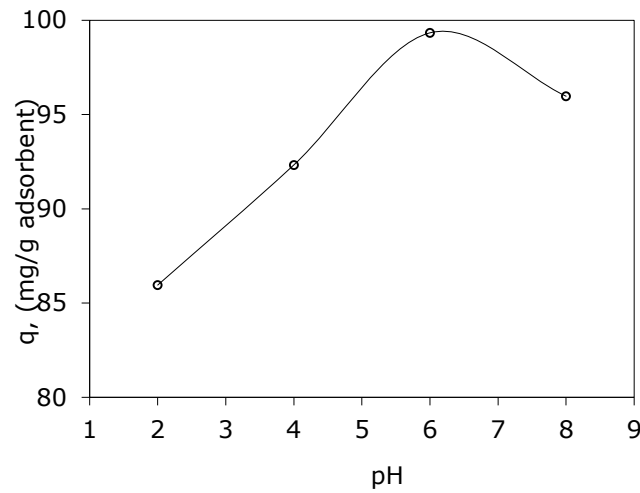
Figure 4: Effect of initial pH on adsorption capacity of SAM (initial BB3 con. 100 ppm; contact time: 120 min; SAM con: 2 g/L; temperature: 298 K)

The Kinetic Analysis of the Adsorption

The effect of the temperature on the adsorption of BB3 molecules by SAM in is shown in Figure 5. It was observed that the adsorptive capacity of the SAM was increased as the temperature decreased from 318 K to 298 K. The equilibrium adsorption capacity of the SAM was determined to be about 97 and 89 mg BB3/g at 298 and 318 K, respectively. The increase in the removal of BB3 with decrease in temperature of solution showed that the adsorption process was exothermic.
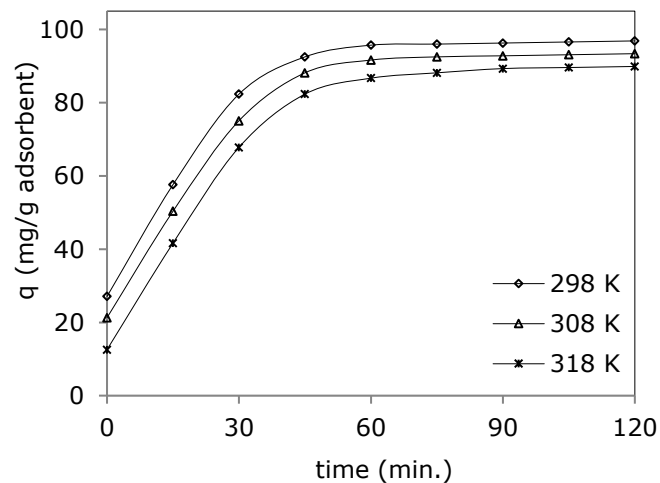

Figure 5: Effect of temperature on adsorption capacity of SAM (initial BB3 con. 100 ppm; contact time: 120 min; SAM con: 2 g/L; pH: 6±0.02)

Adsorption processes are time dependent; therefore, while designing the reactor for this process, the relationship between the adsorption rate and the contact time should be known. This relationship can be demonstrated by kinetic model equations. For that reason, the adsorption rate constants were calculated with pseudo first-order (Lagergren (28)) and pseudo second-order (Ho (29)) kinetic models, which can be used to describe the mechanism of the BB3 dye molecules adsorption.

7

The pseudo-first order equation of Lagergren is generally expressed in equation (3):

$$\frac{dq_t}{dt} = k_1(q_e - q_t)$$
(Eq. 3)

if equation 4 is integrated (t =0 to t =t and q_t =0 to q_t =q_t)

$$q_t = q_e(1 - e^{-k_1 t})$$
(Eq. 4)

if the equation(4) is transformed into a linear form to provide ease of use in kinetic data,

$$\ln(q_e - q_t) = \ln q_e - k_1 t$$
(Eq. 5)

The pseudo second-order model is given by Eq. (6):

$$\frac{dq_t}{dt} = k_2(q_e - q_t)^2$$
(Eq. 6)

If the Eq. (5) is integrated, then Eq (7) is obtained.

$$\frac{t}{q_t} = \frac{1}{k_2 q_e^2} + \frac{t}{q_e},$$
(Eq. 7)

Where; t (min) is the contact time of adsorbate (BB3) and adsorbent (SAM); k_1 (min^{-1}), Lagergren adsorption rate constant, k_2 (g/mg^{-1}.min^{-1}) second order adsorption rate constant, q_e (mg/g)amount of dye absorbed in equilibrium, qt (mg/g) amount of dye absorbed at t=t time.

If the y values in equations are ln (q_e-q_t) or t/q_t plotted against x value t , k_1, k_2 and q_e values can be found, respectively. (Fig. 6 and 7).

The values of k_1, q_{ec1}, k_2, q_{ec2}, and the correlation coefficient (R^2) are given in Table 3. The correlation coefficient (R^2) and the difference between the calculated adsorption capacity (q_{ec}) and the experimental adsorption capacity (q_e) indicate that the Lagergren's kinetic model (pseudo first order) simulated the kinetic data better than the Ho's kinetic model (pseudo second order).
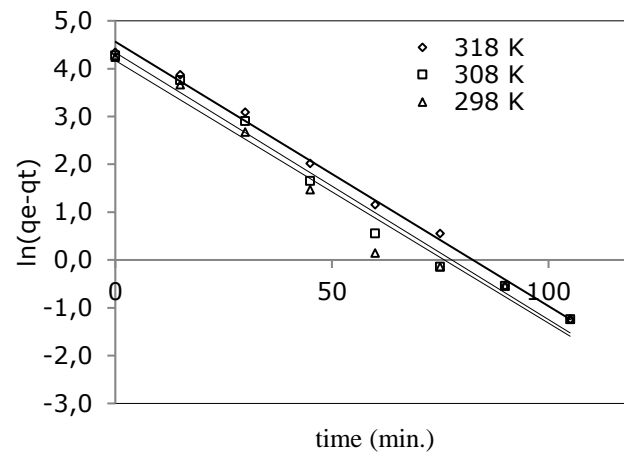
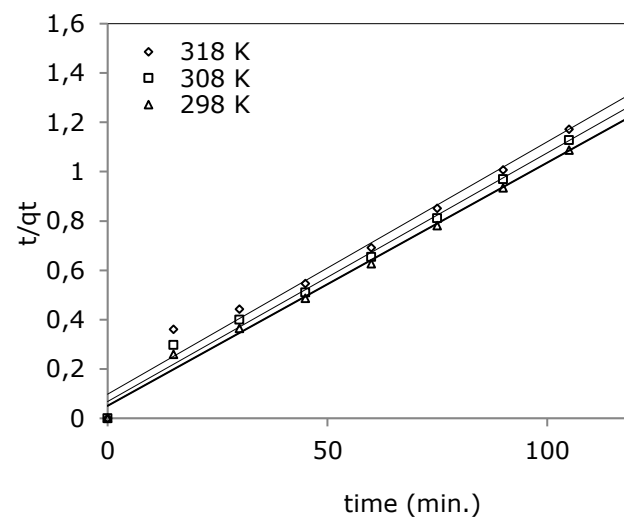**Figure 6:** Pseudo first-order kinetic plots for the removal of BB3 molecules

Figure 7: Pseudo second-order kinetic plots for the removal of BB3 molecules

Table 3: Kinetic constants of Lagergren and Ho models for the removal of BB3 by SAM

Temperature (K)	q_e (mg/g)	Pseudo-first-order (Lagergren) kinetic model		
		R^2	$k_1 \times 10^3$ (min⁻¹)	q_{ec1} (mg/g)
298	99.3	0.97	54.9	64.71
308	93.4	0.98	55.8	76.71
318	89.8	0.99	55.3	95.85
Temperature (K)	q_e (mg/g)	Pseudo-second-order (Ho) kinetic model		
		R^2	$k_2 \times 10^3$ (g/mg min)	q_{ec2} (mg/g)
298	99.3	0.99	1.1	101.0
308	93.4	0.99	1.5	99.00
318	89.8	0.98	1.9	98.04

Thus, the activation energy of the adsorption process of BB3 molecules by the SAM was calculated using the rate constants (k_2) and the Arrhenius equation (Eq. 8).

$$\ln k_2 = \ln A - \frac{E_a}{RT}$$
(Eq. 8)

Where Ea (J/mol), A (g/mg min), R (8.314 J/mol K) and T (K) are the activation energy, the Arrhenius constant, the ideal gas constant and the temperature of the solution, respectively.

The activation energy value (E_a) was calculated as about 19 kJ/mol, and this value indicated that physical adsorption is a dominate mechanisms on the removal process. On the other hand, it was observed that the values of q_{ec2} increased and the values of k_2 decreased with decrease in temperature. These results indicated that the adsorption of BB3 by the SAM occurred more rapidly at higher temperatures.

Thermodynamic Analysis of Adsorption

According to experimental results, the adsorptive capacity of the SAM was a function of the initial concentration of BB3 molecules in the aqueous solution. It was observed that the the adsorption capacity of BB3 increased from 130 to 180 mg/g at the range of initial concentrations values between 100 to 350 mg/L due to the fact that the initial dye concentration is an important driving force to overcome mass transfer resistance. Özer *et al.* (30) have reported similar results their paper. When the temperature of the solution decreased from 318 to 298 K, the value of the maximum adsorption capacity increased from approximately 89.8 to 99.3 mg/g for 100 ppm and 210 to 280 mg/g for 350 ppm. The decrease of efficiency and capacity of adsorption with the temperature increases shows that the adsorption process is exothermic and the adsorption is applicable at low temperature efficiently. this result is the result of weak interaction forces such as van der Waals and hydrogen bonds between dye molecules and adsorbent. Vimoneses et al (31), Toor et al (32) have given similar results and comments for their work.

The equilibrium adsorption isotherm is fundamentally important in the design of an adsorption system. Therefore, an adsorption isotherm study was carried out on Langmuir (33) and Freundlich (34) isotherm models.

The Langmuir isotherm is given by Eq. (9):

$$\frac{C_e}{(x/m)} = \frac{1}{q_{max}K} + \frac{C_e}{q_{max}}$$
(Eq. 9)

Where K (L/mg) is the Langmuir constant. C_e (mg/L) is the equilibrium concentration of BB3. q_e ($\frac{x}{m}$) (mg/g) and q_{max} are the adsorptive and maximum adsorption capacity of the SAM.

The Freundlich isotherm is given by Eq. (10):

$$x/m = K_f C_e^{1/n}$$
(Eq. 10)

if the equation (10) is transformed into a linear form:

$$\ln(x/m) = \ln K_f + \frac{1}{n}\ln C_e$$　　　　　　(Eq. 11)

Where n is the intensity of adsorption, and K_f (mg/g) is the adsorptive capacity.

The adsorption data were analyzed with the Freundlich and Langmuir sorption models. Figs. 8 and 9 show the Langmuir and Freundlich isotherm plots, respectively. The parameters of isotherm models equations and constant are given in Table 4.
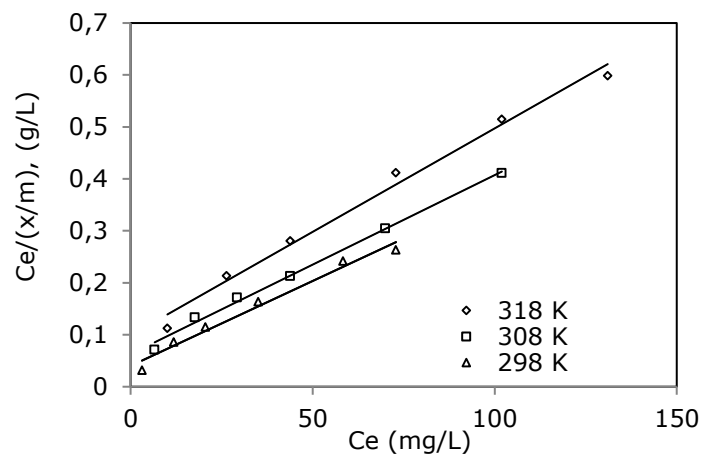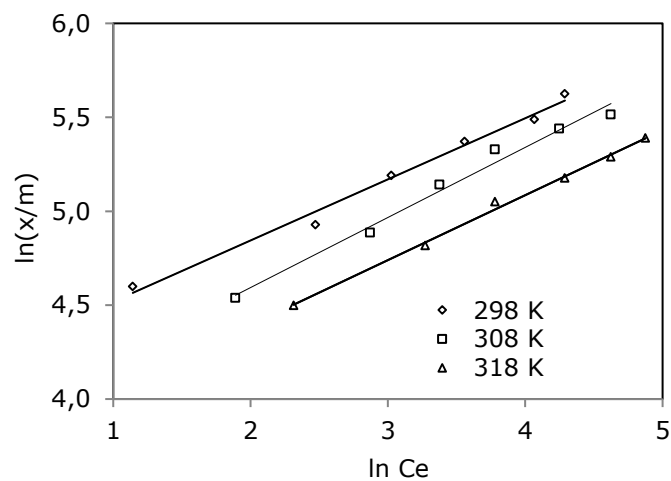
Figure 8: Langmuir isotherm.

Figure 9: Freundlich isotherm.

Table 4: Parameters of investigated isotherms of BB3 molecules adsorption onto SAM.

Temperature K	Langmuir Constants		
	q_{max} (mg/g)	K (L/mg)	R^2
298	303.0	0.081	0.979
308	294.1	0.054	0.985
318	250.0	0.040	0.989
Temperature K	Freundlich Constants		
	K_f (mg/g)(L/mg)^n	n	R^2
298	64.53	3.00	0.991
308	46.86	2.68	0.984
318	40.56	2.89	0.996

It was found that the adsorption of BB3 onto SAM was described better by the Freundlich isotherm than Langmuir isotherm model. The relationship between temperature and the adsorption equilibrium constant, called van't Hoff equation, is given as:

$$\frac{d(\ln K)}{dT} = \frac{\Delta H^o}{RT^2} \tag{Eq. 12}$$

An integrated form of the van't Hoff equation is presented in Eq. (13):

$$-\ln K = \frac{\Delta H^o}{R}\left(\frac{1}{T}\right) + C \tag{Eq. 13}$$

Eq. (14) is obtained when the constant is replaced by
(-ΔS⁰/R):

$$\ln K = \frac{\Delta S^o}{R} - \frac{\Delta H^o}{R}\left(\frac{1}{T}\right) \tag{Eq. 14}$$

If ΔG⁰ = -RTlnK is combined with Eq. (14) the following equation is obtained:

$$\Delta G^o = \Delta H^o - T\Delta S^o \tag{Eq. 15}$$

Where ΔS⁰, ΔH⁰ and ΔG⁰, are changes in free entropy, changes in free enthalpy and changes in Gibbs free energy, respectively. K is the adsorption equilibrium constant; T (K) is absolute temperature. and R (8.314 J/mol K) is the universal gas constant. The intercept and the slope of the plots of lnK versus 1/T were used to determine the values of ΔS⁰ and ΔH⁰.

The thermodynamic parameters were calculated for the process. The change of free energy (ΔG⁰) was calculated as -21.27 for 298 K, -21.05 for 308 K and -20.80 kJ/mol for, 318 K, respectively by using Eq.(14). The change in entropy (ΔS⁰) and enthalpy (Δ*H*⁰) were determined to be 21.86 J/mol K and -27.78 kJ/mol, respectively. The affinity of the SAM for BB3 is understand from the positive value of ΔS⁰. The negative values of ΔH∘ revealed that the adsorption is likely to be dominated by physical processes in nature involving weak forces of attraction (35,36). Also, the negative values of Δ*G*⁰ indicate the feasibility the spontaneous of adsorption process.

DISCUSSION

The sulfuric acid-activated montmorillonite mineral (SAM) was prepared by natural montmorillonite mineral (NM), and it was used for the adsorption of BB3 from an aqueous media in a thermostatic water bath. The experimental results indicated that the adsorption of the BB3 depended on the initial pH of the solution, the initial concentration of the adsorbate (BB3), the temperature, and the contact time. The experimental result is summarized as follows:

1. It was observed that the value of pH_{zpc} was 5.1 for the acid activated montmorillonite mineral,

2. It was determined the adsorption capacity of the SAM increased with contact time and reached its maximum value in the range of 85-99 mg/g for different initial pH values after approximately 60 min,

3. It was obtained that the adsorption capacity of SAM increased linearly up to pH 6, reaching a maximum value (99 mg/g) at pH 6,

4. The equilibrium adsorption capacity of the SAM was determined to be about 97 and 89 mg BB3/g at 298 and 318 K,

5. It was determined that the adsorption capacity of BB3 increased from 130 to 180 mg/g at the range of initial concentrations values between 100 to 350 mg/L,

6. The optimum adsorption conditions were determined 298 K, 6 ± 0.02, 350 ppm, and 60 min,

7. The maximum efficiency and capacity of adsorption was obtained to be about 80% and 277 mg/g at the optimum experimental conditions,

8. Lagergren's kinetic model (pseudo first order) simulated the kinetic data better than the Ho's kinetic model (pseudo second order),

9. It was obtained that The Freundlich isotherm is the best fitting isotherm model equation.

As a result of the study, the acid-activated mineral is suitable for adsorption of BB3 dye molecules from aqueous media.

REFERENCES

1. Gong R, Li M, Yang C, Sun Y, Chen J. Removal of cationic dyes from aqueous solution by adsorption on peanut hull. J Hazard Mater. 20 Mayıs 2005;121(1–3):247–50.

2. Chhabra M, Mishra S, Sreekrishnan TR. Combination of chemical and enzymatic treatment for efficient decolorization/degradation of textile effluent: High operational stability of the continuous process. Biochem Eng J. 2015;Complete(93):17–24.

3. Dulman V, Cucu-Man SM. Sorption of some textile dyes by beech wood sawdust. J Hazard Mater. Mart 2009;162(2–3):1457–64.

4. Annadurai G, Ling LY, Lee JF. Adsorption of reactive dye from an aqueous solution by chitosan: isotherm, kinetic and thermodynamic analysis. J Hazard Mater. Mart 2008;152(1):337–46.

5. Mahmoodi NM, Salehi R, Arami M, Bahrami H. Dye Removal from Colored Textile Wastewater Using Chitosan in Binary Systems. Desalination. 01 Şubat 2011;267:64–72.

6. Çakmak M, Taşar Ş, Selen V, Özer D, Özer A. Removal of astrazon golden yellow 7GL from colored wastewater using chemically modified clay. J Cent South Univ. 01 Nisan 2017;24(4):743–53.

7. Selen V, Güler Ö, Özer D, Evin E. Synthesized multi-walled carbon nanotubes as a potential adsorbent for the removal of methylene blue dye: kinetics, isotherms, and thermodynamics. Desalination Water Treat. 20 Nisan 2016;57(19):8826–38.

8. Angin D. Utilization of activated carbon produced from fruit juice industry solid waste for the adsorption of Yellow 18 from aqueous solutions. Bioresour Technol. Eylül 2014;168:259–66.

9. Zou W, Li K, Bai H, Shi X, Han R. Enhanced Cationic Dyes Removal from Aqueous Solution by Oxalic Acid Modified Rice Husk. J Chem Eng Data. 12 Mayıs 2011;56(5):1882–91.

10. Song J, Zou W, Bian Y, Su F, Han R. Adsorption characteristics of methylene blue by peanut husk in batch and column modes. Desalination. 15 Ocak 2011;265(1):119–25.

11. Kim T-H, Park C, Kim S. Water recycling from desalination and purification process of reactive dye manufacturing industry by combined membrane filtration. J Clean Prod. 01 Haziran 2005;13(8):779–86.

12. Türgay O, Ersöz G, Atalay S, Forss J, Welander U. The treatment of azo dyes found in textile industry wastewater by anaerobic biological method and chemical oxidation. Sep Purif Technol. 19 Mayıs 2011;79(1):26–33.

13.   Nanofiltration and reverse osmosis thin film composite membrane module for the removal of dye and salts from the simulated mixtures [Internet]. [kaynak 24 Eylül 2017]. Available at: https://www.researchgate.net/publication/244144789_Nanofiltration_and_reverse_osmosis_thin_film_composite_membrane_module_for_the_removal_of_dye_and_salts_from_the_simulated_mixtures

14. Coagulation/flocculation process for dye removal using water treatment residuals: modelling through artificial neural networks: Desalination and Water Treatment: Vol 57, No 55 [Internet]. [kaynak 24 Eylül 2017]. Available at: http://www.tandfonline.com/doi/abs/10.1080/19443994.2016.1165150?src=recsys&journalCode=tdwt20

15. Bohli T, Ouederni A, Fiol N, Villaescusa I. Uptake of Cd2+ and Ni2+ Metal Ions from Aqueous solutions By Activated Carbons Derived from Waste Olive Stones. C. 3. 2012. 232 s.

16. Rozada F, Otero M, Morán A, García AI. Adsorption of heavy metals onto sewage sludge-derived materials. Bioresour Technol. Eylül 2008;99(14):6332–8.

17. Ma Y, Gao N, Chu W, Li C. Removal of phenol by powdered activated carbon adsorption. Front Environ Sci Eng. 01 Nisan 2013;7(2):158–65.

18. Banerjee S, Chattopadhyaya M. Adsorption characteristics for the removal of a toxic dye, tartrazine from aqueous solutions by a low cost agricultural by-product. C. 170. 2013.

19. Baseline Studies of Source Clays [Internet]. [kaynak 24 Eylül 2017]. Available at: http://www.clays.org/sourceclays_baseline_studies.html

20. Vijayakumar G, TAMILARASAN R, Dharmendirakumar M. Adsorption, Kinetic, Equilibrium and Thermodynamic studies on the removal of basic dye Rhodamine-B from aqueous solution by the use of natural adsorbent perlite. J Mater Environ Sci. 01 Ocak 2012;3.

21. Liu H, Yuan P, Qin Z, Liu D, Tan D, Zhu J, vd. Thermal degradation of organic matter in the interlayer clay–organic complex: A TG-FTIR study on a montmorillonite/12-aminolauric acid system. C. 80–81. 2013. 398 s.

22. Öztürk N, Tabak A, Akgöl S, Denizli A. Newly synthesized bentonite–histidine (Bent–His) micro-composite affinity sorbents for IgG adsorption. Colloids Surf Physicochem Eng Asp. 05 Temmuz 2007;301(1):490–7.

23. Lee J-W, Choi S-P, Thiruvenkatachari R, Shim W-G, Moon H. Evaluation of the performance of adsorption and coagulation processes for the maximum removal of reactive dyes. Dyes Pigments. 01 Ocak 2006;69(3):196–203.

24. Yao Y, Bing H, Feifei X, Xiaofeng C. Equilibrium and kinetic studies of methyl orange adsorption on multiwalled carbon nanotubes. Chem Eng J. 15 Mayıs 2011;170(1):82–9.

25. Wang P, Cao M, Wang C, Ao Y, Hou J, Qian J. Kinetics and thermodynamics of adsorption of methylene blue by a magnetic graphene-carbon nanotube composite. Appl Surf Sci. 01 Ocak 2014;290:116–24.

26. Özer A, Akkaya G, Turabik M. Biosorption of Acid Blue 290 (AB 290) and Acid Blue 324 (AB 324) Dyes on Spirogyra rhizopus. J Hazard Mater. 01 Ağustos 2006;135:355–64.

27. Vijayaraghavan K, Yun Y-S. Bacterial biosorbents and biosorption. Biotechnol Adv. Haziran 2008;26(3):266–91.

28. S L. ABOUT THE THEORY OF SO-CALLED ADSORPTION OF SOLUBLE SUBSTANCES. 01 Ocak 1898;24(4):1–39.

29. Ho YS, McKay G. Pseudo-second order model for sorption processes. Process Biochem. 01 Temmuz 1999;34(5):451–65.

30. Ozer D, Dursun G, Ozer A. Methylene blue adsorption from aqueous solution by dehydrated peanut hull. J Hazard Mater. Haziran 2007;144(1–2):171–9.

31. Vimonses V, Lei S, Jin B, Chow CWK, Saint C. Kinetic study and equilibrium isotherm analysis of Congo Red adsorption by clay materials. Chem Eng J. 15 Mayıs 2009;148(2):354–64.

32. Toor M, Jin B. Adsorption characteristics, isotherm, kinetics, and diffusion of modified natural bentonite for removing diazo dye. Chem Eng J. 01 Nisan 2012;187(Supplement C):79–88.

33. Langmuir I. THE CONSTITUTION AND FUNDAMENTAL PROPERTIES OF SOLIDS AND LIQUIDS. II. LIQUIDS.1. J Am Chem Soc. 01 Eylül 1917;39(9):1848–906.

34. Freundlich H. Über die Adsorption in Lösungen. Leipzig: Wilhelm Engelmann; 1906. 98 s.

35. Yu Y, Zhuang Y-Y, Wang Z-H. Adsorption of Water-Soluble Dye onto Functionalized Resin. J Colloid Interface Sci. 15 Ekim 2001;242(2):288–93.

36. Chatterjee S, Chatterjee S, Chatterjee BP, Guha AK. Adsorptive removal of congo red, a carcinogenic textile dye by chitosan hydrobeads: Binding mechanism, equilibrium and kinetics. Colloids Surf Physicochem Eng Asp. 15 Mayıs 2007;299(1):146–52.

Effect of GLYMO/TEOS/MTEOS Sol-Gel Film Thickness on the Responses of Glucose Biosensor

This article was produced from a poster or oral contribution to the ICAIE Congress, 2017.

Nizamettin Demirkıran[1]*, Ergun Ekinci[2]

[1] İnönü University, Department of Chemical Engineering, Malatya/Turkey.
[2] İnönü University, Department of Chemistry, Malatya/Turkey.

Abstract: In the present study, the effect of the film thickness on the responses of a glucose biosensor was investigated. The modified platinum electrodes used in the study were constructed by immobilization of glucose oxidase under a film layer of the sol-gel coating solution. The sol-gel coating solutions were prepared by using (3-Glycidoxylpropyl) trimethoxysilane (GLYMO), tetraethoxysilane (TEOS), and methyltriethoxysilane (MTEOS). Electrochemical measurements were carried out amperometrically by determining hydrogen peroxide released by the enzymatic reaction between glucose and glucose oxidase. It was found that the amperometric responses of the sensor decreased with increasing the volume of coating solution dropped on the adsorbed enzyme. It was determined that the film thickness has a significantly influence on the sensor responses. It was observed that the amperometric responses decreased by 85% when the volume of the coating solution dropped on the electrode increased from 4 µL to 12 µL.

Keywords: Biosensor; glucose; glucose oxidase; sol-gel.

***Corresponding author. E-mail:** nizamettin.demirkiran@inonu.edu.tr.

INTRODUCTION

The routine analysis of glucose in various physiological fluids is one of the most frequent operations in a clinical chemical laboratory. The convenient, rapid, safe and precise determination of blood sugar in diabetes patients is important for the treatment and control of diabetes. Glucose can be detected by various methods, such as electrochemical, colorimetric, and optical methods. Among these methods, enzyme-based electrochemical biosensors are widely used for the determination of glucose. They may be divided into conductometric, potentiometric, and amperometric biosensors depending upon the electrochemical property to be measured by detector system. The amperometric biosensors are more attractive than the others due to their high sensitivity and wide linear range. Enzymatic detection of glucose by an amperometric biosensor is based on the monitoring of hydrogen peroxide formed by the enzymatic reaction between glucose and glucose oxidase. The resulting current changes due to the oxidation of hydrogen peroxide on the modified working electrode were measured as a function of time (1-4).

The most important subject in the development of an enzyme-based amperometric glucose biosensor is the immobilization of glucose oxidase on the surface of the working electrode. A number of immobilization techniques, such as physical entrapment, chemical immobilization in an inert matrix, and covalent attachment to electrode surfaces have been used to attach the relevant enzyme in the construction of the amperometric biosensors. Among the various modification procedures, the sol-gel technology has attracted wide spread interest to immobilize the biomoleculos in the design of the biosensor due to its distinct advantages, such as low temperature requirement, chemical inertness, negligible swelling, optical transparency, low-temperature encapsulation, tunable porosity, thermal stability, and biocompability (5-7).

The sol-gel process is a chemical synthesis method used in the preparation of glass and ceramics, thin films and coatings, fine powders, fibers and some others. This method is based on the hydrolysis and condensation reactions of liquid precursors to produce a stable gel. The sol-gel method can be also practiced to prepare the hybrid coating by using organic-inorganic silane compounds. Organic-inorganic composite materials prepared by this method have many application fields, like surface coating, corrosion protection and electrode modification. These coatings have been successfully performed as enzyme immobilization matrix due to their biocompatibility (5, 8). Several papers on the immobilization of glucose oxidase within the sol-gel matrix for the preparation of glucose biosensors have been found in the literature. In these studies, different silane compounds have been practiced as the immobilization matrix to improve the stability, selectivity, reproducibility and other analytical parameters of the biosensor (9-11).

In this study, the effect of the film thickness on the responses of the glucose biosensor prepared by immobilization of glucose oxidase on the platinum electrode surface using the sol-gel films has been reported. The sol-gel film was prepared by mixing of (3-glycidoxylpropyl)trimethoxysilane, tetraethoxysilane and methyltriethoxysilane precursors.

MATERIAL AND METHODS

The sol-gel coating solution was prepared by mixing 1 mL of (3-Glycidoxylpropyl)trimethoxysilane (GLYMO, 98%, Aldrich), 0.4 mL of tetraethoxysilane (TEOS, 98%, Aldrich), 0.4 mL of methyltriethoxysilane (MTEOS, 99%, Aldrich), and the calculated amount of distilled water in a glass vial. A calculated aliquot of concentrated HCl (37%, Riedel-de-Haën) solution was added to the mixture to accelerate hydrolysis of the silanes. The mixture in glass vial was stirred until a clear and homogeneous solution was obtained and stored at room temperature for 24 h. This solution was used as the stock sol solution. Then, a coating solution was prepared by mixing 1 mL of the stock sol solution and 3 mL of 2-butoxyethanol (Aldrich) in a separate glass vial. This final solution was stirred for 2-3 h and stored at room temperature for 24 h. The solution diluted with alcohol was used for the immobilization of glucose oxidase.

The enzyme solution was prepared by dissolving 5.1 mg of glucose oxidase (Aspergillus Niger, Sigma) in 50 µL of 0.1 M phosphate buffer solution (pH=7) at room temperature.

Phosphate buffer solution (PBS) was prepared by using disodium hydrogen phosphate and potassium dihydrogen phosphate. The glucose (α-D-(+) glucose, Sigma) stock solution (0.2 M) was prepared in distilled water and left at room temperature for 24 h prior to use to ensure the presence of β-D-glucose form.

The platinum electrode was chosen as working electrode for the preparation of the sol-gel modified glucose biosensor. A volume of 2 µL of the enzyme solution was dropped on the cleaned platinum electrode surface (2 mm diameter) and allowed to dry at room temperature. After that, the coating solutions at different volumes to obtain the varied film thickness were carefully dropped on the enzyme adsorbed onto the surface of the platinum electrode and allowed to dry at room temperature.

Electroanalytical measurements were carried out with a BAS 100 W (Bionalytical Systems, Inc.) electrochemical analyzer. All experiments were performed by using a conventional electrochemical cell with a three-electrode system, comprising a modified platinum electrode as the working electrode, an Ag/AgCl electrode saturated with KCl as the reference electrode, and a Pt wire coil as the auxiliary electrode.

Phosphate buffer solutions (PBS) used in the amperometric studies were aerated by bubbling air for about 20 min prior to use. Then, three-electrode system was immersed into 10 mL of PBS solution. The solution was stirred by using a magnetic bar to provide the convective mass transport during the experiments. A predetermined constant working potential versus Ag/AgCl was applied to the cell, and the background current was allowed to reach the steady state before glucose injections. The resulting amperometric response due to the oxidation of hydrogen peroxide formed by the enzymatic reaction was measured as a function of time, and the graphs of the current versus time were continuously recorded.

RESULTS AND DISCUSSIONS

The responses of a biosensor are affected from various parameters, such as film thickness, amount of enzyme, compound of coating solution, pH of solution, applied potential, and presence of interfering species. The film thickness is probably the most important one among these parameters because the species to be measured reaches the electrode surface by diffusing through the film. Therefore, the amount of substance diffused through the film varies depending upon whether the film is thick or thin. At the same time, the film porosity affects the response of sensor.

In a biosensor, enzyme is generally contact with electrochemical transducer, which converts an observed change into a measurable signal. A coating layer is located onto the enzyme layer, which is the recognition element of biosensor, to immobilize the enzyme. The substrate is diffused from the sample solution to the recognition element passing through the coating layer, and where an enzymatic reaction occurs between the substrate and enzyme. The product formed as a result of the enzymatic reaction is transformed by transducer the evaluable signal associated with the amount of the product. Thus, the analyte concentration in the sample solution is indirectly detected by biosensor. Consequently, it can be said that the determination of a substrate concentration by a biosensor is based mainly on a sequential two-step process including diffusion and chemical reactions. In here, the diffusion step is directly related with the thickness of the coating layer or film on the enzyme.

The overall reaction between glucose and glucose oxidase in a glucose biosensor can be written as follows:

$$Glucose + O_2 \xrightarrow{glucose\ oxidase} Gluconic\ acid + H_2O_2 \quad (1)$$
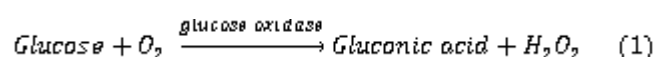
Because the glucose does not directly measure electrochemically, the amount of glucose in the sample solution can be indirectly determined by monitoring of the consumed oxygen, the produced gluconic acid or the released hydrogen peroxide. In the amperometric determination of glucose, the monitoring of hydrogen peroxide has the advantage of being simpler, especially

when miniaturized devices are concerned. Hydrogen peroxide measurements are commonly carried out on a platinum electrode at an oxidation potential of around 0.6-0.7 V versus Ag/AgCl reference electrode, and the alterations in the anodic current are recorded (in Eq. 2).

$$H_2O_2 \xrightarrow{Pt} O_2 + 2H^+ + 2e^- \qquad\qquad (2) H_2O_2 \xrightarrow{Pt} O_2 + 2H^+ + 2e^- \qquad\qquad (2)$$
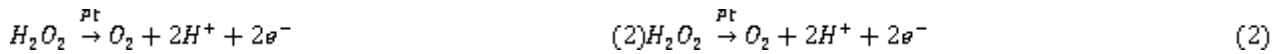
It is related to the glucose concentration whichever the chemical species mentioned above is measured. Thereby, the glucose concentration determined is proportional with the glucose amount that can pass through the coating layer. Accordingly, the film or coating layer thickness has a very important effect on the response of biosensor.

In this work, the enzyme electrodes have been prepared by dropping the sol-gel coating solution at volumes of 4, 5, 6, 7, 8, 9, 10, 11, and 12 µL on the enzyme layer adsorbed onto the platinum electrode. The results of the electrochemical tests performed using these electrodes are given in Fig. 1. In this figure, only the experimental results of the electrodes prepared by dropping aliquots of 4, 5, 6, 7, 8, and 9 µL of the sol-gel solution have been illustrated. Each injection indicated in Fig. 1 corresponds to 2 mM concentration of the glucose. For all the enzymatic electrodes obtained by dropping in the range of 4-12 µL of the sol-gel solution, the amperometric current responses for a total concentration of 10 mM glucose at the end of five injections have been shown in Table 1. A graph of the values of the amperometric responses versus each volume of the coating solution given in Table 1 are plotted in Fig. 2. As can be seen from Figs. 1-2, and Table 1, the amperometric responses of the enzymatic electrodes were decreased with increasing the amount of the sol-gel coating solution dropped on the electrodes. It was determined that the amperometric response decreased by 85% when the volume of the coating solution dropped on the electrode increased from 4 µL to 12 µL. As can be seen from Fig. 1, the responses of the enzymatic electrodes are high up to 7 µL of the sol-gel coating solution, however they are irregular responses. The similar responses to each other have been observed for 5, 6, and 7 µL of the films. The responses taken from the enzymatic electrode prepared with 8 µL of the coating solution are more uniform, and the similar results have been obtained for the successive measurements performed using this electrode. The recorded responses from the electrodes prepared beginning from 9 µL of the coating solution have been increasingly diminished. The amount of glucose passed through the pores of the resulting sol-gel film is high when the thin film is in question. As a consequence, the biosensor responses become large due to the high amount of hydrogen peroxide formed after enzymatic reaction. As the film becomes thicker, the amperometric responses of sensor decrease significantly because of a decrease in glucose diffusion through the thick sol-gel film. The thinner films may appear advantageous in terms of the sensor responses. But, the selectivity of an amperometric glucose biosensor can affect adversely from the application of

thin films because some electroactive species (e.g., ascorbic acid, uric acid, and oxalic acid) together with glucose in the real biological samples is present.
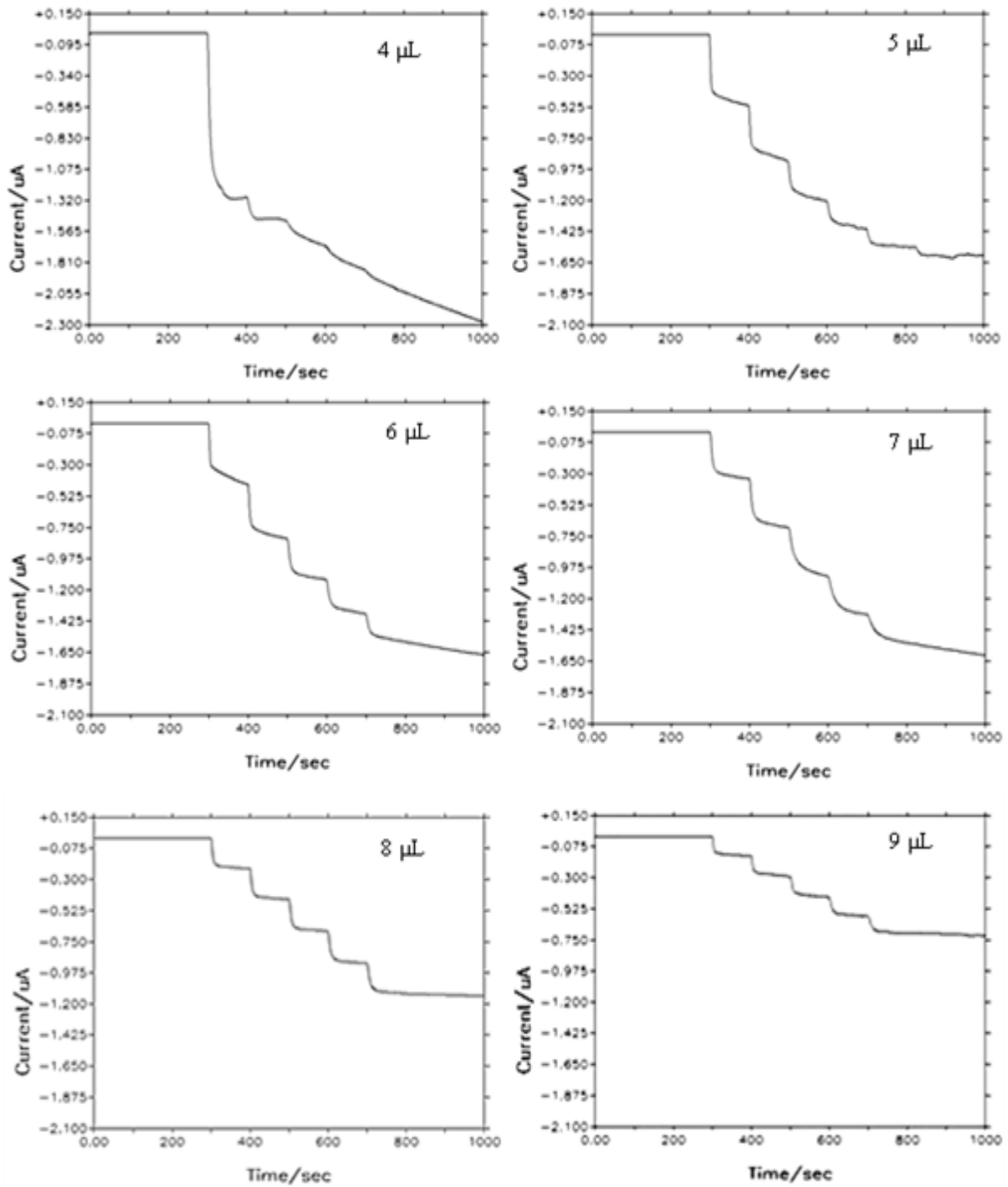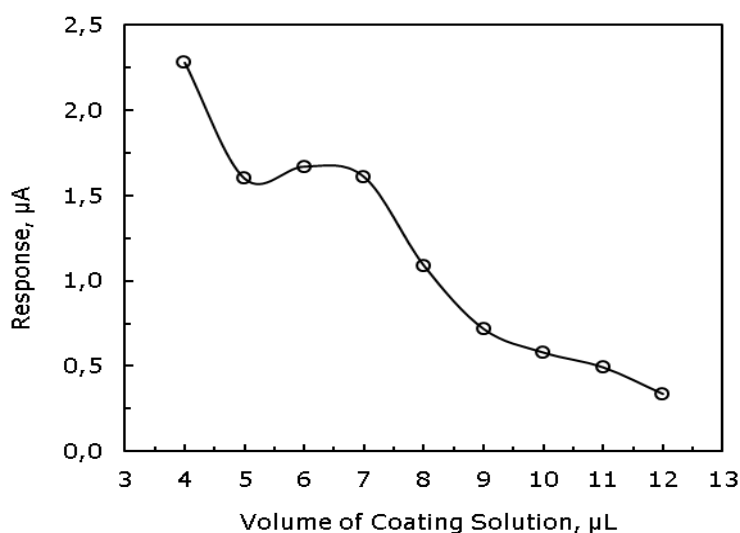

Figure 1: The amperometric responses of enzyme electrodes prepared by dropping the coating solution at different volumes.

Table 1: The values of amperometric current responses of enzyme electrodes for a total concentration of 10 mM glucose.

Volume of Coating Solution, µL	Response, µA
4	2,28
5	1,60
6	1,62
7	1,61
8	1,09
9	0,72
10	0,58
11	0,49
12	0,34

Figure 2: The graph of amperometric current responses of enzyme electrodes for a total concentration of 10 mM glucose at various volumes of coating solution.

These species can oxidize on the electrode surface by passing through the sol-gel film and can interfere to the current responses of the released hydrogen peroxide by enzymatic reaction. In addition to this, the leaching of enzyme through the pores of the thin sol-gel films can take place from the electrode surface into the sample solution. These negativities may overcome by using the thicker sol-gel films. But in this case, the mass transfer from the sample solution to the enzyme under the film layer becomes difficult and the sensor responses decrease. When the thicker sol-gel films are used, the diffusion pathway can lengthen and the pores of the film can block. Hence, the whole glucose injected may not pass from the thick sol-gel film, and ultimately the amperometric responses of glucose sensor decrease significantly.

CONCLUSIONS

In this study, the effect of the amount of the sol-gel coating solution on the responses of the glucose biosensor has been examined. The enzymatic electrodes were produced by entrapping under a silica sol-gel film of the glucose oxidase adsorbed on the platinum electrode surface. The silica sol-gel coating solutions have been prepared by using GLYMO, TEOS, and MTEOS. It was observed that the amperometric responses decreased with increasing the volume of coating solution dropped on the adsorbed enzyme. A decrease in the amperometric responses can be attributed that the diffusion of glucose through the resulting thick sol-gel films becomes difficult. According to the experimental findings determined, it can be said that the film thickness or the amount of the coating solution dropped on the electrode has a significantly influence on the sensor responses. The experimental findings showed that the current responses were decreased by 85% when the volume of the coating solution dropped on the electrode increased from 4 µL to 12 µL.

REFERENCES

1. Li J, Chia L.S., Goh N.K., Tan S.N., Ge H. Mediated amperometric glucose sensor modified by the sol-gel method, Sens Actuators B,1997;40:135-141. DOI:10.1016/S0925-4005(97)80252-3

2. Chaubey A, Malhotra B.D. Mediated biosensors, Biosens Bioelectron, 2002; 17:441-456. DOI:10.1016/S0956-5663(01)00313-X

3. Freire R.S., Pessoa C.A., Mello L.D., Kubota L.T. Direct electron transfer:An approach for electrochemical biosensors with higher selectivity and sensitivity, J Braz Chem Soc, 2003; 14:230-243. http://jbcs.sbq.org.br/imageBank/PDF/v14n2a08.pdf

4. Wang J. Electrochemical glucose biosensors, Chem Rev, 2008;108:814-825. DOI:10.1021/cr068123a

5. Collinson M.M. Analytical applications of organically modified silicates, Mikrochim Acta, 1998; 129:149-165. DOI:10.1007/BF01244737

6. Jin W, Brennan J.D., Properties and application of proteins encapsulated within sol-gel derived materials, Anal Chim Acta, 2002;461:1-36. DOI:10.1016/S0003-2670(02)00229-5

7. Thenmozhi K, Narayanan S.S. Electrochemical sensor for H2O2 based on thionin immobilized 3-aminopropyltrimethoxy silane derived sol-gel thin film electrode, Sens Actuators B, 2007; 125:195-201. DOI:10.1016/j.snb.2007.02.006

8. Tu Y.F., Di J.W., Chen X.J. Study of the nano-size silica sol-gel film as the matrix of chemically modified electrode, J Sol-Gel Sci Technol, 2005;33:187-191. DOI:10.1007/s10971-005-5613-6

9. Pandey P.C., Upadhyay S, Pathak, H.C. A new glucose sensor based on encapsulated glucose oxidase within organically modified sol-gel glass, Sens Actuators B, 1999;60:83-89. DOI:10.1016/S0925-4005(99)00246-4

10. Pauliukaite R, Brett C.M.A. Characterization of novel glucose oxysilane sol-gel electrochemical biosensors with copper hexacynoferrate mediator, Electrochim Acta, 2005;50:4973-4980. DOI:10.1016/j.electacta.2005.01.060

11. Demirkıran N, Ekinci E. Immobilization of glucose oxidase in GLYMO/MTEOS sol-gel film for glucose biosensor application, Acta Chim Slov, 2012; 59:302-306. http://acta-arhiv.chem-soc.si/59/59-2-302.pdf

RESEARCH ARTICLE

Thermal and Mechanical Properties of Cement-Eps-Marble Powder Composites

This article was produced from a poster or oral contribution to the ICAIE Congress, 2017.

Ayse BICER[1]*, Filiz KAR[1]

[1]Department of Chemical Engineering, Firat University, Elazig/Turkey

Abstract: This work was undertaken to produce a new construction materials which could have insulation and mechanical strength properties by using two different wasted materials. The waste expanded polystyrene (EPS) and marble powder were used as the aggregate in order to produce a new concrete material. After waste EPS is collected as packaging material, it is mixed with the cement of percentages; 20%, 40%, 60% and 80%. Marble powder is added to each of this cement at 0.0%, 0.5%, 1% and 1.5% of the weight of the mixture. 16 different samples were produced. At the end of 28 days of drying period, the samples were subjected to a number of tests so that their physical characteristics could be identified. As a result of these test, it was concluded that EPS ratio of the samples increased, their density, thermal conductivity, the compression and tensile strength decreased, while porosity increased. It was recommended that; using EPS aggregated and marble powder added concrete, *(i)* the waste EPS and marble powder can be evaluated as construction material, *(ii)* building heating and cooling energy will be saved.

Cite this: Biçer A, Kar F. Thermal and Mechanical Properties of Cement-Eps-Marble Powder Composites. JOTCSB. 2017;1(Special issue 1):25–32.

*Corresponding author. E-mail: abicer@firat.edu.tr

INTRODUCTION

Today styropor can be used as insulation material in buildings; it is also widely used in packaging industry. As an important waste material in terms of environmental pollution, this material has to be recycled and re-economized. Revaluation of waste EPS as construction material is important both in terms of its contribution to economy and as a solution to environmental solution problem. Several studies have been made on the usage of EPS as construction material. A considerable portion of these studies are related to the use of aggregate in concrete. Some of these studies are summarized below.

Babu *et al*. examined the mechanical features of light concretes produced by using ly ash along with expanded polystyrene along with regular aggregate [1]. Miled et al. studied the impact of the change in the amount and dimensions of EPS found on aggregated concrete samples on the pressure resistance of the concrete [2]. Bourvard et al. worked on the physical features of high-performance concretes consisting of expanded polystyrene balls [3]. Chen studied on the characteristics of the light concrete which consists of polystyrene foam reinforced with steel fibre [4]. Babu et al. investigated the mechanical behaviours of the concretes which were mixed with silica fume at different rates in order to increase the resistance of low-intensity concrete consisting of EPS [5]. Demirboga and Kan displayed the changes in thermal conductivity, density and average drying contraction values of the concrete in the samples they produced by using 25, 30 and 100% EPS as aggregate in concrete [6],. Rossignolo and Agnesini studied the technical properties of concretes created with light aggregate mixtures of styrene-butadiene rubber (SBR) modified with two types of light aggregates [7],. Kaya and Kar investigated the physical characteristics of light concrete and gypsum coatings with waste EPS aggregates [8]. Kaya and Kar tested thermal and mechanical properties of the light weight concretes with EPS and tragacanth resin [9]. Sariisik and Sariisik determined the thermal conductivity value of concrete mixtures with cement, pumice and EPS [10]. Khedari et al. investigated a new lightweight construction material, composed of cement, sand and fiber of waste coconut [11].

In this paper, the mechanical features of samples produced by granulating the EPS particles which are liberated as waste material in packaging industry using certain amounts of cement and marble powder have been examined.

EXPERIMENTAL

Materials

Expanded Polystyrene Foam (EPS) is a foam-like- closed-pored thermoplastic material, typically in white colour, obtained from polymerization of styrene monomer (Figure 1). EPS products were acquired by bulking and amalgamation of polystyrene particles. "Pentane" gas

was used for particle bulking and foam acquiring. Pentane is an organic component and after it ensures formation of many small particles within particles, it is exchanged by air in a very short time during and after the production. With the liberation of pentane, inert air is trapped in the abounding (3-6 billion in 1 m^3 EPS depending on density) number of small pored cells. 98 percent of the material is air and the rest is polystyrene (8). EPS is a close-pored material. Due to its very low level of water absorption, its features do not change even if it directly contacts with water. As it does not dissolve and disintegrate in water, the pore walls are water-proof.
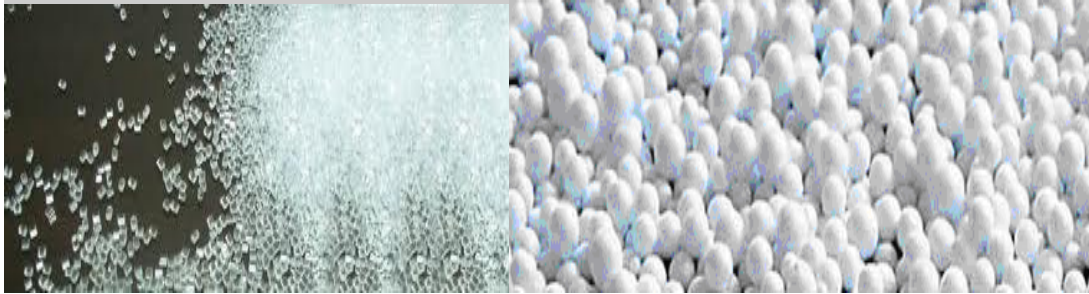
Figure 1: Polystyrene and expanded polystyrene (7).

Marble Powder (MP) are obtained from Marble manufacturing facility in Elazig.

CEM IV/B(P)32.5 R   pozzolanic cement were used to EPS and marble powder as a binder. Chemical components of cement are given in Table 1.

Table 1: Chemical composition of cement used.

Component	SiO$_2$	CaO	Al$_2$O$_3$	Fe$_2$O$_3$	MgO	SO$_3$	Cl	Fire loss	Not available
(%)	23.51	58.51	6.15	4.00	2.27	2.37	0.10	2.04	0.72

The prepared blends were mixed with sufficient amount of water and poured into the pre-assembled molds. The weights after mixing the cement, EPS and marble powder with the mentioned percentages are listed in Table 2. The molds that were formed had the dimensions of 100x100x100 mm for mechanical tests and the dimensions of 20x60x150 mm for thermal tests (Figure 2).

Table 2: Details of the cement-EPS-marble powder mixes.

Samples	Volumetric ratio		Weight (g)		Total weight	Marble powder	Marble powder	(W)/(C+E+M)
	EPS	cement	EPS					
Sample 1	80	20	20.4	450	470.4	0.0	-	0.5
Sample 2	60	40	15.6	900	915.6		-	
Sample 3	40	60	10.4	1350	1360.4		-	
Sample 4	20	8080	5.2	1800	1805.2		-	
Sample 5	80	20	20.4	450	470.4	0.5	23.53	0.5
Sample 6	60	40	15.6	900	915.6		45.78	
Sample 7	40	60	10.4	1350	1360.4		68.02	
Sample 8	20	80	5.2	1800	1805.2		90.26	
Sample 9	80	20	20.4	450	470.4	1	47.0	0.5
Sample	60	40	15.6	900	915.6		91.5	
Sample	40	60	10.4	1350	1360.4		136	
Sample	20	80	5.2	1800	1805.2		180.52	
Sample	80	20	20.4	450	470.4	1.5	70.5	0.5
Sample	60	40	15.6	900	915.6		137	
Sample	40	60	10.4	1350	1360.4		204	
Sample	20	80	5.2	1800	1805.2		270	

W:Water, **C:**cement, **E:**EPS, **M:**marble powder

Figure 2: Rectangular and cubic block samples.

Thermal and Mechanical Test

The thermal conductivities of specimens were detected by *Isomet 2104* unit, which makes measurements by using the hot wire method according to *DIN 51046.* Its range and sensitivity were 0.02-6.00 W/mK respectively and its precision was ±5% [9]. Each sample block was measured three times at three locations to show the average of nine values. The temperature was between 22°C and 25°C during measurement.

Compressive strength tests on the samples were undertaken according to the *ASTM C 109-80* standard. The tensile strength values calculated according to the *TS 500* standard by Eq. 1 [13].

$$f_{ctk} = 0.35\sqrt{f_{ck}}$$ (Eq. 1)

Here;

f_{ck}: Compressive strength (MPa) f_{ctk}: Tensile strength (MPa)

Elasticity module is mostly calculated by theoretical methods [12]. Elasticity module values are calculated according to the *TS 500* standard by Eq. (2) [13]:

$$E=3.25*(fck)^{1/2}+14 \qquad\qquad\qquad\qquad \text{(Eq. 2)}$$

In this equation, *E* is the elasticity module (GPa), and f_{ck} is the characteristic compressive strength (MPa).

The water absorption test aimed to analyze the maximum water uptake amount. This characteristic is significant to designate whether the material is appropriate for use against freezing risks. The critical moisture amount is 30% of the total dry volume and the material does not deform when frozen below this amount. The tests were performed by complying with BS 812, Part 2 standard and keeping the samples in water.

$$\text{Water absorption}=\{[W_d-W_k]/W_k\}.100 \qquad\qquad \text{(Eq. 3)}$$

In the equation, W_k is the dry weight of sample and W_d is the wet weight of sample.

The purpose of drying ratio test is to search the respiration abilities of the samples. After being left in water contained for 48 hours the samples were taken from the water, wiped with a wet piece of cloth and left to natural drying at 22°C room temperature. The drying ratio values are calculated by Eq. (4). Drying occurs through evaporation from the surface of the material; here it is about the movement of water from the depth of the material through capillary canals, meaning that moisture is expelled from the body through steam permeability resistance and drying occurs.

$$\text{Drying ratio}=\{[W_d-W_k]/W_d\}.100 \qquad\qquad \text{(Eq. 4)}$$

The results are shown in Table 3.

Table 3: Thermal and mechanical properties of samples

Sample no	Density (g/cm^3)	Thermal conductivity(W/mK)	Compressive strength (MPa)	Tensile strength (MPa)	Elasticity module (GPa)	Water absorption (%)	Drying ratio (%)
1	1.36	0.071	18.50	1.50	27.98	23.41	16.83
2	1.15	0.135	14.58	1.34	26.41	22.06	14.10
3	0.89	0.250	9.15	1.06	23.83	19.55	11.66
4	0.65	0.390	5.12	0.79	21.35	16.6	8.32
5	1.42	0.083	18.94	1.52	28.14	22.05	16.00
6	1.22	0.184	14.89	1.35	26.54	20.10	13.25
7	1.08	0.290	10.18	1.12	24.37	17.11	10.42
8	0.75	0.424	5.38	0.81	21.54	15.85	7.00
9	1.52	0.094	19.04	1.53	28.18	20.90	15.10
10	1.35	0.213	15.15	1.36	26.64	8.80	12.96
11	1.25	0.333	10.36	1.13	24.46	16.74	8.90
12	0.88	0.441	5.70	0.84	21.75	14.17	6.50
13	1.61	0.101	13.48	1.29	25.93	18.75	13.28
14	1.45	0.232	10.60	1.13	24.58	16.45	11.05
15	1.36	0.360	6.27	0.88	22.14	14.56	7.10
16	0.96	0.462	2.58	0.56	19.22	12.28	6.02

RESULTS AND DISCUSSIONS

When Figure 3 is examined, it can be seen that density values of the samples decrease as EPS ratio increases. This reduction is directly related to the density of EPS. But density of the samples increase marble powder ratio decreases.
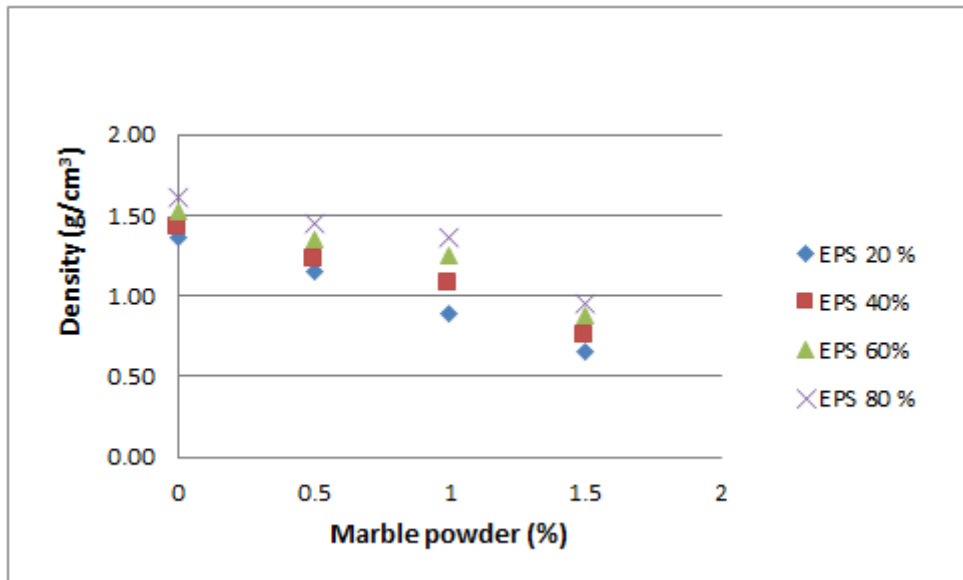
Figure 3: Density ratio of samples versus EPS percentages

Considering Figure 4, it is clear that thermal conductivity drops as EPS ratio climbs. Thermal conductivity depending on EPS ratios, 20% and 80%, decreased by 81.79 %. In the case of 0% and 1.5% ratios of marble powder in the mixture the thermal conductivity increased as 28.16-17.94%.
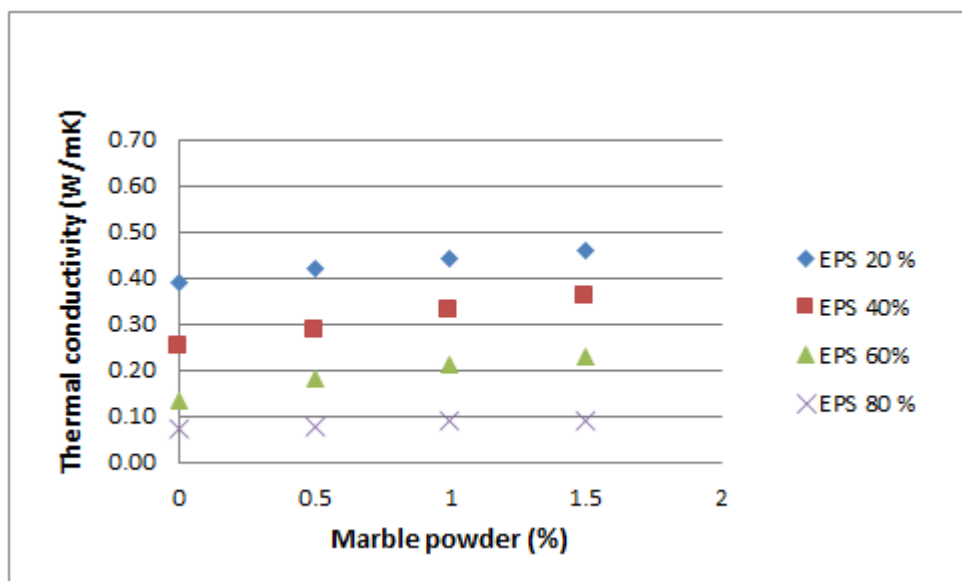
Figure 4: Thermal conductivity variation according to EPS and MP.

27

The Figures 5, 6, 7 shows that compressive strength, tensile strength and elasticity module values increases from 0 to 60% EPS and marble powder 1% ratios. But their values decreases after from the rate of the 1% marble powder. Because, cement and marble powder aggregate (1%) are creating a good mix.
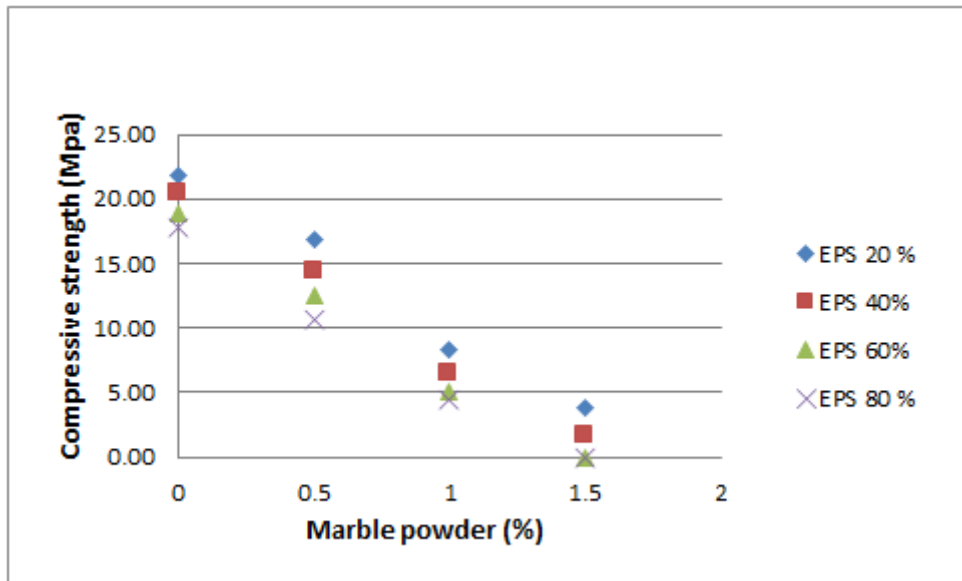
Figure 5: Compressive strength-EPS and marble powder percentage relation in the specimens.
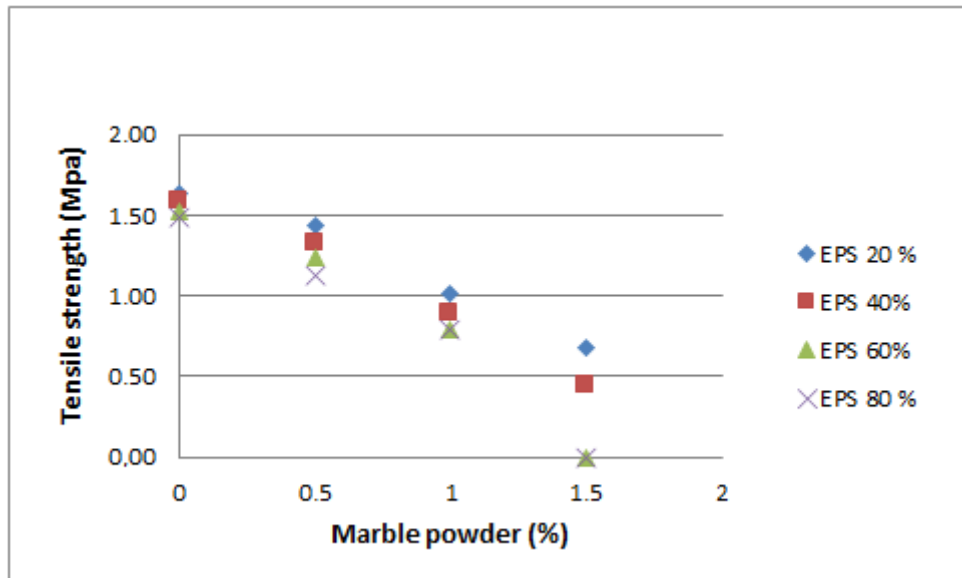
Figure 6: Tensile strength-EPS and marble powder percentage relation in the specimens.
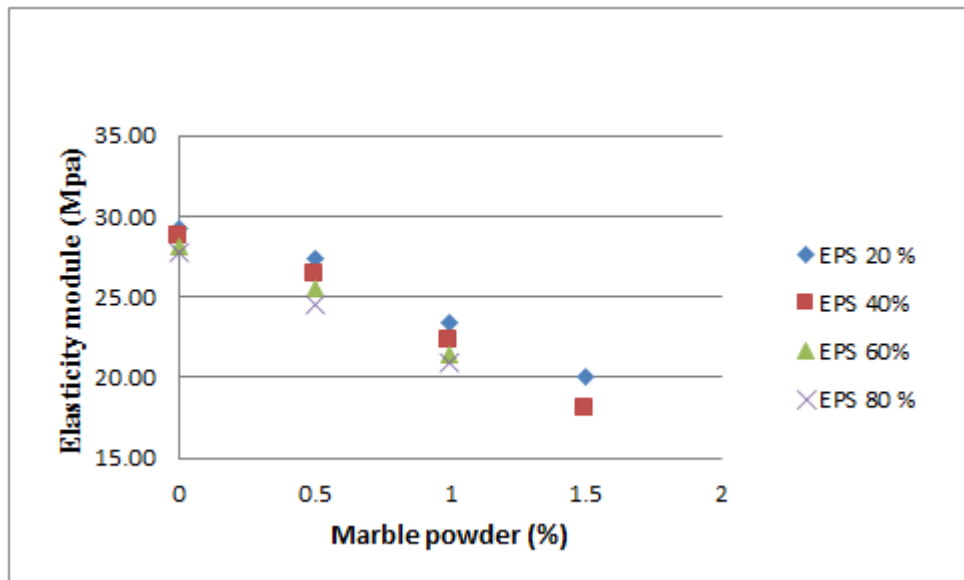
Figure 7: Variation of drying ratio of samples versus EPS percentages.

Almost all of the samples with resin added cement binders remained below 30%, which is the critical level for water absorption (Fig. 8). Therefore these materials can be used without the risk of freezing under 0°C temperature in places which is in contact with water.
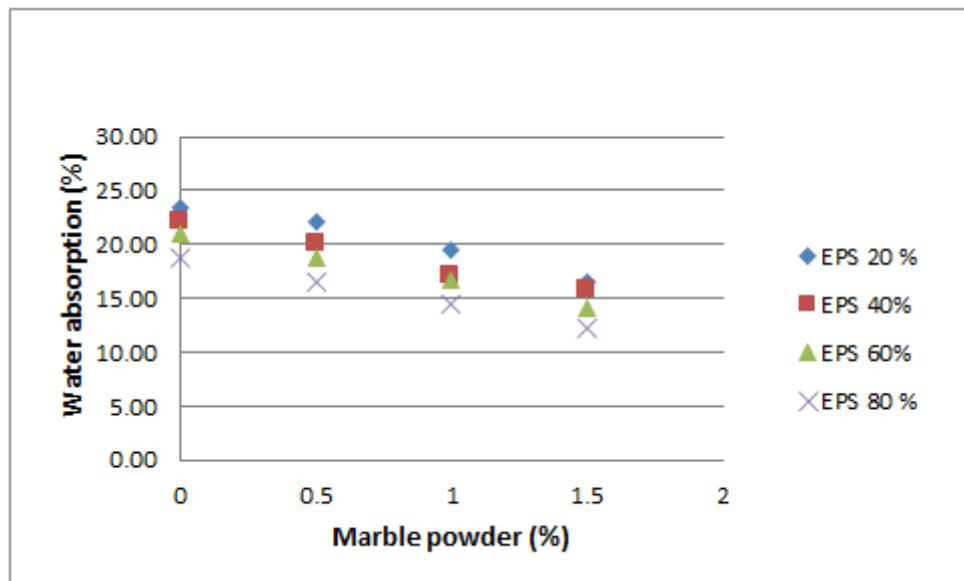
Figure 8: Variation of water absorption ratio of samples versus EPS percentages.

Considering Figure 9, it is clear that the sample drying ratios diminish as the EPS particle addition ratio grows. The moisture contained in the material moves towards the surface by means of capillary channels. This indicates the material's respiration ability.
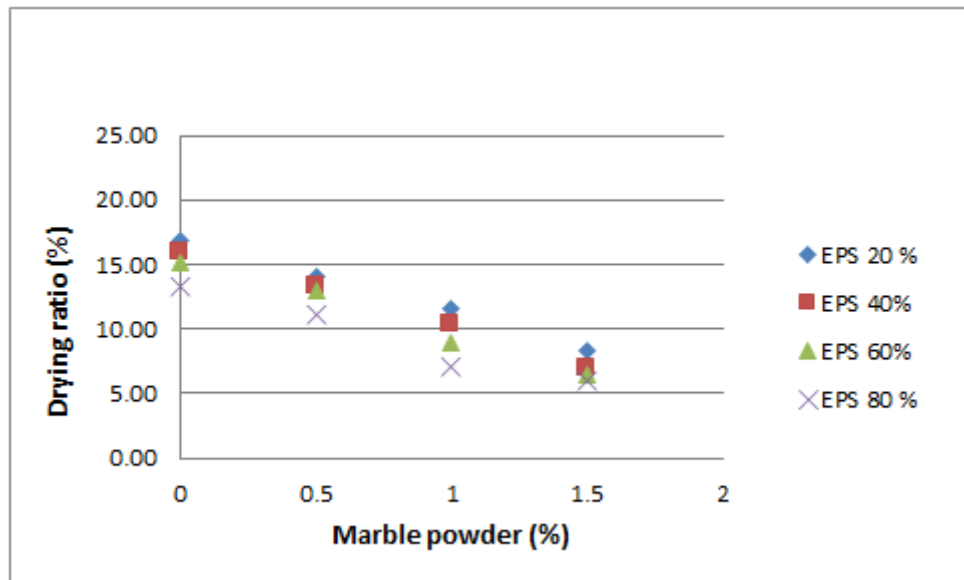
Figure 9: Variation of drying ratio of samples versus EPS percentages

CONCLUSION

This study was conducted to illustrate whether the use of waste EPS and marble powder in concrete was possible in place of natural aggregate materials.

Low-density concrete with EPS and marble powder aggregate can be used in panel walls, floorings and floor deck concretes as well as construction applications such as concrete briquettes, whereas blocks of plaster with the same additives can be used as insulation coating.

These materials should not be used as columns and beams components in buildings due to low compressive, tensile strength and elasticity module values of the samples. Nevertheless, these concretes with low density are designated as flooring, ceiling and wall concrete.
The rate of water absorption of samples is less than 30%. From this result, it is concluded that these materials can be used as concrete and external plaster or inner plaster material that subjected to water.

In conclusion, the concrete material containing EPS and marble powder can be used as building material and simultaneously solve the environmental pollution problem by recycling waste EPS and marble powder.

REFERENCES

1. Babu DS, Babu KG, Wee TH, Properties of lightweight expanded polystyrene aggregate concretes containing fly ash, Cement and Concrete Research, 2005, 35, 1218–1223.

2. Miled K, Sab K, Roy RL, Particle size effect on EPS lightweight concrete compressive strength: Experimental investigation and modeling, Mechanics of Materials, 2007, 39, 222-240.

3. Bouvard D, Chaix JM, Dendievel R, Fazekas A, Létang JM, Peix G, Quenard D, Characterization and simulation of microstructure and properties of EPS lightweight concrete, Cement and Concrete Research, 2007, 37, 1666-1673.

4. Chen B, Liu J, Properties of lightweight expanded polystyrene concrete reinforced with steel fiber, Cement and Concrete Research, 2004, 34, 1259–1263.

5. Babu, K.G. and Babu D.S., Behavior of lightweight expanded polystyrene concrete containing silica fume, Cement and Concrete Res. 2003, 33, 755-762.

6. Demirboga R, Kan AK, Thermal conductivity and shrinkage properties of modified waste polystyrene aggregate concretes, Construction and Building Materials, 2012, 35, 730–734.

7. Rossignolo YA, Agnesini MVC, Mechanical properties of polymer modified lightweight aggregate concrete, Cement and Concrete Research, 2002, 32, 329-334.

8. Kaya A, Kar F, Thermal and mechanical properties of concretes with Styropor, Journal of Applied Mathematics and Physics, 2014, 2-6, 310-315.

9. Kaya A, Kar F, Properties of concrete containing waste expanded polystyrene and natural resin. Construction and Building Materials, 2016, 105: 572-578.

10. Saiisik A, Sariisik G, New production process for insulation blocks composed of EPS and lightweight concrete containing pumice aggregate. Mater. Struct., 2002, 45(9), 1345-1357.

11. Khedari J, Suttisonk B, Pratinthong N, Hirunlabh J, New lightweight composite construction materials with low thermal conductivity. Cement and Concrete Composites, 2001, 23: 65-70.

12. Cui HZ, Lo TY, Memon SA, Xing F, Shi X. Analytical model for compressive strength, elastic modulus and peak strain of structural lightweight aggregate concrete. Construction and Building Materials, 2012, 36: 1036-1043.

13. TS 500, Turkish Standard, 2000, Ankara.

The Production of Vegetable Oil-Based Polyols and Modelling of Rheological Properties

This article was produced from a poster or oral contribution to the ICAIE Congress, 2017.

Ercan Aydoğmuş[1,*], Müge Gür[1], Fethi Kamışlı[1]

[1]Fırat University, Department of Chemical Engineering, 23119, Elazığ/Turkey

Abstract: In this study, some vegetable-oil based polyols were produced from the different vegetables oils with the catalysts. The produced polyols compared with commercial polyols in terms of rheological properties such as viscosity, temperature, shear stress, shear rate. The rheological properties of the polyols were modelling with general equations based on experimental data. Canola, cotton, linseed, corn, hazelnut and soybean oils were used in the production of polyols. The polyol production was accomplished by oxygen bonding to the structure followed by hydroxyl bonding by breaking the double bonds in the oil. These steps were, respectively, the steps of epoxidation, hydroxylation and purification. In this study, variations of viscosities of soybean oil, cottonseed oil, corn oil, hazelnut oil, canola oil, linseed oil-based polyols and commercial polyols were determined a function of temperature. It is known that the viscosity of the fluid decreases as temperature increases. The tested polyols showed Newtonian and non- Newtonian fluids behavior at certain temperature range. According to the experimental data; the linear and non-linear regression were made to determine coefficients of regression in the model equations.

Keywords: Vegetable oil; polyols; rheological properties; modelling.

INTRODUCTION

When the polyurethane produced from petroleum-based polyols is compared with that produced from vegetable oil-base polyols, a smaller amount of isocyanate is used for the production of polyurethane from vegetable oil polyols. The polyurethane produced from the vegetable oil-base polyols has a lower compression resistance [1].

Wood powder was added as filler to the polyurethane derived from castor oil-based polyol. The polyurethane of the swelling time was compared with commercial polyols, and castor oil-based polyols. Effective thermal conductivity of the castor oil-based polyurethane material was compared to that of commercial polyurethane material and it was observed that the effective thermal conductivity for the polyurethane produced from vegetable oil-base polyols had a lower value. Increasing the filler has negative impact on the effective heat transfer coefficient. Density of polyurethane material was found to be between 36 and 39 kg/m^3. TGA value of the thermal stability of the castor oil-based polyurethane material was found to be more commercially polyol product [2].

The goal of this study is to determine the rheological properties of different oil-based polyols and choose the best model complying with experimental data and the viscosity to each waste vegetable oil based-polyols are measured at different temperatures (25, 30, 35, 40, 45 and 50 °C) by using a rotary viscometer (Brookfield DV-II). Samples were sheared with several different rotational speeds at an increasing order. One of the most important parameters required in the design of technological processes in polyurethane industries is the viscosity of raw materials. Data obtained for apparent viscosity and rotational speed were used to describe the flow behavior by the model equations both in the forward and backward - measurement.

The polyols are produced from the waste vegetable oils in three consecutive steps which are epoxidation, hydroxylation and purification. The temperature of the system is kept under the control using a thermostat. When it is reached to the desired reaction temperature, the peroxides are added into the vegetable oils in acidic medium by the aid of dropping funnel in the certain time.

After the reaction is completed, the mixture is taken into separatory funnel and after for a while the mixture separates in two phases with the upper phase of the epoxidized vegetable oil. After the epoxidation step, neutralization with water and the hydroxylation starts. Especially hydroxylation with alcoholysis is frequently preferred in the production of polyols. The purification process is carried with rotary evaporator to get rid of impurities such as water, heptane and etc. The polyols produced from the vegetable oil are used in the production of polyurethane by checking the number of hydroxyl. The structures of the hydroxyl compounds

were investigated with the FTIR spectrometer. The polyurethane was produced from the different vegetable oil-based polyols and commercial polyols. The characteristic properties of the polyurethane such as thermal conductivity, the structures of porosity, density were determined. The polyurethane produced from the different vegetable oils is compared one another in terms of thermal properties.

EXPERIMENTAL

Material, Methods, and Modelling

In this study, a system consisting of a three necked balloon joe, thermometer, water bath, magnetic stirrer, condenser and funnel was used for the epoxidation reaction, which is the first step of obtaining polyols from vegetable oils used as raw materials. A three-necked balloon was used at the atmospheric pressure with a magnetic stirrer to heat the water bath to 325 – 330 K. A condenser system was attached to the ball of three necks and a thermometer is placed with the help of plugs. The refined oil was placed in the amount determined in a three-necked balloon with the aid of a funnel. Acetic acid, sulfuric acid and heptane were added to the system with the necessary optimizations. Hydrogen peroxide was added dropwise to the system after reaching a temperature of 325 K, and the epoxidation step was carried out in 4 hours. After the reaction was completed, the epoxy-oil is separated off with the separating funnel. Since the epoxy-oil was acidic, the pH value was raised by washing with pure water. Neutralization was also achieved using a basic ion exchange resin. In the experimental system, the hydroxylation was carried out by adding the certain amounts of methanol, water and acetic acid to the three necked balloon. The mixture was heated to the boiling temperature of the methanol while it was stirred. When the boiling temperature was reached, epoxy-oil was added to the three necked balloon. Hydroxylation proceeded for about 2 hours. Neutralization was performed again after this step. In the last step, impurities such as water, methanol, heptane were removed by using vacuum evaporator. The hydroxyl value of the obtained polyol was determined according to ASTM D 4274 D method.

The viscosities of the polyols produced from different the vegetable oils were measured by using a rotary viscometer (Brookfield DV-II) at different temperatures (25, 30, 35, 40, 45 and 50 °C). Samples were sheared with several different rotational speeds (2.5, 5, 10, 20, 30 and 50 rpm) at an increasing order. The obtained data for apparent viscosity and rotational speed were used to describe the flow behavior by the model equations.

Brookfield rotational viscometer (Model DV-II, Brookfield Engineering Laboratories) equipped with spindle 21 was used to measure viscosities of produced and commercial polyols. Enough samples nearly 8 mL in the beaker were used for immersing the groove on the spindle with guard leg. Temperature was kept constant at a desired value using thermostatically controlled

electrical system. Shear rate ($\dot{\gamma}$) and shear stress (τ) were read from viscometer directly. Shear stress and shear rate can also be calculated by using Eq. (1), (2) and (3).

$$\dot{\gamma} = \beta.N \qquad \textbf{(Eq. 1)}$$

$$\tau = \mu.\dot{\gamma} \qquad \textbf{(Eq. 2)}$$

$$\tau = K.(\mu)^{\delta} \qquad \textbf{(Eq. 3)}$$

Where; N is rotational speed (rpm), τ is shear stress (Pa), μ is the apparent viscosity (mPa.s), K is the consistency coefficient (mPa.s), δ is flow behavior index and β is coefficient (dimensionless).

The viscosity of a blend as a function of temperature can be calculated using one of the equations given below. Here all the equations given below are used to determine how the viscosity depends on temperature. In order to choose the best model for each blend, R^2 is calculated for each model.

$$\mu_{Linear} = a.T + b \qquad \textbf{(Eq. 4)}$$

$$\mu_{Exponential} = c.\exp(d.T) \qquad \textbf{(Eq. 5)}$$

$$\mu_{Power} = e.T^f \qquad \textbf{(Eq. 6)}$$

$$\mu_{Logarithmic} = g.\ln(T) + h \qquad \textbf{(Eq. 7)}$$

$$\mu_{Polynomial} = i.T^2 + j.T + k \qquad \textbf{(Eq. 8)}$$

$$\mu_{Suggested} = \exp(-T) + m.T + n \qquad \textbf{(Eq. 9)}$$

FIGURES AND TABLES

Table 1: Comparison of vegetable oil based polyols with model equations.

MODELS	Correlation Coefficients	Soybean Polyols	Cotton Polyols	Corn Polyols	Hazelnut Polyols	Canola Polyols	Linseed Polyols
Linear	**a**	-9,6579	-7,9912	-1,9308	-5,8209	-2,1367	-4,4974
	b	3058,5	2508,7	643,23	1793,2	707,18	1355,3
	R²	0,9702	0,9855	0,9588	0,9567	0,9296	0,9929
Exponential	**c**	2.10^6	5.10^{16}	2.10^{10}	4.10^{18}	1.10^9	5.10^{37}
	d	-0,109	-0,113	-0,065	-0,131	-0,056	-0,283
	R²	0,7668	0,7897	0,8920	0,7809	0,9653	0,9066
Power	**e**	6.10^{82}	7.10^{85}	4.10^{51}	1.10^{97}	2.10^{44}	4.10^{208}
	f	-32,56	-33,85	-20,11	-38,55	-17,19	-83,91
	R²	0,7542	0,7809	0,8773	0,7717	0,9593	0,9044
Logarithmic	**g**	-2906	-2400	-601,1	-1721	-663,2	-1335
	h	16736	13798	3492,4	9862,8	3848,3	7619,5
	R²	0,9667	0,9830	0,9600	0,9524	0,9404	0,9935
Polynomial	**i**	-0,095	-0,105	0,006	-0,144	0,039	0,132
	j	47,629	55,433	-5,377	79,46	-26,51	-82,93
	k	-5576,5	7025,3	1179,4	-10842	4465,6	12991
	R²	0,979	0.995	0.961	0.987	0.994	0.998
New (Suggested)	**m**	-9,65795	-7,97888	-1,93083	-5,82090	-2,13662	-4,49741
	n	3058,480	2505,030	643,2298	1793,152	707,1342	1355,300
	R²	0,9996	0,9997	0,9998	0,9998	0,9997	1,0000
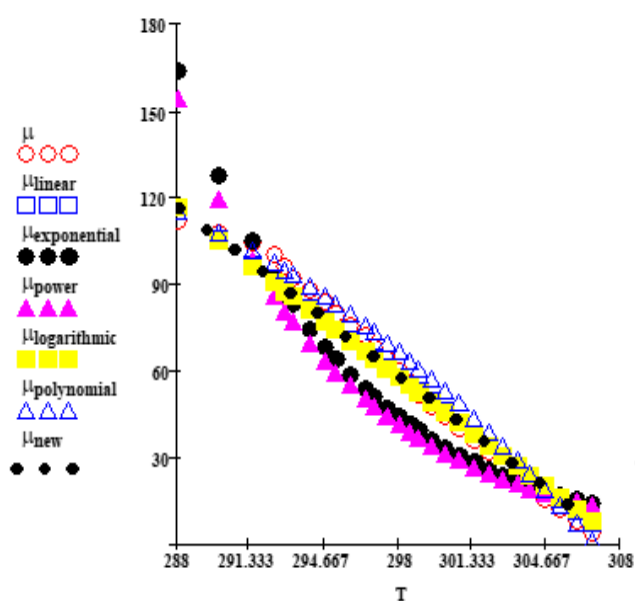
Figure 1: Hazelnut oil-based polyols
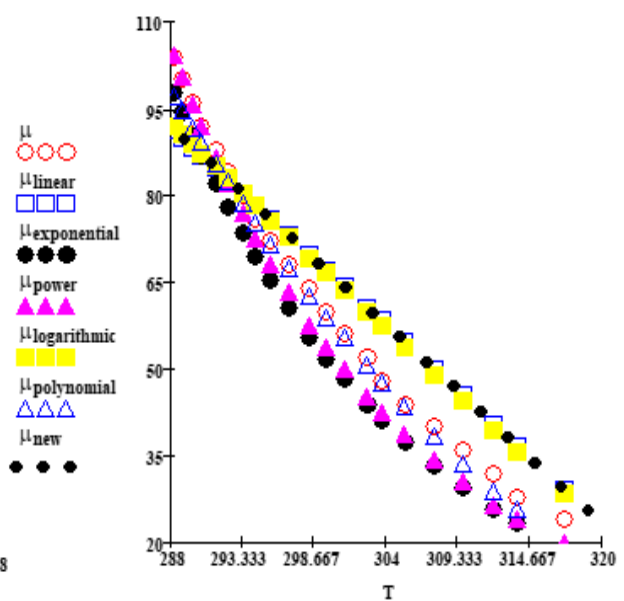
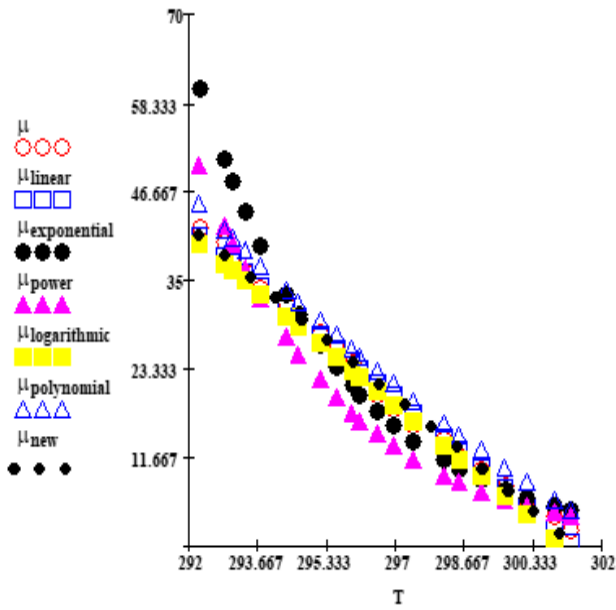
Figure 2: Canola oil-based polyols
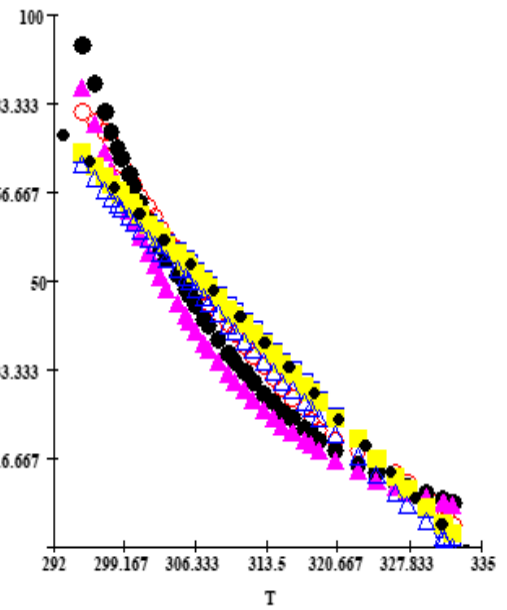
Figure 3: Linseed oil-based polyols
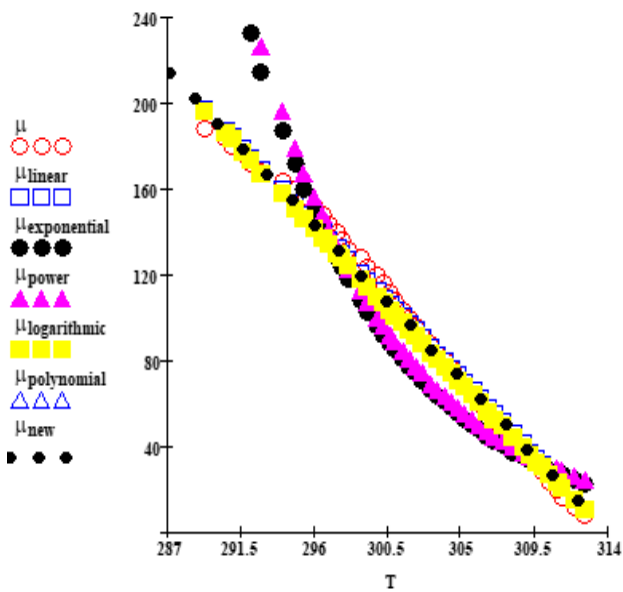

Figure 4: Corn oil-based polyols

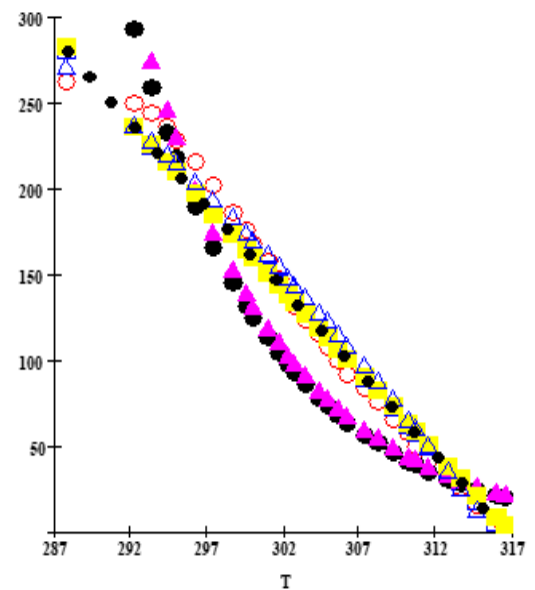**Figure 5:** Cottonseed oil-based polyols

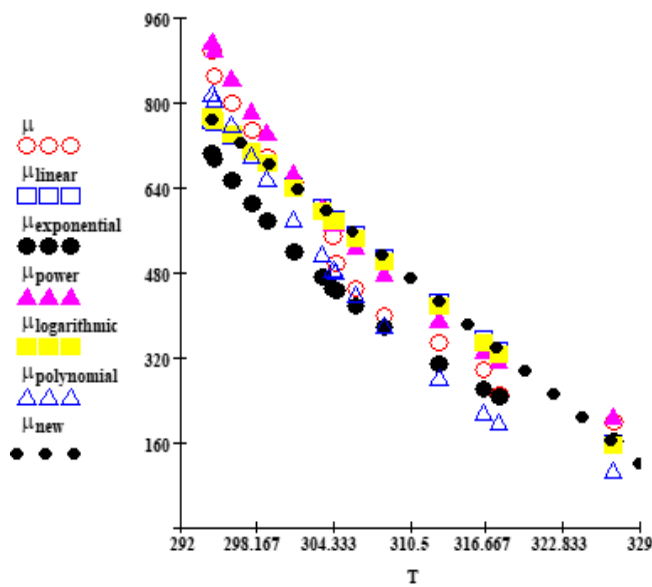

Figure 6: Soybean oil-based polyols
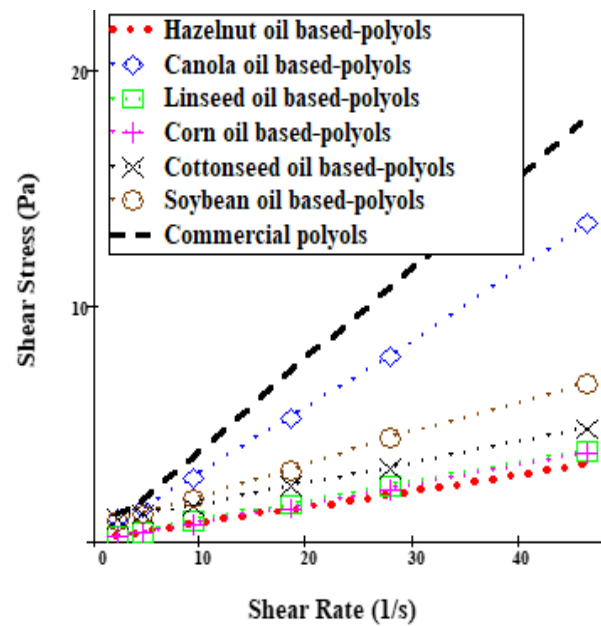
Figure 7: Commercial polyols

Figure 8: Shear stress vs. shear rate

RESULTS AND DISCUSSION

In this study, the temperature dependence of the viscosity of the vegetable oil-based polyols; model equations compared with experimental data. In Figures: 1, 2, 3, 4, 5, 6 and 7; the variations of apparent viscosities of polyols as a function of temperature were examined by using various model equations which were compared with experimental results. Operating temperatures of the assay were measured by raising temperature stepwise in a water bath. The viscosities of vegetable oil-based polyols were measured by different rotational speeds at an increasing order. According to the experimental results regression coefficients of model equations (4), (5), (6), (7), (8) and (9) were determined.

In present study, variations of viscosities of soybean oil, cottonseed oil, corn oil, hazelnut oil, canola oil, linseed oil-based polyols and commercial polyols were determined a function of temperature. As expected that the viscosity of the fluid decreases as temperature increases. The tested polyols showed Newtonian and non- Newtonian fluids behavior at certain temperature range.

As can be seen in Figures (1), (2), (3), (4), (5), (6) and (7) the viscosities of all types polyols irrespective of their production sources decrease substantially with increasing temperature. Heating may rupture molecular entanglement and bonds, which may stabilize the molecular structure and reduce the effect of molecular volume in the vegetable oil-based polyols. In other words, as temperature increases, thermal energy of molecules increase and molecular distance develops due to reduction of intermolecular forces, hence viscosity of the fluid decreases.

When thermal energy of molecules increases, molecular entanglement aligns easily and molecular structure stabilizes quickly since the molecules with high thermal energy move over one another easily.

As can be seen in Figure 8 the highest viscosity belongs to the commercial polyols while the lowest viscosity belongs to the polyol obtained from the raw hazelnut oil. The viscosities of polyols from high to low can be put in order as $\mu_{commercial} > \mu_{canola} > \mu_{soybean} > \mu_{cottonseed} > \mu_{Linseed} > \mu_{corn} > \mu_{hazelnut}$, here $\mu_{commercial}$, μ_{canola}, $\mu_{soybean}$, $\mu_{cottonseed}$, $\mu_{Linseed}$, μ_{corn} and $\mu_{hazelnut}$ denote the viscosities of commercial polyol and polyols obtained from raw canola oil, soybean oil, cottonseed oil, linseed oil, corn oil and raw hazelnut oil, respectively. Furthermore, it can be seen that all types of polyols show almost Newtonian behavior.

The regression coefficients and correlation coefficients of each model equation for each polyol obtained from different vegetable oils are given Tables 1., high values of R-squared were obtained for polynomial model irrespective of polyols obtained sources. Moreover, the new (suggested) model has the highest values for R-squared.

In addition, density of vegetable oil based-polyols was measured to be 880 and 910 kg/m^3.

The petroleum-based polyols and vegetable-based polyols have different hydroxyl numbers. The hydroxyl numbers of vegetable-based polyols were optimized by varying temperature, reaction time and catalyst.

The model equations and experimental data were compared with one another in terms of the temperature dependent-apparent viscosities of vegetable oil-based polyols. According to the experimental data; the linear and non-linear regression were made to determine coefficients of regression in the model equations.

REFERENCES

1. Andersson A, Lundmark S, Magnusson A, Maurer FHJ. Vibration and Acoustic Damping of Flexible Polyurethane Foams Modified with a Hyper Branched Polymer. Journal of Cellular Plastics. 2009; vol.01, pp. 01-21.

3. Armenta JLR, Heinze T, Martinez AMM. New Polyurethane Foams Modified with Cellulose Derivatives. European Polymer Journal. 2004; vol. 40, pp. 2803-2812.

4. Bashirzadeh R, Gharehbaghi A. An investigation on reactivity, mechanical and fire properties of PU flexible foam. Journal of Cellular Plastics.2009; vol. 01, pp. 01-30.

5. Bian XC, Tang JH, Li ZM. Flame retardancy of whisker silicon oxide/rigid polyurethane foam composites with expandable graphite. Journal of Applied Polymer Science.2008; vol. 110, pp. 3871-3879.

6. Bian XC, Tang JH, Li ZM. Flame retardancy of hollow glass microsphere/rigid polyurethane foams in the presence of expandable graphite. Journal of Applied Polymer Science. 2008; vol. 110, pp. 3871-3879.

7. Han DS, Park IB, Kimi MH, Noh BJ, Kim WS, Lee JM. The effects of glass fiber reinforcement on the mechanical behavior of polyurethane foam. Journal of Mechanical Science and Technology. 2010; vol. 24, pp. 263-266.

8. Indennidate L, Cannoletta D, Lionetto F, Greco A, Maffezzoli A. Nanofilled polyols for viscoelastic polyurethane foams. Society of Chemical Industry. 2009; vol. 59, pp. 486-491.

9. Lubguban AA, Tu YC, Lozada ZR, Hsieh FH, Suppes GJ. Noncatalytic polymerization of ethylene glycol and epoxy molecules for rigid polyurethane foam applications. Journal of Applied Polymer Science. 2009; vol. 112, pp. 2185-2194.

10. Meng XY, Ye L, Zhang XG, Tang PM, Tang JH, Ji X, Li ZM. Effects of expandable graphite and ammonium polyphosphate on the flame-retardant and mechanical properties of rigid polyurethane foams. Journal of Applied Polymer Science.2009; vol. 114, pp. 853-863.

11. Mello D, Pezzin SH, Amico SC. The effect of post-consumer pet particles on the performance of flexible polyurethane foams. Polymer Testing. 2009; vol. 28, pp. 702-708.

Modeling of Solid-liquid Extraction of Total Phenolics from *Capsicum annium L.*

This article was produced from a poster or oral contribution to the ICAIE Congress, 2017.

Sibel YİĞİTARSLAN[*][1]

[1]Department of Chemical Engineering, Suleyman Demirel University, 32260 Isparta, Turkey

Abstract: In this paper, the extraction kinetics of gallic acid equivalent of polyphenols from *Capsicum annium* was investigated. Ethanol was used as a solvent for extraction at different temperatures and the extraction medium was set at mixed and unmixed conditions to observe the changes in the kinetics. Two different strategies were applied for modeling. In the first one, four different models; namely Peleg, Mass Transfer, Logarithmic, and Page's Models were used for mathematically describing the physicochemical behavior of the extraction. The yields of extraction ranged from 1.39-3.27 mg/g depending on the extraction conditions. Mass transfer was found the best model representing the experimental data. Molecular and effective diffusivities were calculated. In the second strategy, extraction was modeled with the aid of response surface methodology. Extraction yield surface showed a linear relation with temperature, time, and solid-to-liquid ratio. The optimum conditions of extraction were 70°C, 90 minutes and 1/50 g/ml, and 3.29 mg/g gallic acid equivalent of total phenolics were extracted at those conditions. The model equations of this process could contribute to optimize the industrial extraction process and design of drug-delivery systems.

Keywords: Extraction; modeling; polyphenols; gallic acid; response surface methodology.

*Corresponding author. E-mail: yildizsibel@sdu.edu.tr

INTRODUCTION

In recent years, several researchers have been focused on polyphenols in vegetables, fruits and herbs due to their contribution to human health. Phenolic compounds are capable of scavenging free radicals (1, 2), and are known as antioxidants (3). Gallic acid, quercetin, kaempferol and catechin are well known phenolics (4-6), and they have been used especially in cancer treatments (7, 8). One of the herbs containing gallic acid is *Capsicum annium L.* (red pepper) from Solanaceae family. It contains calcium, phosphorus, sodium, iron, B_1, B_3, C vitamins, lipids, carbohydrates, proteins, fibers and organic compounds producing its characteristic color (9). Researchers had been analyzed its phenolic content by HPLC analysis in detail (10, 11). The amount and the type of phenolic components in a plant material depend on not only genotype, maturation and growth conditions of the plant (12-14), but also the type and conditions of extraction.

The studies on extraction of phenolics from *Capsicum annium* focused on application of different type of solvents including pure methanol (15), methanol-water mixture (12, 16), pure ethanol (13, 14). In those papers, since they paid attention to the types of flavonoids in a plant, they analyzed the extracts after hydrolyzing them. When extraction temperature was increased up to 65^oC, the increase in the extraction yield was observed because of the increase in stability of phenolics due to non-enzymatic reactions (15).

All of the literature deals with the types of flavonoids in the plant, and there is scarce data on modeling of the extraction process of them. Mathematical modeling of the extraction is a useful engineering tool which facilitates the understanding, optimization, design and control of the processes with minimal time and energy consumption. There are two types in modeling of a process; namely mathematical models and Response Surface Methodology. Several equations have been proposed in the literature for mathematical modeling (17-20) and it seems that the best model differs due to the plant material and the extraction conditions. Response surface method is a combination of statistical and mathematical techniques used for analyzing several independent variables and also interactive effects among the variables on the response (21). This method has been used in several different optimizations including adsorption, extraction, fermentation etc. in an efficient manner (22-26). The advantages of the method are reduced number of experimental runs, cost and time (27, 9). In addition, the final equation found by this method can adaptable to any situation faced in the industry. There is not any research aiming to combine these two method for comparison within a special extraction case.

This study aimed to obtain a model equation by applying two procedures for optimization of extraction of phenolics from *Calendula officinalis*. Peleg's, Page's, mass transfer and logarithmic models were applied in mathematical modelling. The molecular and convective diffusion

coefficients were determined. In addition, response surfaces were constructed and the influences of temperature, solid-to-liquid ratio, and time on extraction yields were analyzed.

MATERIAL AND METHODS

Material

In the experiments of classical extraction, *Capsicum annium L.* was purchased from the herbalist has capable of growing this plant itself. Ethanol, Folin-Ciocalteu, and sodium carbonate were at analytical grade, and bought from Sigma-Aldrich.

Solvent extraction

Ethanolic extraction was realized batch-wise in a 250 mL Erlenmeyer flask. Extraction temperature, solid-to-liquid ratio, and mixing rate were chosen as the parameters of single- and multiple-parameter experimental designs. At the end of the specified extraction conditions the content of the flask was filtered through 110 mm filters (FilterLab) and filtered samples were used for total flavonoid analysis.

Determination of total phenolics

The concentrations of the total polyphenols in the extracts filtered were determined using the Folin-Ciocalteu method. In the analysis 0.4 ml of the extract was mixed with 5.1 ml of distilled water and 0.5 ml of Folin ciocalteu reagent. 1.5 ml of sodium carbonate solution (20% by weight) was added into the medium immediately and after mixing they kept in dark during two hours at room temperature. The color resulted from the colorimetric reaction between gallic acid in the sample and the Folin reagent was analyzed by UV-vis spectrophotometer (Perkin-Elmer) at 765 nm. The gallic acid equivalents (GAE) of total phenolics were calculated from the calibration curve (Absorbance = 0.01532 x Concentration (µg/ml); $R^2=0.9989$) and the results were expressed as mg GAE/g dry herb.

Extraction kinetics

Peleg's model: Since the extraction curves (concentration of phenolics vs. time) have similar shape with the sorption curves, all of the extraction processes could be described with a non-exponential equation of Peleg (17):

$$c_t = c_0 + \frac{1}{K_1 + K_2 t}$$

(1)

where c_t is the concentration of phenolics at time t (mg GAE/g), c_0 is the initial concentration of phenolics at time t=0 (i.e. $c_0=0$ in all experiments), t is the extraction time, K_1 is Peleg's rate constant (min.g/mg GAE), and K_2 is Peleg's capacity constant (g/mg GAE). In that equation, K_1 relates to the extraction rate (B_o) at the very beginning of the extraction (t=t_0):

$$B_0 = \frac{1}{K_1} \qquad (\text{mg GAE/g}) \tag{2}$$

and K_2 relates equilibrium concentration (c_{eq}) at t→∞:

$$c_{eq} = \frac{1}{K_2} \qquad (\text{mg GAE/g}) \tag{3}$$

Page's model: Another model used for the mathematical modeling of the extraction proposed by Page as follows (19):

$$c_t = \exp(-kt^n) \tag{4}$$

where k and n are the constants of Page's Model, and all the other parameters have the same definitions.

Logarithmic model: In mathematical modeling of extraction processes, Logarithmic model can also be used as follows:

$$c_t = a \, \text{Log} t + b \tag{5}$$

where a and b are the logarithmic model constants.

Mass transfer model: Extraction occurs through two steps; Firstly, the solvent penetrates into the solid to dissolve the extractable material, and then the extractable material diffuses from inside the solid to the bulk liquid. The rate determining step of the overall process is the diffusion (28). The rate of this step under unsteady-state conditions is defined by Fick's second law as:

$$\frac{\partial c}{\partial t} = D \, \frac{\partial^2 c}{\partial x^2} \tag{6}$$

where, c is the concentration of the solute (mg/g), t is time (min), D is the diffusion coefficient (m^2/min), and x is the distance of diffusion. This equation is valid when very dilute solution is used in the extraction and the diffusivity is assumed to be constant (29). If the shapes of the solid particles are assumed to as perfect spheres having the same properties and also if the perfect mixing of the solid-liquid medium occurs, the time of mass transfer at infinity, the general solution of this equation becomes:

$$\text{Ln} \left(\frac{c_\infty}{c_\infty - c} \right) = 0.498 + \frac{9.87Dt}{R^2} \tag{7}$$

where, c is the concentration of the extracted material in the solution at time t (mg/g), c_∞ is the concentration of the extracted material at time t=∞, and R is the characteristic distance (m); i.e. for spheres it is equal to the radius. This equation can be rewritten as:

$$\text{Ln} \left(\frac{c_{eq}}{c_{eq} - c} \right) = a + K_{obs} t \tag{8}$$

Since c_∞ is considered as equilibrium concentration, a is a constant (0.498), and

$$K_{obs} = \frac{9.87D}{R^2}$$

(9)

In this research, Equation 8 was used to fit the experimental data and to obtain a, K_{obs} and diffusion coefficient values.

Validity of model prediction: The consistency between the predicted and experimental data evaluated by using the coefficient of determination (r^2), which is defined as:

$$r^2 = 1 - \frac{\sum_{i=1}^{n}(y_i - y_{model})^2}{\sum_{i=1}^{n}(y_i - y_{mean})^2}$$

(10)

where, n is the number of samples, y_i is the actual experimental data of the ith sample, y_{model} is the model-fitting data of the ith sample, and y_{mean} is the mean value of all experimental data. A high r^2 value indicates high consistency between the fitted and experimental data.

Response surface methodology

In designing the experiments, firstly, the potential design factors of extractions, namely extraction temperature, solid-to-liquid ratio, time and mixing rate were studied to determine the most effective three parameters on the extraction yield by single-parameter procedure. It was found that mixing rate was not as effective as the other parameters (data not shown). Then, Box-Behnken design (BBD) was constructed for analysis of multi-parameter effects. The highest levels of respective parameters producing the highest yield were chosen as the center point values (coded as "0" in Table 1) of the optimization of the extraction, while the least and the highest values were used as minimum and maximum points (coded as "-1" and "+1" in Table 1), respectively. The chosen independent variables were coded according to (1).

Table 1. Levels and codes of experimental parameters used in Box-Behnken Design (BBD)

Parameters	-1	0	+1
x_1: Temperature (°C)	30	50	70
x_2: Time (min)	30	60	90
x_3: Solid/liquid (g/mL)	1/30	1/40	1/50

$$x_i = \frac{x_i - x_0}{\Delta x}$$

(11)

where x_i is the dimensionless coded value of ith independent variable, x_0 is the value of x_i at the center point, and Δx is the step change value. The behavior of the system is explained by the following second-order polynomial model:

$$Y = \beta_0 + \sum_{i=1}^{k} \beta_i x_i + \sum_{i=1}^{k} \beta_{ii} x_i^2 + \sum_{i=1}^{k-1} \sum_{j=2}^{k} \beta_{ij} x_i x_j + \epsilon \tag{12}$$

where Y is the predicted response, x_i, x_j,...,x_k are input variables, which affect the response Y, x_i^2, x_j^2,...,x_k^2 are the square effects, β_0 is the intercept term, $x_i x_j$, $x_j x_k$ and $x_i x_k$ are the interaction effects, β_i (i = 1, 2, . . . , k) is the linear effect, β_{ii} (i = 1, 2, . . . , k) is the squared effect, β_{ij} (i = 1, 2, . . . , k) is the interaction effect, and ε is the random error (30-31).

The Design-Expert 9.0 (Stat-Ease Inc., Minneapolis, MN, USA) software was used for regression and graphical analysis of the experimental data to fit the equations developed. Design of fifteen experiments consisting of three replicates at the central point was fitted into a polynomial model. The optimum values of the selected variables were obtained by solving the regression equation in which desired values of the process responses were set as the optimization criteria.

RESULTS AND DISCUSSION

The aim of the present study was to determine the mathematical equation fitting to the experimental results of batch extraction yields. Two different optimization methods were applied to reach this aim by plotting the values of gallic acid equivalent of total phenolics extracted versus time for different extraction conditions. In the first approach, four different mathematical relations defining the physicochemical behavior of extraction were chosen; i.e.; Peleg's, Mass transfer, Logarithmic, and Page's equations. The models were statistically analyzed and compared with their respective determination of coefficient (r^2) value. The constants of respective models and their r^2 values were summarized in Table 2.

As it can be seen from Table 2, Peleg's model was not as successful as other methods applied. Mass transfer model produced the highest value of determination of coefficient and the a-values were close to its exact value of 0.498. Although, values of determination of coefficient in mass transfer, logarithmic and Page's models were all acceptable, it seemed that logarithmic model caused more reliable results than the others because it produced nearly the same values for regression coefficients under different extraction conditions. In the literature, different models were found as the best model on the kinetic analysis of extraction depending on the different plants and extractable materials (19, 32-34). It is impossible to compare the kinetic results of this research with the one in the literature that focused on the extraction of total phenolics from *Capsicum annium* since there is not any research focusing on it.

Table 2. Model parameters of extraction kinetics

Peleg's model			
	K_1	K_2	r^2
70°C-molecular	3.0392	0.3048	0.8414
70°C-convective	1.1899	0.326	0.7463
Mass transfer model			
	K_{obs}	A	r^2
70°C-molecular	0.0361	0.4247	0.9804
70°C-convective	0.0370	0.5534	0.9187
Logarithmic model			
	A	b	r^2
70°C-molecular	1.2769	0.5614	0.9662
70°C-convective	1.1163	1.0375	0.9146
Page's model			
	K	n	r^2
70°C-molecular	0.2338	0.3723	0.9704
70°C-convective	0.4461	0.2227	0.9723

In the detailed analyses of the models, results were employed by plotting the calculated values of concentrations for each model and their respective experimental values (Figures 1-8) vs. time. As it was expected from its lower r^2 value, high discrepancies between concentrations estimated by Peleg's equation and experimental data were observed in both molecular (unmixed extraction medium; Figure 1) and convective extractions (mixed extraction medium; Figure 2). Comparing the other three models, the excellent fitness between the experimental data obtained under unmixed extraction medium conditions at 70°C and estimated concentrations of phenolics were obtained by mass transfer model (Figure 3). Either in logarithmic or Page's model equations caused less (especially in logarithmic model; Figures 5 and 6) or higher estimated values under all conditions (Figures 7 and 8). Figures clearly showed that, extraction yield increases rapidly at the beginning of extraction due to high driving force (concentration difference between solid and solvent), and that this increase getting lesser as the time passes due to decrease in driving force. In each case, extraction was reached equilibrium at the end. This behavior is explained by the mass transfer model appropriately. From Equation 9, the molecular and convective diffusion coefficients were calculated as $2.67.10^{-10}$ m^2/s and $2.73.10^{-10}$ m^2/s by using the average diameter of the particle size of 0.27 mm, respectively. According to the results, a 2.2% increase of diffusion coefficient with mixing was observed. This result was in accordance with the single-parameter effect analysis in which mixing rate was found less effective than the other parameters on extraction yield. In addition, the yields were determined as 3.11 mg GAE/g and 3.27 mg/GAE for molecular and convective extractions, respectively. As a result, the increase in diffusion coefficient yielded nearly 5% increases in extraction.
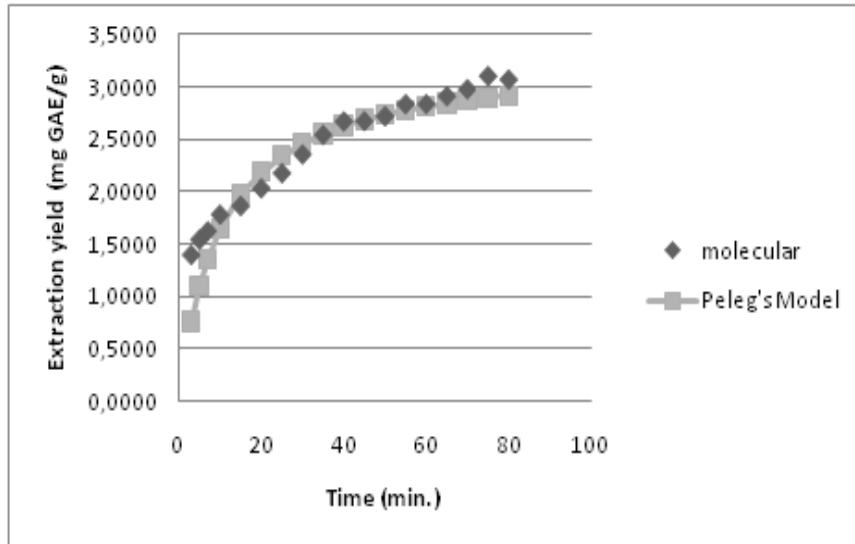
Figure 1. Experimental data obtained at 70°C under unmixed extraction medium fitted to Peleg's Model.
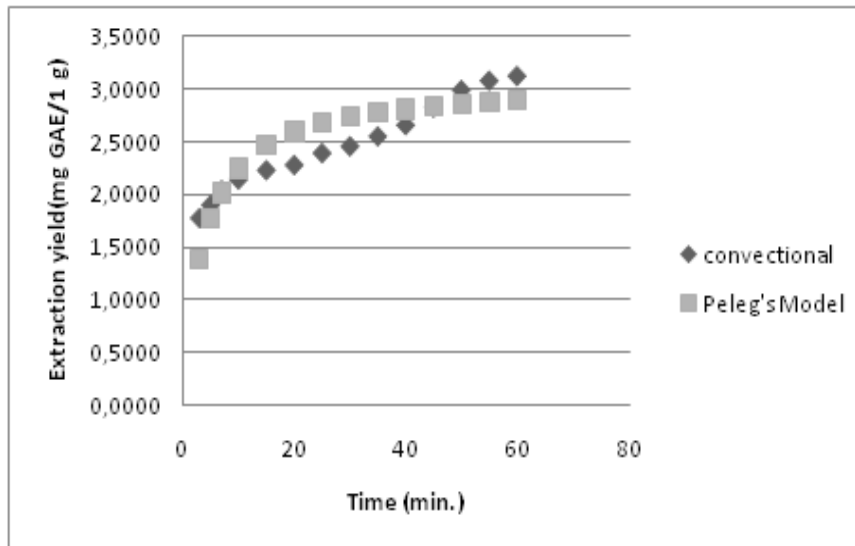

Figure 2. Experimental data obtained at 70°C under mixed extraction medium fitted to Peleg's Model.
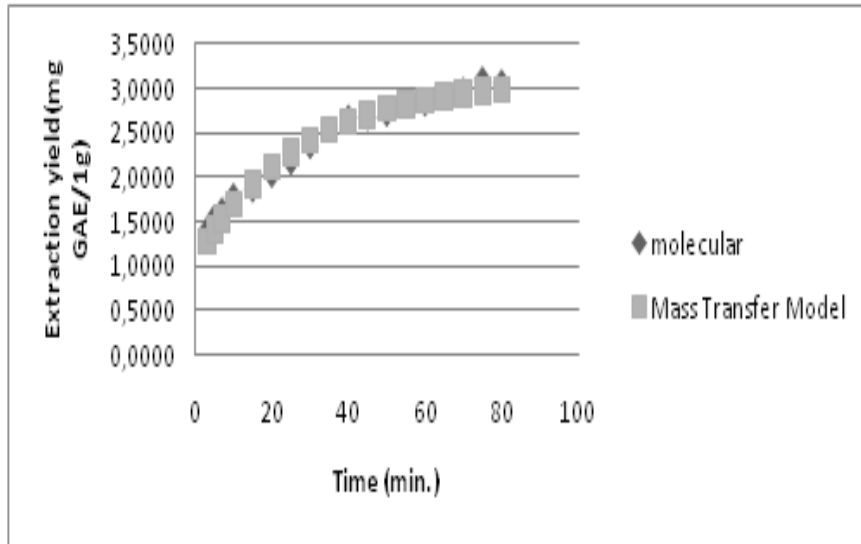
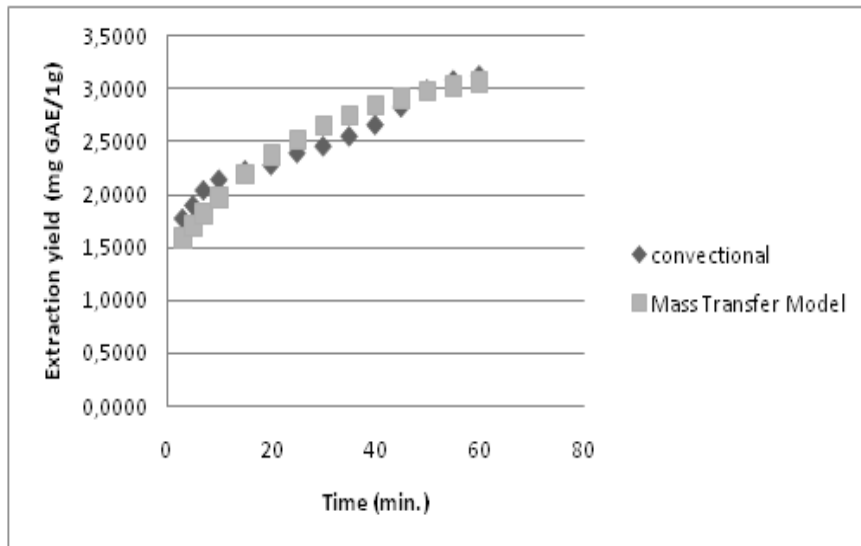**Figure 3.** Experimental data obtained at 70°C under unmixed extraction medium fitted to Mass Transfer Model.

Figure 4. Experimental data obtained at 70°C under mixed extraction medium fitted to Mass Transfer Model.
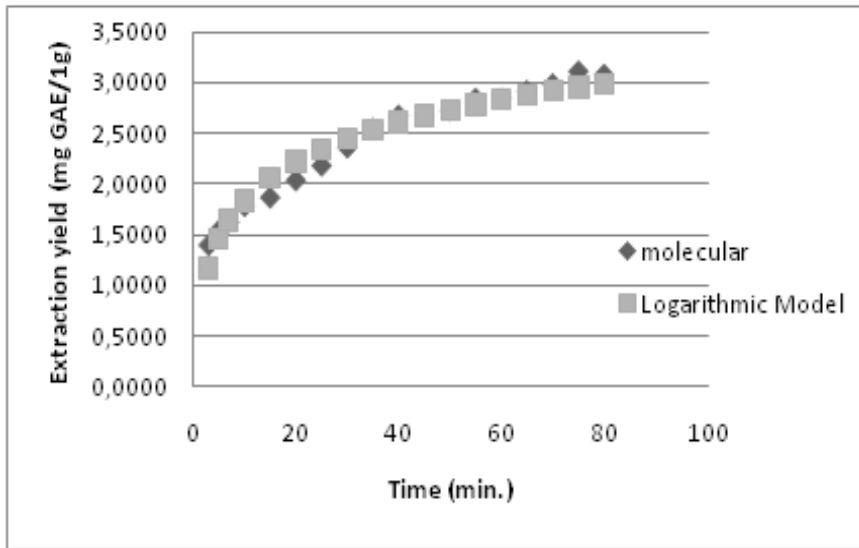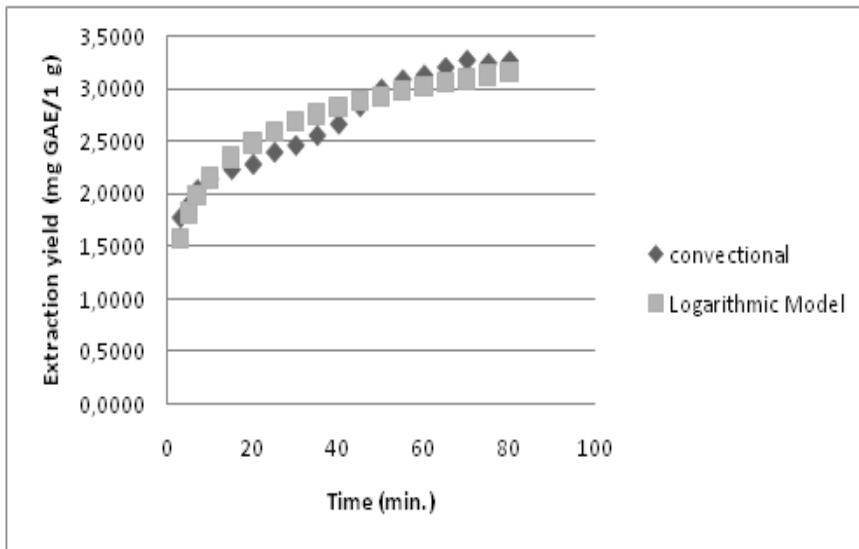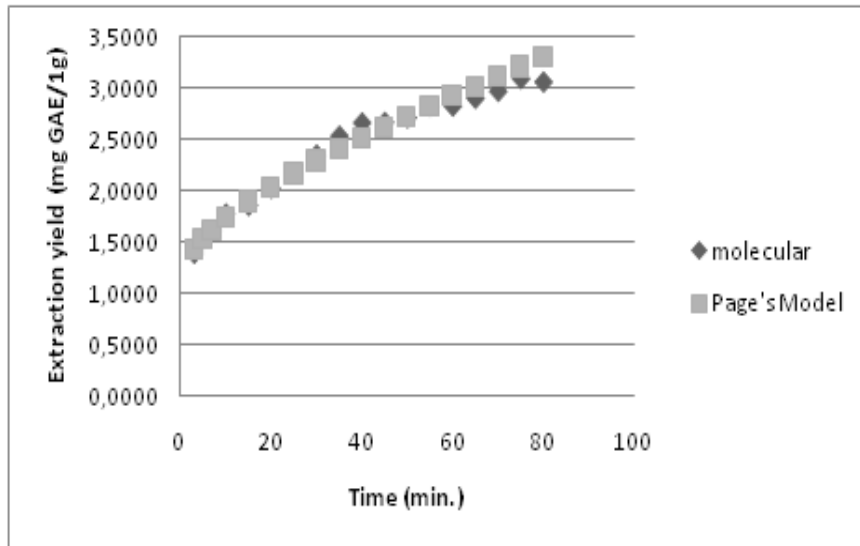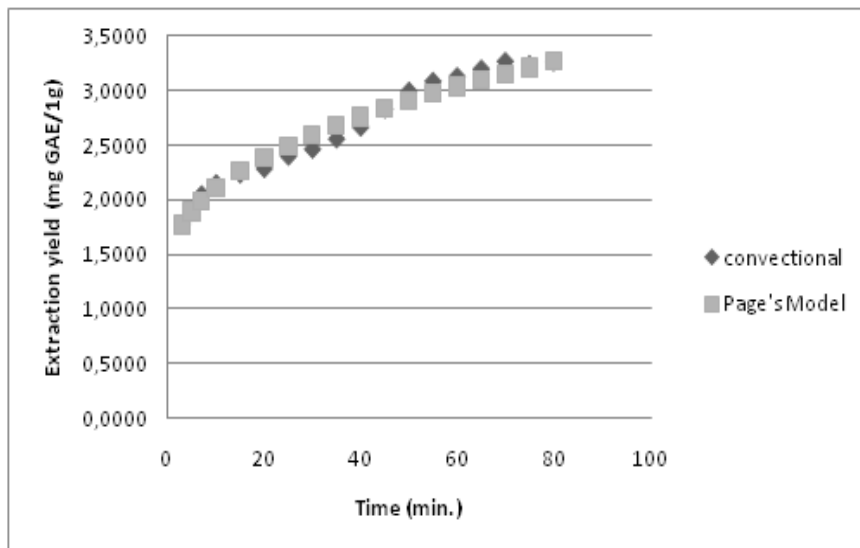
Figure 5. Experimental data obtained at 70°C under unmixed extraction medium fitted to Logarithmic Model.

Figure 6. Experimental data obtained at 70°C under mixed extraction medium fitted to Logarithmic Model.

Figure 7. Experimental data obtained at 70°C under unmixed extraction medium fitted to Page's Model.

Figure 8. Experimental data obtained at 70°C under mixed extraction medium fitted to Page's Model.

In the second procedure of optimization of extraction, three-parameter three-level Box-Behnken design applied within response surface methodology. In the study, the calculated values of gallic acid equivalents of phenolics (Table 3) at respective conditions were entered into the Design-Expert 9.0 software. In the experiments the yield of extraction ranged from 1.45 to 3.30 mg GAE/g depending on the extraction conditions. The standard deviation of experimental results at the center points was 2.2%. All of the suggested functions were investigated by applying statistical analysis of the program, and the linear model was found to be the best function (Table 4) representing the extraction surface of the total polyphenols from *Capsicum annium*. In this decision, the highest regression coefficient ($R^2 = 0.9834$), and the highest fitness in between the experimental data (actual) and their respective calculated values of the function (predicted) were

considered (Figure 9). The symmetrical relationship between them (Figure 9) approved the applicability of the function chosen. Generally, second order polynomials found the most appropriate functions when response surface methodology was applied to the systems (28-29). This observation results from the interrelation of parameters on the process response. In this study, the interactive effects between parameters were so low that the linear relations were found as enough for presentation of the extraction surface. This was approved by the statistical analysis of software function in which showing the model as "significant", and lack of fit as "insignificant" (Table 4). The larger the F value and the smaller the p value, the higher the effect of the parameter on the extraction of the flavonoids of this plant. So, the dominant parameter was determined as temperature, whereas the least effective parameter was solid-to-liquid ratio. This result showed that at the extraction conditions, liquid had capable of dissolving all of the phenolic compounds in the solid.

At this point, three-dimensional response surfaces were constructed in this study by using software. The interactive effects of the parameters were shown in Figures 10-12. In those, red regions shows the highest amount of total flavonoids extracted, yellow and blue parts represent the lower and much lower extraction yields than those. As it can be seen from figures, extraction temperature must be in the coded range of [0.5;1] for the highest flavonoid extraction.

Table 3. Experimental design and yields of extraction

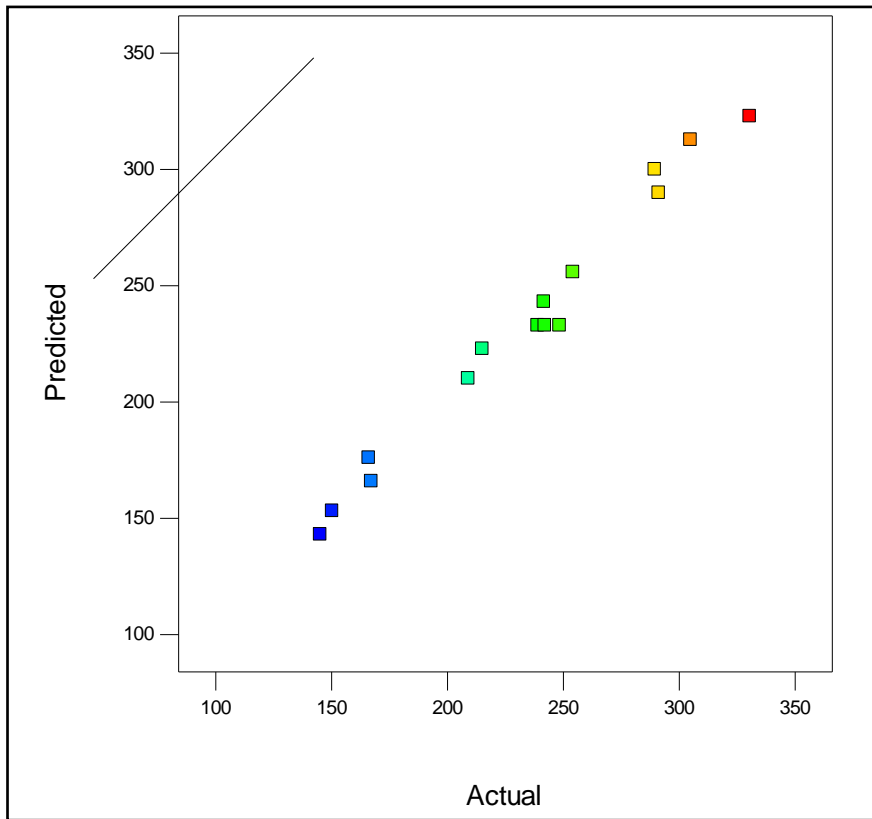| No	x_1	x_2	x_3	Amount of gallic acid (mg/100g)
1	-1	-1	0	145,175
2	1	-1	0	291,206
3	-1	1	0	166,080
4	1	1	0	330,475
5	-1	0	-1	150,299
6	1	0	-1	289,531
7	-1	0	1	167,194
8	1	0	1	304,941
9	0	-1	-1	209,034
10	0	1	-1	241,636
11	0	-1	1	215,123
12	0	1	1	254,214
13	0	0	0	248,468
14	0	0	0	238,997
15	0	0	0	242,102

Figure 9. Experimental results and extimated values of linear function of response surface model.

Table 4. ANOVA table

Source	Sum of Squares	df	Mean Square	F Value	p-value Prob > F
Model	45629,32	3	15209,77	217,39	< 0.0001
A-Temperature	43130,87	1	43130,87	616,45	< 0.0001
B-Time	2173,68	1	2173,68	31,07	0,0002
C-Solid/liquid	324,77	1	324,77	4,64	0,0542
Residual	769,63	11	69,97		
Lack of Fit	723,01	9	80,33	3,45	0,2451
Pure Error	46,62	2	23,31		
Core Total	46398,95	14			

Model: Significant; Lack of fit: Not significant; R-Squared: 0.9834;

Adjusted R-Squared: 0.9789; Predicted R-Squared: 0.9722
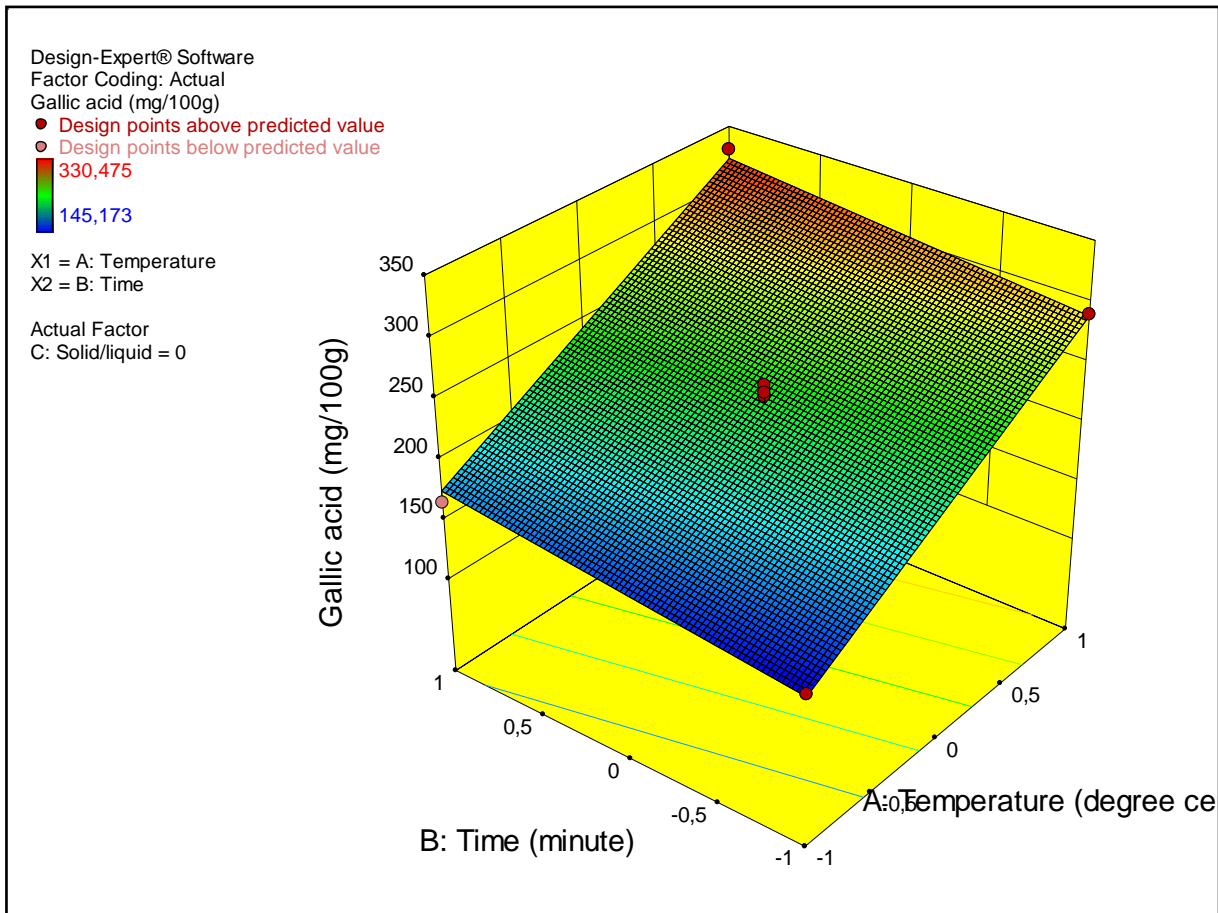
Figure 10. Three-dimensonal response surface of extraction yield depending on time and temperature.
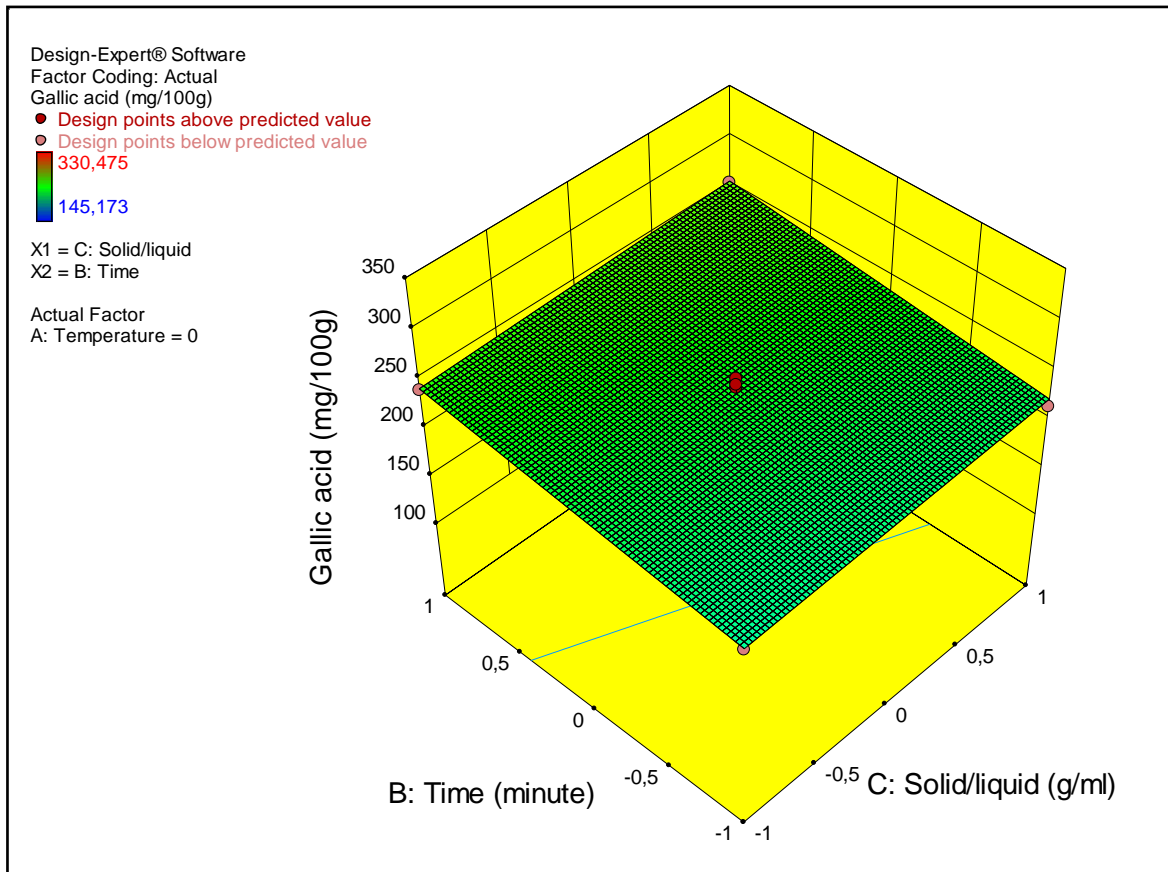
Figure 11. Three-dimensonal response surface of extraction yield depending on time and solid/liquid ratio.
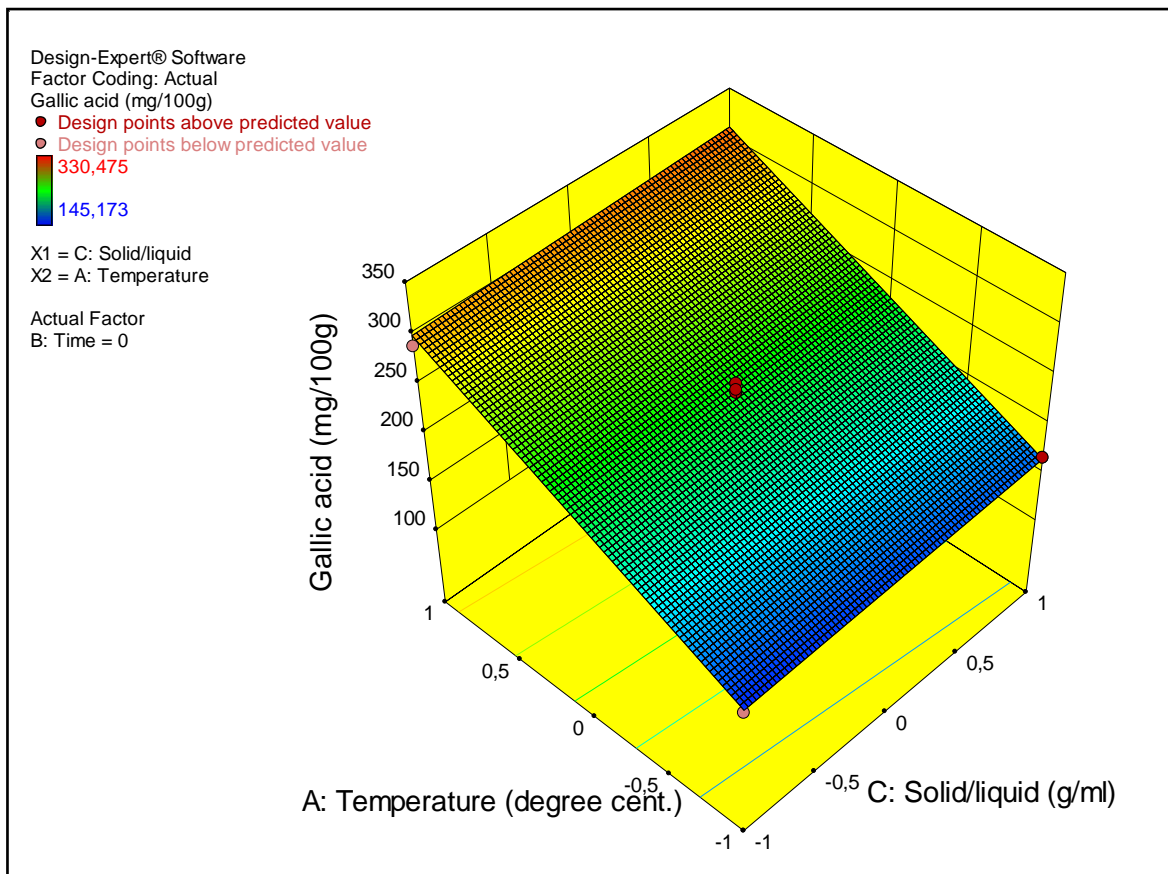
Figure 12. Three-dimensonal response surface of extraction yield depending on temperature and solid/liquid ratio.

As a result, the emprical relation explaining the response surface was found as:

Gallic acid (mg/100g)

$$= +232.96487 + (73.42587). \text{temperature} + (16.48363). \text{time}$$

$$+ (6.37150). (^{\text{solid}}/_{\text{liquid}}) \tag{13}$$

Finally, the required extraction conditions were analyzed by using this equation and numerical analysis section of the software. In the analysis, restrictions of the parameters were selected as "in range" (has a meaning that they are in the experimental range), and the response criterion was determined as "max". As a result of the multi-parameter optimization, the optimum conditions producing the highest yield (5.29 mg GAE/g) were determined as 70°C, 90 minutes, 1/50 g/mL.

CONCLUSION

This research investigated the extraction of gallic acid equivalents of total phenolics of red pepper. At the experimental conditions of the study, the yield and kinetics of solid-liquid extraction were influenced especially by temperature. The extracted total phenolics were in the range of 1.39-3.27 mg GAE/g. Mass transfer model found as the most suitable model for the extraction kinetics of phenolics from red pepper. Temperature increased the diffusion coefficients. The results of this work could contribute in the optimization of extraction of total phenolics from *Capsicum annium* and in the design of drug-delivery systems including them in where the same value of diffusion coefficient may be more "natural" to the human body cells.

REFERENCES

1. X. Deng, H. Song, Y. Zhou, G. Yuan and F. Zheng. Effects of quercetin on the profileration of breast cancer cells and experession of surviving in vitro. Experimental and Therapeutic Medicine. 2013; 6(5); 1155-1158.

2. Z. Liu, D. Li, L. Yu and F. Niu. Gallic Acid as a cancer-selective agent induces apoptosis in pancereatic cancer cells. Chemotherapy. 2012; 58(3); 185-98.

3. J. P. Cornard and J. C. Merlin Jacobs. Spectroscopic and structural study of complexes of quercetin with Al(III). Journal of Inorganic Biochemistry. 2002; 92; 19-27.

4. J. W. Higdon and B. Frei. Tea catechins and polyphenols: health effects, metabolism and antioxidant functions. Critical Reviews in Food Science and Nutrition. 2003; 43(1); 89-143.

5. L. Pavun, P. Durdevic, M. Jelikic-stankov, D. Dikanovic, A. Ciric and S. Uskokovic-Markovic. Spectrofluorimetric determination of quercetin in pharmaceutical dosage forms. Macedonian Journal of Chemistry and Chemical Engineering. 2014; 33; 209-215.

6. H.H. Ho, C.S. Chang, W.C. Ho, S.Y. Liao, C. H. Wue and C. J. Wanga. Anti-metastasis effects of gallic acid on gastric cancer cells involves inhibition of NF-kB activity and downregulation of PI3 K/AKT/small GTPase signals. Food and Chemical Toxicology. 2010; 48; 2508-2516.

7. G.R. Cleonice, C. D. Borges, R. C. Zambiazi, M. R. Nunes, E. V. Benvenutti, S. R. da Luz, R. F. D'avila and J. K. Rutz. Microencapsulation of gallic acid in chitosan, β-cyclodextrin and xanthan. Industrial Crops and Products. 2013; 46; 138-146.

8. V.R. Punithhavathi, P.S.M. Price, R. Kumar and J. Selvakumari. Antihyperglycaemic antilipid peroxidative and antioxidant effects of gallic acid on streptozotonic induced diabetic Wistar rats. European Journal of Pharmacology. 2011; 650; 465-471.

9. A. Akgül. Baharat bilimi ve teknolojisi. Gıda Teknolojisi Derneği Yayınları; 1993; No:15; 106-115.

10. M. Materska and I. Perucka. Antioxidant activity of the main phenolic compounds isolated from hot pepper fruit (Capsicum annuum L.). Journal of Agricultural and Food Chemistry. 2005; 53(5); 1750-1756.

11. A. Marin, F. Ferreres, F. A. Tomas- Barberan and M. I. Gıl. Characterization and quantitation of antioxidant constituents of sweet paper (Capsicum annuum L.). Journal of Agricultural and Food Chemistry. 2004; July; 10.1021/f0497915.

12. Y. Lee, L. R. Howard and B. Villalon. Flavonoids and antioxidant activity of fresh pepper (Capsicum annuum) cultivars. Journal of Food Science. 1995; 60; 473-476.

13. N. Deepa, C. Kaur, B. George, B. Singh and H. C. Kapoor. Swiss society of food science and technology. Elsevier; 2005; 121-129.

14. W-R. Kim, E.O. Kim, K. Kang, S. Oidowsambuu, S. H. Jung, B.S. Kim, C. W. Nho and B-H. Um. Antioxidant activity of phenolics in leaves of three red peper (Capsicum annuum) cultivars. Journal of Agricultural and Food Chemistry. 2014; 62; 850-859.

15. N.Y. Shotorbani, R. Jamei and R. Heidari. Antioxidant activities of two sweet pepper Capsicum annuum L. varieties phenolic extracts and effects of thermal treatment. Avicenna Journal of Phytomedicine. 2012; 3(1); 25-34.

16. A.L. Medina-Juarez, D. M. A. Molina-Quijada, C. L. D. Toro-Sanchez, G. A. Gonzalez-Aguilar and N. Gamez-Meza. Antioxidant activity of peppers (Capsicum annuum L.) extracts and characterization of their phenolic constituents. Interciencia. 2012; 37; 588-593.

17. M. Peleg. An empirical model for the description of moisture sorption curves. Journal of Food Science. 1988; 53; 1216-1219.

18. J. Cranck. The mathematics of diffusion. Claredon Press, Oxford; 1975.

19. S. Jokic, D. Velic, M. Bilic, A. Bucic-Kojic, M. Planinic and S. Tomas. Modelling the process of solid-liquid extraction of total polyphenols from soybeans. Czech Journol of Food Science. 2010; 28(3); 206-212.

20. D. F. Othmer and W. A. Jaatinen. Extraction of soybeans. Industrial and Engineering Chemistry Research. 1959; 51; 543-546.

21. D. M. Amirah, R. Prassad and M.R. Khan. Comprarison of extraction techniques on extraction of gallic acid from stem bark of Jatropha curcas. Journal of Applied Sciences. 2012; 12(11); 1106-1111.

22. H. Turkyilmaz, T. Kartal and S. Yildiz Yigitarslan. Optimization of lead adsorption of mordenite by response surface methodology: characterization and modification. Journal of Environmental Health Science and Engineering. 2014; 12(1); doi:10.1186/2052-336X-12-5.

23. M. Dashtianeh, A. Vatanara, S. Fatemi and F. Sefidkon. Optimization of supercritical extraction of Pimpinella affinis ledeb. using response surface methodology. Journal of CO2 Utilization. 2013; 3-4; 1-6.

24. L. Levin, V. L. Papinutti. Optimization of lignocellulolytic enzyme production by the white-rod fungus Trametes trogii in solid-state fermentation using response surface methodology. Biochemical Engineering Journal. 2008; 39(1); 207-214.

25. C. Zhao, W. Ying-long, X. Xiao-jie and L. Jie and L. Qiang. Optimization of schizothorax prenanti tchang protein enzymatic hydrolysis technology by response surface methodology. Science and Technology of Food Industry. 2012; 2.

26. L. Sun, S. Wan, Z. Yu and L. Wang. Optimization and modeling of preparation conditions of TiO2 nanoparticles coated on hollow glass microspheres using response surface merhodology. Separation and Purification Technology. 2014; 125; 156-162.

27. C. Pal, S. Bindu, S. Dey, A. Alam, M. Goyal, M. S. Iqbal, P. Maity, S. S. Adhikari and U. Bandyopadhyay. Gallic acid prevents nonsteroidal anti-inflammatory drug-induced gastroathy in rat by blocking oxidative streaa and apoptpsis. Free Radical Biology and Medicine. 2010; 49; 258-267.

28. Y. C. Cheung, K. C. Siu and J. Y. Wu. Kinetic models for ultrasound-asisted extraction of water-soluble components and polysaccharides from medicinal fungi. Food and Bioprocess Technology. 2012; 6; 2659-2665.

29. J. E. Cocae and G. Mazza. Mass transfer process during extraction of phenolic comounds from milled berries. Journal of Food Engineering. 2003; 59; 379-389.

30. Y. Zhao, Y. Hou, G. Tang, E.Cai, S. Liu, H. Yang, L. Zhang, S. Wang. Optimization of ultrasonic extraction of phenolic compounds from Epimedium brevicornum Maxim using response surface methodology and evaluation of its antioxidant activities in vitro. Journal of Analytical Methods in Chemistry. 2014; Article ID 864654; 7 pages; doi:10.1155/2014/864654.

31.   Z. Sun, R. Su, J. Qiao, Z. Zhao and X. Wang. Flavonoids extraction from Taraxacum officinale (Dandelion): Optimization using response surface methodology and antioxidant activity. Journal of Chemistry. 2014; Article ID 956278, 7 pages, 2014. doi:10.1155/2014/956278.

32. M. M. Poojary and P. Passamonti. Extraction of lycopene from tomato processing waste: Kinetics and modeling. Food Chemistry. 2015; 173; 943-950.

33. M. S. Guerrero, J. S. Torres and M. J. Nunez. Extraction of polyphenols from white distilled grape pomace: Optimization and modeling. Bioresource Technology. 2008; 99; 1311-1318.

34. A. Bucic-Kojic, M. Planinic, T. Srecko, M. Bilic and D. Velic. Study of solid-liquid extraction kinetics of total polyohenols from grape seeds. Journal of Food Engineering. 2007; 81; 236-242.

Investigation of the Dissolution Behaviors in Different Solvents of the Zinc and Manganese Powders Obtained from the Spent Alkaline Batteries

This article was produced from a poster or oral contribution to the ICAIE Congress, 2017.

Gülistan DENİZ, Turhan ÖZDEMİR, Nizamettin DEMİRKIRAN*

Department of Chemical Engineering, İnonu University, Malatya, Turkey

Abstract: In this study, after the zinc and manganese powders were individually obtained from the spent alkaline batteries, their dissolution behaviors in different solvents were examined to determine the appropriate leaching reagent for each species. The aqueous solutions of the sodium hydroxide, ammonia, ammonium chloride, ammonium acetate, acetic acid, sulfuric acid, and hydrochloric acid were used as the leaching reagents with the aim of dissolving the zinc and manganese powders. In the dissolution experiments, the values of the concentration of relevant reagent, reaction temperature, solid to liquid ratio, stirring speed, and particle size were fixed at 1 mol/L, 40 °C, 0,5/500 g/mL, 500 rpm, and -40+50 mesh, respectively. It was determined that the hydrochloric acid was more effective reagent for both powder samples. The dissolution extent of manganese powder in the hydrochloric acid solutions was found to be 41,5% after 120 minutes of reaction time. It was observed that the zinc powder was completely dissolved in the hydrochloric acid solutions in 20 minutes of reaction time.

Keywords: Dissolution; Spent Battery; Zinc; Manganese.

Cite this: Deniz G, Özdemir T, Demirkıran N. Investigation of the Dissolution Behaviors in Different Solvents of the Zinc and Manganese Powders Obtained from the Spent Alkaline Batteries. Journal of the Turkish Chemical Society, Section B: Chemical Engineering. 1(Sp. is. 1):61–68.

*Corresponding author. E-mail: nizamettin.demirkiran@inonu.edu.tr

INTRODUCTION

The recycling of various industrial and domestic solid wastes has been a popular research area from both environmental and economical perspectives in recent years. Among the solid wastes, the spent batteries are considered as hazardous wastes due to the heavy metal content of their. Zinc-carbon and alkaline zinc-manganese dioxide batteries are widely used because of the versatility, low maintenance, favorable electrical properties/price ratio and its requirements by the electronic industry. These batteries are consumed in very large quantities due to its wide range of uses, and consequently, much waste containing metal are generated. The storage of these wastes in private areas can be a way out to reduce the environmental pollution. However, number of this kind of special storage spaces are limited, and the disposal costs can be very high. Therefore, the recovery of the major metal values of waste batteries can appear to be a more beneficial way to prevent the environmental pollution and decrease the consumption of raw material used in battery production. Thereby, the spent batteries may be evaluated as secondary sources of zinc and manganese because they contain a high amount of metal (1-3).

Pyrometallurgical and hydrometallurgical methods are usually applied for recovering metals from the waste batteries. The hydrometallurgical treatment of the spent batteries is more environmentally suitable and economical when compared with pyrometallurgical technique. The hydrometallurgical processing consists of mainly three steps, including leaching, solution purification, and metal recovery. The most important step in this processing technique is probably the leaching stage, which is a mass transfer operation, because the recovery efficiency depends on effective implementation of this stage. In the leaching step, the metal values in the waste battery powder are transferred from solid powder to solution medium by means of an aqueous solution. The yield of leaching process is affected by various factors, such as the type of solvent, reaction temperature, solid-to-liquid ratio, stirring speed, and particle size. In the treatment of the spent battery powders by applying hydrometallurgical process, aqueous solutions of acidic and alkaline chemicals are generally utilized as leaching agent. For this aim, the aqueous solutions of sulfuric acid (4,5), hydrochloric acid (6), sodium hydroxide (7,8), ammonia (9) and ammonium acetate (10) have been used to dissolve the zinc and manganese in the waste battery powder.

In the alkaline zinc-manganese dioxide batteries, the zinc and manganese dioxide are used the anode and cathode materials, respectively. A simple schematic representation of an alkaline battery is shown in Figure 1. Finely powdered zinc metal is in the form of paste together with potassium hydroxide serving as electrolyte. The anode and cathode materials are separated by a separator, and they do not mix with each other. Thus, these

components in the spent alkaline battery powder can be individually obtained. Taking advantage of this feature of alkaline batteries, the zinc and manganese in the waste battery powder can be separately dissolved in an aqueous solution and recovered. Accordingly, the determination of individual dissolution behavior of these species in the waste powder is an important subject in terms of the leaching yield, design of leaching reactor, and separation and recovery steps of hydrometallurgical process.

In this study, after the zinc and manganese powders were individually obtained from the spent alkaline batteries, their dissolution behaviors in different solvents were examined to determine the appropriate leaching reagent for each species.
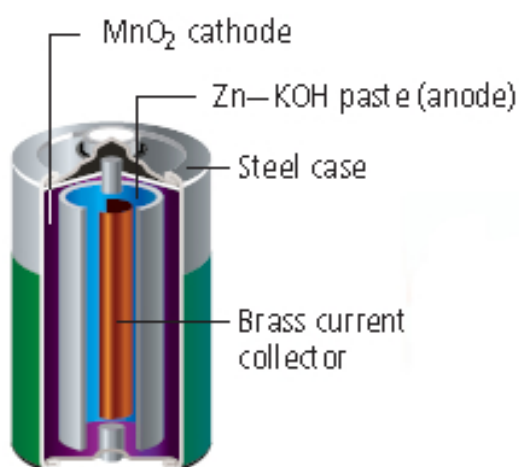
Figure 1. Schematic representation of an alkaline battery.

EXPERIMENTAL

The waste alkaline batteries used in this experimental study were collected in Malatya Province, Turkey. The collected waste batteries were shredded manually and the parts containing the zinc and manganese was separated from each other and other components of battery. After this procedure, the zinc and manganese powders were individually obtained. The battery powders prepared were dried at room temperature. The dried powders were sieved using standard sieves to prepare different particle size fractions. The mineralogical analysis of the battery powder samples were performed by using a Rigaku RadB-DMAX II model X-ray diffractometer. The results of the X-ray analyses are given in Figure 2 for the zinc powder and Figure 3 for the manganese powder. The dissolution tests were carried out in a 1 L jacketed glass reactor equipped with a mechanical stirrer, a temperature control unit, and a back-cooler. The aqueous solutions of the sodium hydroxide, ammonia, ammonium chloride, ammonium acetate, acetic acid, sulfuric acid, and hydrochloric acid were applied as the leaching reagents with the aim of dissolving the

zinc and manganese powders. After putting 500 mL of aqueous solution of relevant reagent into the glass reactor and bringing it to operating reaction temperature, a given amount of the zinc or manganese powder was added to the solution, and the stirring speed was set. The dissolution process was performed for various reaction times. Aliquots of 5 mL sample were taken at regular intervals during the dissolution process, and it was filtered. The filtered samples were analyzed complexometrically for the zinc or manganese ions content using Titriplex III solution as titrant and puffertabletten as indicator. In the dissolution experiments, the values of the concentration of relevant reagent, reaction temperature, solid-to-liquid ratio, stirring speed, and particle size were fixed at 1 mol/L, 40 °C, 0,5/500 g/mL, 500 rpm, and -40+50 mesh, respectively.

The zinc or manganese amount passing into the solution was calculated as follows:

x= mass of metal ion passing to the solution/mass of metal in the battery powder sample.
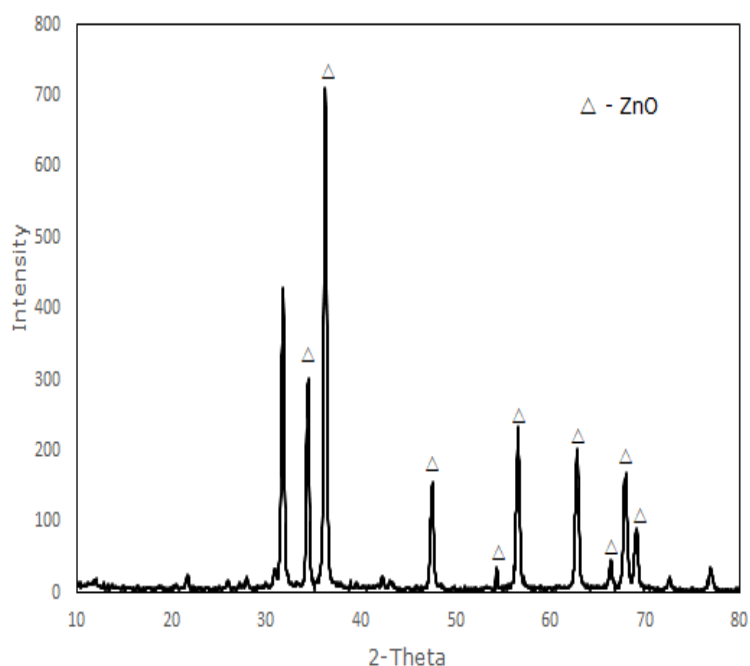
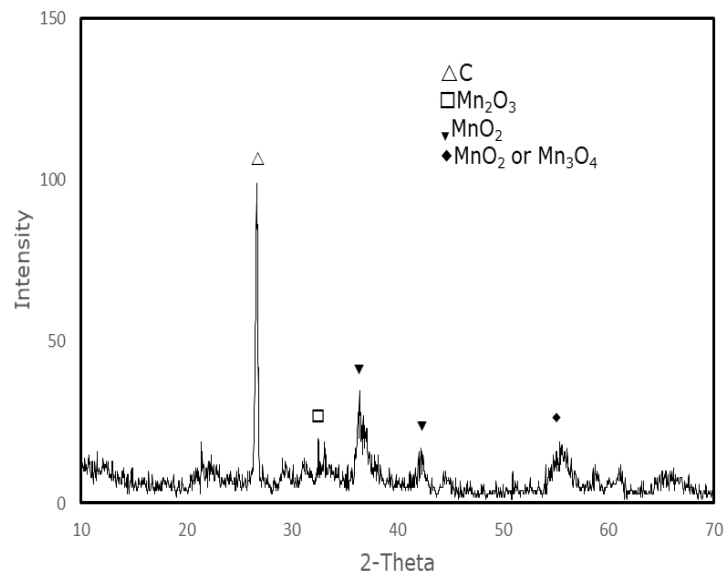**Figure 2.** X-ray diffraction pattern of the zinc powder.

Figure 3. X-ray diffraction pattern of the manganese powder

RESULTS AND DISCUSSIONS

As mentioned above, in an alkaline zinc-manganese dioxide battery, the anode and cathode materials are the powdered zinc metal and manganese dioxide powder, respectively. A concentrated solution of KOH is used as electrolyte solution. During the discharge of battery, the metallic zinc powder is oxidized according to Eq. 1 while the manganese dioxide is reduced in accordance with reaction shown in Eq. 2.

$$Zn + 2OH^- \rightarrow ZnO + H_2O + 2e^- \tag{1}$$
$$2MnO_2 + H_2O + 2e^- \rightarrow Mn_2O_3 + 2OH^- \tag{2}$$

A simplified overall battery reaction can be written as follows considering the anode and cathode reactions given above.

$$Zn + 2MnO_2 \rightleftharpoons ZnO + Mn_2O_3 \tag{3}$$

Thus, the spent alkaline zinc-manganese dioxide batteries contain mainly Zn, ZnO, MnO_2, and Mn_2O_3. If it is thought that the batteries are extremely consumed, it can be understood how much metal is found in the generated waste. Therefore, the recovery of metallic values from the spent batteries is a highly important issue especially in terms of economy. The solubility of a solid material in aqueous solutions varies from solvent to solvent. A solid material may generally easily dissolve in the strong and less acidic solutions while it may

not readily dissolve in basic solutions. Some solid materials may sufficiently dissolve in basic solutions while some of them may dissolve in sufficient amount in both acidic and basic solutions. Therefore, the determination of an appropriate solvent for the dissolution process is a significant matter to reach the adequate yield.

The zinc oxide containing part of the waste battery powder dissolves in both acidic and basic solvents because of the amphoteric characteristic of zinc. The leaching reagents used in this study are the strong acid (sulfuric acid and hydrochloric acid), strong base (sodium hydroxide), weak acid (acetic acid and ammonium chloride), weak base (ammonia), and neutral salt (ammonium acetate). In aqueous solution of these reagents, the dissolution reactions of solid zinc oxide can be simply written as follow.
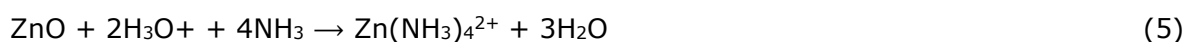
$ZnO + 2OH^- \rightarrow ZnO_2^{2-} + H_2O$ (4)
(in NaOH solution)
$ZnO + 2H_3O+ + 4NH_3 \rightarrow Zn(NH_3)_4^{2+} + 3H_2O$ (5)
(in ammonium acetate, ammonia and ammonium chloride)
$ZnO + 2H_3O^+ \rightarrow Zn^{2+} + 3H_2O$ (6)
(in sulfuric acid, hydrochloric acid and acetic acid)

The dissolution results of zinc powder in the solution mentioned above are given in Figure 4. As can be seen from Figure 4, the zinc powder was dissolved more or less in all solution utilized as reagent. The highest dissolution was observed in hydrochloric acid solution.

The manganese oxides containing part of the waste battery powder was also dissolved in both acidic and basic solvents. For the dissolution of manganese oxides, the following reactions equations can be simply written.

$2MnO_2 + 3NaOH \leftrightarrows Na_3MnO_4 + MnOOH + H_2O$ (7)
$Mn_2O_3 + H_2SO_4 \rightarrow MnO_2 + MnSO_4 + H_2O$ (8)

The dissolution results of manganese powder are given in Figure 5. As can be seen from Figure 5, the dissolution of manganese powder is at very low levels in the solutions of sodium hydroxide, ammonia, ammonium chloride, and ammonium acetate and can be practically ignored. The value of the highest dissolution was reached in the hydrochloric acid solution.

It can be observed from the experimental results that the manganese powder does not practically dissolve in basic medium while the zinc powder dissolves in basic solutions. This

feature can provide an advantage for the leaching process of the waste battery powders. The manganese and zinc in the waste batteries can be selectively leached using a basic solution. Thus, the leach solution with low impurities can be obtained for the step of the metal recovery of the hydrometallurgical process.
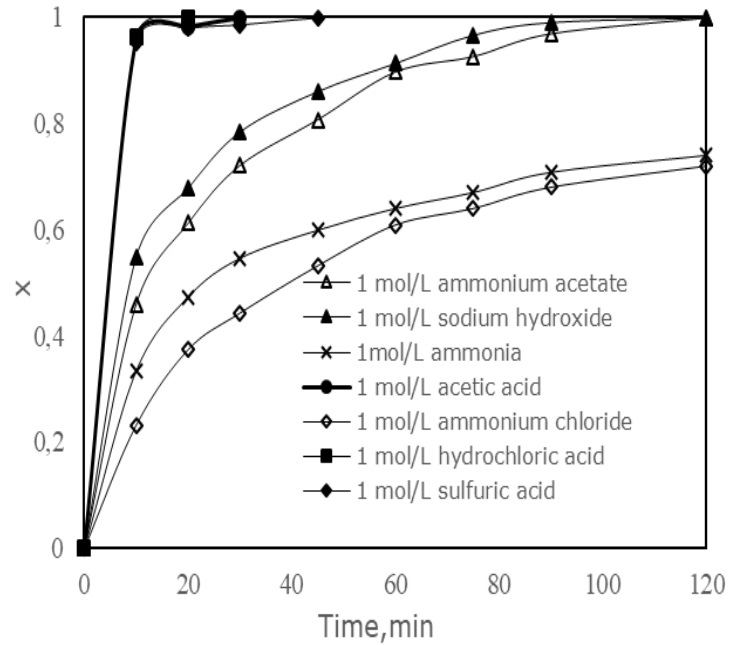

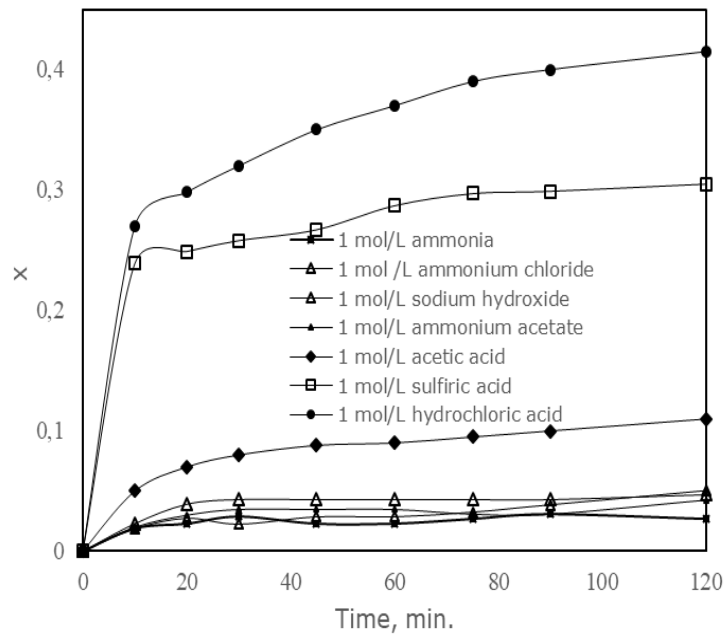**Figure 4.** Effect of solvents on solvent dissolution for zinc powder.

Figure 5. Effect of solvents on solvent dissolution for manganese powder.

CONCLUSIONS

In this study, the manganese and zinc powders in the spent alkaline batteries were separately obtained, and they were dissolved by using different leaching reagents. It was determined that the zinc powder dissolved at satisfactory amounts in all reagents while the manganese powder dissolved at remarkable amounts in the hydrochloric acid and sulfuric acid solutions. It was observed that the hydrochloric acid was more effective reagent for both powder samples. According to the results obtained, it can be said that the zinc and manganese in the waste alkaline batteries could be selectively dissolved and recovered by applying hydrometallurgical treatment.

REFERENCES

1. Jaapar J, Ahmad W.A. Recovery of valuable metals from dry cell batteries. International Conference on Environment 2006 (ICENV 2006). 13-15 November 2006; Penang, Malaysia.

2. De Souza C.C.B.M., De Oliveria D.C., Tenorio J.A.S, Characterization of used alkaline batteries powder and analysis of zinc recovery by acid leaching, J Power Sources, 2001; 103:120-126. DOI:10.1016/S0378-7753(01)00850-3.

3. Sayılgan E, Kukrer T, Yigit N.O., Civelekoglu G., Kitis M. Acidic leaching and precipitation of zinc and manganese from spent battery powder using various reductants, J Hazard Mater 2010; 173:137-143. DOI:10.1016/j.jhazmat.2009.08.063.

4. Gega J, Walkowiak W. Leaching of zinc and manganese from used up zinc-carbon batteries using aqueous sulfuric acid solution, Physicochem Probl Miner Process, 2011; 46:155-162. DOI:10.5277/ppmp120203.

5. Buzatu M, Saceanu S, Petrescu M.I., Ghica G.V., Buzatu T. Recovery of zinc and manganese from spent batteries by reductive leaching in acidic media, J Power Sources, 2014; 247:612-617. DOI:10.1016/j.jpowsour.2013.09.001.

6. El Hazek M.N., Lasheen T.A., Helal A.S. Reductive leaching of manganese from low grade sinai ore in HCl using H2O2 as reductant, Hydrometallurgy, 2006;84:187-191.DOI: 10.1016/j.hydromet.2006.05.006.

7. Shin S.M., Senanayake G, Sohn J, Kang J, Yang D, Kim T. Separation of zinc from spent zinc-carbon batteries by selective leaching with sodium hydroxide, Hydrometallurgy, 2009; 96:349-353. DOI:10.1016/j.hydromet.2008.12.010

8. Buzatu T, Popescu G, Birloaga I, Saceanu S. Study concerning the recovery of zinc and manganese from spent batteries by hydrometallurgical processes, Waste Manage, 2013; 33:699-705. DOI:10.1016/j.wasman.2012.10.005.
9. Senanayake G, Shin S.M., Senaputra A, Winn A, Pugaev D, Avraamides J, Sohn J.S., Kim D.J. Comparative leaching of spent zinc-manganese-carbon batteries using sülfür dioxide in ammoniacal and sulfuric acid solution, Hydrometallurgy, 2010; 105:36-41. DOI: 10.1016/j.hydromet.2010.07.004.

10. Demirkıran N. Examination of the use of ammonium acetate as lixivilant in recovery of Zn from waste batteries and kinetic analysis, Environ Eng Manag J, 2015; 14:51-56. http://www.eemj.icpm.tuiasi.ro

Investigation of the Chemical Exergy of Torrefied Lignocellulosic Fuels using Artificial Neural Networks

This article was produced from a poster or oral contribution to the ICAIE Congress, 2017.

Ugur Özveren[1,*] , **Omer Faruk Dilmac[2]**, **Mehmet Selcuk Mert[3]** , **Fatma Karaca Albayrak[1]**

[1]Marmara University, Engineering Faculty, Chemical Engineering Department, Kadikoy, Istanbul, 34722, Turkey
[2]Cankiri Karatekin University, Engineering Faculty, Chemical Engineering Department, Fatih, Cankiri, 18200, Turkey
[3]Yalova University, Engineering Faculty, Energy Systems Engineering Department, Merkez, Yalova, 77200, Turkey

Abstract: Torrefaction is a type of thermo-chemical pretreatment process to enhance energy density of lignocellulosic fuels. For a torrefaction process, a key challenge is to develop efficient thermal conversion technologies for torrefied fuels which can compete with fossil fuels. The calculation of chemical exergy is an essential step for designing efficient thermal conversion systems. However, there is a few correlations to predict the chemical exergy of solid fuels has been published so far. This study deals with a new method to characterize the chemical exergy of different kinds of torrefied lignocellulosic fuels by using Bayesian trained artificial neural network (ANN). The proposed model based on proximate analysis and higher heating values of torrefied fuels. Use of the artificial neural network method is encouraged to reduce variance in model results. The results indicate that the proposed model offers a high degree of correlation (R^2=0,9999) and its robustness and capability to compute the chemical exergy of any torrefied lignocellulosic fuels from its proximate analysis and heating value.

Keywords: Lignocellulosic fuels; Chemical exergy; Proximate analysis; Neural networks.

INTRODUCTION

Environmental and economic concerns of fuel supply have been motivating the torrefied fuel for thermal conversion systems. Torrefaction is a thermochemical process in which raw biomass is heated under atmospheric pressure, at a temperature range of 200–300 °C, in the absence of oxygen or under low oxygen concentrations (1). An efficient technology for torrefaction process which can produce torrefied fuel to substitute fossil fuels is a key challenge. Exergy analysis is commonly accepted as the most natural way to evaluate the performance of different processes and calculation of chemical exergy is the first step of exergy evolution (2). However, there is a few correlations to predict the chemical exergy of solid fuels have been published so far. These correlations are based on ultimate analysis of fuels. However, the ultimate analysis requires very expensive equipment and highly trained analysts. The proximate analysis on the other hand only requires standard laboratory equipment and can be run by any competent scientist or engineer (3).

Artificial neural network is an effective alternative of linear and nonlinear correlations in that they can represent highly complex and nonlinear processes. Furthermore, they are quite flexible and robust against input noise and, once developed and their coefficients determined, they can provide a rapid response for a new input (4).

In this study, a new artificial neural network model was developed to evaluate the chemical exergy of torrefied biomass fuel, which is based on higher heating value and torrefied fuel content obtained by proximate analysis.

MATERIAL AND METHODS

Samples

The data of 116 torrefied biomass samples with their proximate and ultimate analysis were taken from the study of Daya Ram Nhuchhen (5), who acquired the data from previous studies in this field (6 - 16). In order to develop a predictive model, the dataset used in this study was divided into two parts: the first part for training the model and the second for assessing the estimation capability of the obtained neural network architecture (called the "testing set"). All 116 torrefied biomass samples as well as a split of the samples into a training set with 97 samples and a testing set with 19 samples were randomly selected

by using the MATLAB software. Description of torrefied biomass samples was given Table 1.

Table 1. Torrefied Biomass Samples (5).

	Minimum (%)	Maximum (%)
Oxygen (% DAF*)	7,23	44,35
Nitrogen (%DAF)	0,00	2,65
Hydrogen (%DAF)	3,24	7,50
Carbon (%DAF)	49,25	88,50
Total sulfur (%DAF)	0,00	0,26
VM (%DAF)	15,71	87,37
FC (%DAF)	12,67	84,29
HHV (MJ/kg)	16,63	33,30

*DAF = Dry Ash free VM: Volatile Matter HHV: Higher Heating Value

In order to validate the artificial neural network model, un-torrefied biomass samples from the study of Chun-Yang Yin (17) also were tested to measure the extensity of the proposed exergy model in this study. Description of biomass samples used in this study for 23 samples was given Table 2.

Table 2. Biomass Samples (17).

	Minimum (%)	Maximum (%)
Oxygen (% DAF*)	33,02	48,99
Nitrogen (%DAF)	0,30	5,49
Hydrogen (%DAF)	4,49	7,34
Carbon (%DAF)	42,26	56,73
Total sulfur (%DAF)	0,02	0,85
VM (%DAF)	71,38	87,16
FC (%DAF)	12,84	28,57
HHV (MJ/kg)	15,09	21,95

*DAF = Dry Ash free VM: Volatile Matter HHV: Higher Heating Value

Artificial Neural Networks

An ANN is a massively parallel-distributed information processing system that simulates the functions of neurons using artificial neurons inspired from the studies of the brain and the nervous system (18). An artificial neuron is the fundamental processing element of ANN and can be implemented in many different ways. The general architecture of an artificial neuron is shown in Figure 1 (18,19).
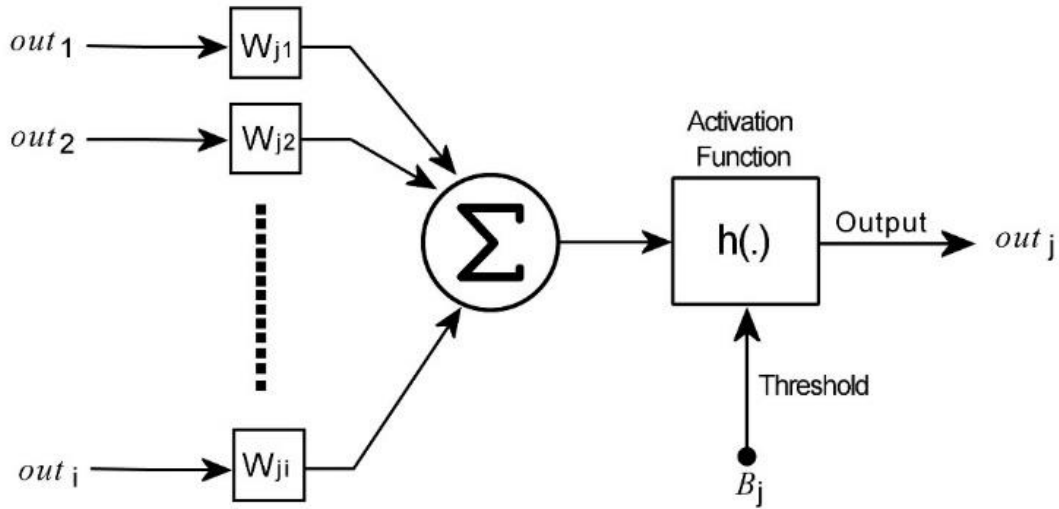
Figure 1. Architecture of an artificial neuron

In this figure, input from the output (out_i) of the preceding layer neuron is multiplied by its weight value (W_{ji}). Then, results of these multiplications are summed with bias value (B_j). The initial weights and biases are usually assigned randomly. The output of a neuron, which is in Figure 1, can be described by Equation 1.

$$out_j = h(\sum_{i=1}^{N}(W)_{ji}X_i + B_j)$$ (Eq. 1)

where h is the activation (transfer) function. The activation function can be found in different forms, either linear or non-linear. In this work, logarithmic sigmoid, h(x), function was used an activation function which defines as:

$$h(x) = 1/(1+\exp(-x))$$ (Eq. 2)

Bayesian methods are the ideal methods for solving learning problems of neural network (20), which can automatically select the regularization parameters and integrate the properties of high convergence speed of traditional BP and prior information of Bayesian statistics (21). The Bayesian Regularization method changes the error performance function by attaching a standard deviation of the weights and the thresholds (22) and can be expressed by (23):

$$F = \beta E_D + \alpha E_W$$ (Eq. 3)

where α and β are the regularization parameters. Using (Equation 3) to minimize the performance error, enables the network to possess less weights and thresholds. This is

equivalent to reducing the size of the network in such a way that it can respond smoothly, thus reducing overfitting (23).

ANN Model

The exergy value of a solid fuel is related to higher heating values and proximate analysis. Therefore, the correlation between the exergy values of torrefied fuels and their proximate analysis with higher heating values has been examined to develop an artificial neural network model. There are several classes of neural network architectures, classified according to a number of layers, neurons, and their interconnections. In this paper, we adopt a single-output three-layered BP neural network with Bayesian regularization to predict the dry ash free based chemical exergy (e_{DAF}^{CH}) of the torrefied fuels. Figure 2 presents the neural network structure of proposed model.
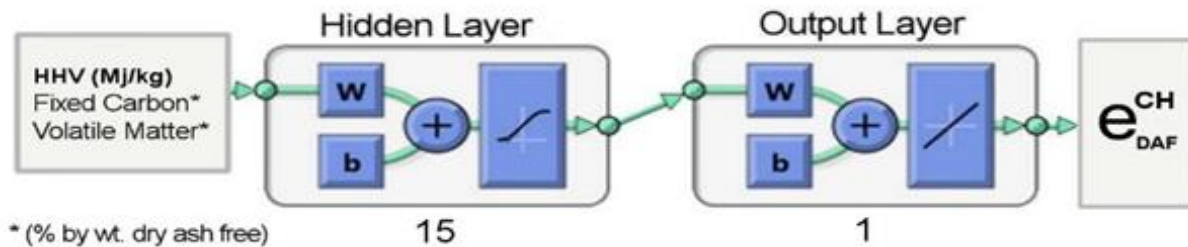

Figure 2. ANN Model

Validation of the correlations

In this study, Coefficient of determination (R^2) is employed to assess correlations for the chemical exergy of torrefied biomass, which is computed as follows:

$$R^2 = 1 - \frac{\sum_i^n (c_i - e_i)^2}{\sum_i^n (c_i - \bar{c})^2}$$
(Eq. 4)

Where e and c denote the estimated and calculated values, respectively. $\bar{c}$ is the calculated average value. R^2 is used as a universal parameter to measure the accuracy of any model. A higher R^2 value means a better estimation and fitting.

RESULTS AND DISCUSSIONS

In order to use an artificial neural network model, one needs first to train the proposed model with training dataset. Figure 3 showed the quality of fit between the chemical exergy values and predicted chemical exergy values of torrefied fuels for training dataset.
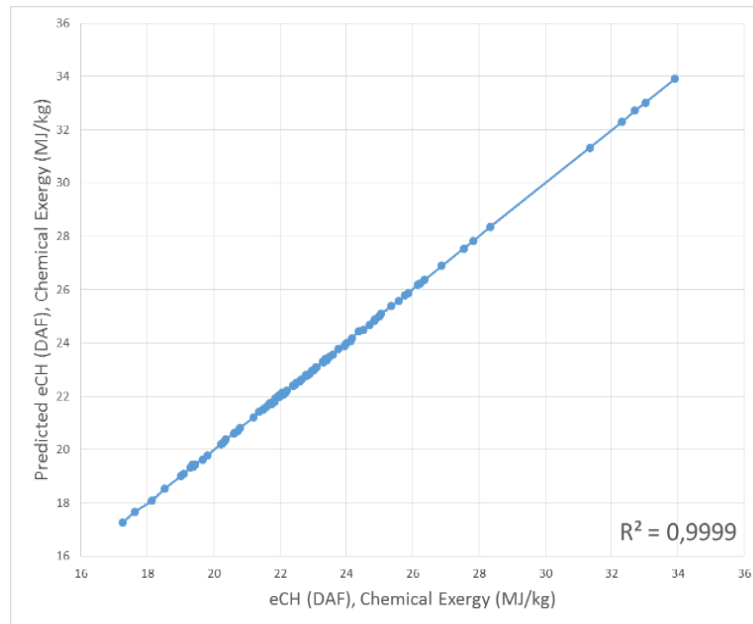
Figure 3. Training dataset

The artificial neural network model was also tested for reliability using the testing dataset (Figure 4).
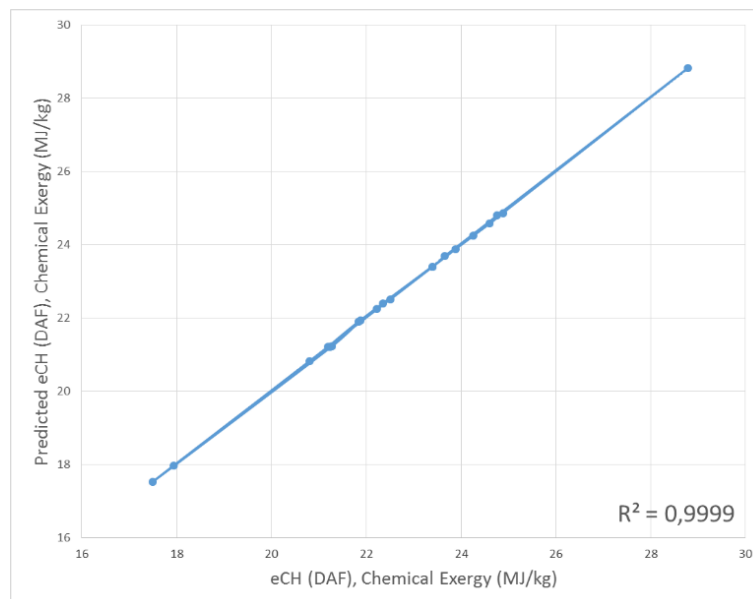

Figure 4. Test dataset

In this study, a high degree of correlation (R^2 = 0,9999) between actual and predicted chemical exergy was observed, as shown in Figure 4, for test datasets of the torrefied lignocellulosic fuels. It can thus be apprehensible that the ANN model used in this study possesses good accuracy and generalization performance.

RESEARCH ARTICLE

To ensure the capability and predictive ability of the model, biomass fuel dataset also were used for the robustness of the proposed model. Figure 5 shows plots of the chemical exergy values and corresponding ones estimated by the model in this study.

CONCLUSIONS

A model for chemical exergy prediction of lignocellulosic fuels was developed using artificial neural networks. The high R^2 values and the good fit in testing dataset lead to the conclusion that the artificial neural network model provides accurate predictions of the chemical exergy for a variety of torrefied lignocellulosic fuels. The major advantage of this model is its capability to compute chemical exergy of any torrefied fuels simply from its proximate analysis instead of ultimate analysis. Thereby provides a useful tool for exergy analysis of thermal conversion processes.

REFERENCES

1. Rousset P, Aguiar C, Labbe N, Commandre JM. Enhancing the combustible properties of bamboo by torrefaction. Bioresource Technology. 2011 Sep; 102(17): 8225-8231.

2. Song GH, Shen LH, Xiao J. Estimating Specific Chemical Exergy of Biomass from Basic Analysis Data. Industrial & Engineering Chemistry Research. 2011 Aug 17; 50(16): 9758-9766.

3. Parikh J, Channiwala SA, Ghosal GK. A correlation for calculating HHV from proximate analysis of solid fuels. Fuel. 2005 Mar; 84(5): 487-494.

4. Estiati I, Freire FB, Freire JT, Aguado R, Olazar M. Fitting performance of artificial neural networks and empirical correlations to estimate higher heating values of biomass. Fuel. 2016 Sep 15; 180: 377-383.

5. Nhuchhen DR. Prediction of carbon, hydrogen, and oxygen compositions of raw and torrefied biomass using proximate analysis. Fuel. 2016 Sep 15; 180: 348-356.

6. Arias B, Pevida C, Fermoso J, Plaza MG, Rubiera F, Pis JJ. Influence of torrefaction on the grindability and reactivity of woody biomass. Fuel Processing Technology. 2008 Feb; 89(2): 169-175.

7. Bridgeman TG, Jones JM, Williams A, Waldron DJ. An investigation of the grindability of two torrefied energy crops. Fuel. 2010 Dec; 89(12): 3911-3918.

8. Chen DY, Zhou JB, Zhang QS, Zhu XF, Lu Q. Upgrading of Rice Husk by Torrefaction and its Influence on the Fuel Properties. Bioresources. 2014 Nov; 9(4): 5893-5905.

9. Eseltine D, Thanapal SS, Annamalai K, Ranjan D. Torrefaction of woody biomass (Juniper and Mesquite) using inert and non-inert gases. Fuel. 2013 Nov; 113: 379-388.

10. Ibrahim RHH, Darvell LI, Jones JM, Williams A. Physicochemical characterisation of torrefied biomass. Journal of Analytical and Applied Pyrolysis. 2013 Sep; 103: 21-30.

11. Pala M, Kantarli IC, Buyukisik HB, Yanik J. Hydrothermal carbonization and torrefaction of grape pomace: A comparative evaluation. Bioresource Technology. 2014 Jun; 161: 255-262.

12. Pohlmann JG, Osorio E, Vilela ACF, Diez MA, Borrego AG. Integrating physicochemical information to follow the transformations of biomass upon torrefaction and low-temperature carbonization. Fuel. 2014 Sep 1; 131: 17-27.

13. Soponpongpipat N SD, Sae-Ueng U. Higher heating value prediction of torrefaction char produced from non-woody biomass. Front Energy. 2015; 9(4): 461-471.

14. Strandberg M, Olofsson I, Pommer L, Wiklund-Lindstrom S, Aberg K, Nordin A. Effects of temperature and residence time on continuous torrefaction of spruce wood. Fuel Processing Technology. 2015 Jun; 134: 387-398.

15. Wannapeera J, Fungtammasan B, Worasuwannarak N. Effects of temperature and holding time during torrefaction on the pyrolysis behaviors of woody biomass. Journal of Analytical and Applied Pyrolysis. 2011 Sep; 92(1): 99-105.

16. Wannapeera J, Worasuwannarak N. Upgrading of woody biomass by torrefaction under pressure. Journal of Analytical and Applied Pyrolysis. 2012 Jul; 96: 173-180.

17. Yin CY. Prediction of higher heating values of biomass from proximate and ultimate analyses. Fuel. 2011 Mar; 90(3): 1128-1132.

18. Ozveren U. An artificial intelligence approach to predict a lower heating value of municipal solid waste. Energy Sources Part a-Recovery Utilization and Environmental Effects. 2016; 38(19): 2906-2913.

19. Fausett LV. Fundamentals of neural networks : architectures, algorithms, and applications. Prentice-Hall; 1994 3.

20. Heydecker BG, Wu J. Identification of sites for road accident remedial work by Bayesian statistical methods: an example of uncertain inference. Advances in Engineering Software. 2001 Oct-Nov; 32(10-11): 859-869.

21. Sun Z, Chen Y, Li XY, Qin XL, Wang HY. A Bayesian regularized artificial neural network for adaptive optics forecasting. Optics Communications. 2017 Jan 1; 382: 519-527.

22. Li X, Wang DS. A Sensor Registration Method Using Improved Bayesian Regularization Algorithm. International Joint Conference on Computational Sciences and Optimization, Vol 2, Proceedings. 2009: 195-199.

23. Monteiro RVA, Guimaraes GC, Moura FAM, Albertini MRMC, Albertini MK. Estimating photovoltaic power generation: Performance analysis of artificial neural networks, Support Vector Machine and Kalman filter. Electric Power Systems Research. 2017 Feb; 143: 643-656.

EGGSHELL DERIVED NANOHYDROXYAPATITE REINFORCED CHITOSAN CRYOGEL BIOCOMPOSITES FOR TISSUE ENGINEERING APPLICATIONS

This article was produced from a poster or oral contribution to the ICAIE Congress, 2017.

Didem Demir[1] iD **, Seda Ceylan[1,2], Fatma Öfkeli[1], Duygu Şen[1], Nimet Bölgen Karagülle[1,*]**

[1]Mersin University, Engineering Faculty, Chemical Engineering Department, 33343, Mersin, Turkey
[2]Adana Science and Technology University, Bioengineering Department, Adana, Turkey

Abstract: Hydroxyapatite has a biocompatible, biodegradable and natural apatite characteristic to be used in biomedical applications such as bone tissue engineering. The objectives of this study were to synthesize hydroxyapatite from domestic waste eggshells which is utilized as pure calcium source; compare the properties of biosynthesized hydroxyapatite with commercially purchased hydroxyapatite; and produce biosynthesized hydroxyapatite reinforced chitosan cryogels for possible tissue engineering applications. Calcium oxide powders obtained after calcination of waste eggshells showed different particle sizes depending on calcination temperature. It was found that increased temperature of calcination led to the powders of smaller particle sizes. Structural changes at carbonate groups of calcined eggshell were determined by FTIR analysis. The effect of the biosynthesized hydroxyapatite on the morphology of chitosan cryogel biocomposites were determined. The changes in the chemical bond structure of the cryogels were analysed by FTIR and swelling behavior of produced chitosan cryogels was determined by swelling ratio tests.

*Corresponding author. E-mail: nimetbolgen@yahoo.com; nimet@mersin.edu.tr

INTRODUCTION

Hydroxyapatite (HAp, $Ca_{10}(PO_4)6(OH)_2$) exhibits excellent biocompatibility, biodegradability, osteoconductive and bioactive properties due to its chemically similar composition to the inorganic component of natural bone minerals (1). HAp can be produced by chemical synthesis such as sol-gel method, hydrothermal method, sono-chemical synthesis, co-precipitation and mechanochemical method or by extraction from natural sources such as corals, sea shells, animal bones and eggshells (2). The worldwide availability, unlimited supply, low cost, simple, inexpensive, economical, and efficient production are the advantages of obtaining HAp from natural biological sources (3). Eggshell is one of the major waste product of food industry, and it becomes useless after the use of egg contents and its derivatives (4). Eggshell is composed of calcium carbonate (94%), organic matter (4%), calcium phosphate (1%) and magnesium carbonate (1%) (5). In recent years, the combination of a polymeric matrice (especially made of a natural polymer) with a biocompatible, reinforcing and bioactive component like HAp has shown significant improvements as biomaterials for clinical applications (6). In this study, we aimed to obtain biosynthesized HAp (bio-HAp) from waste egg shells and combine it with chitosan cryogel scaffolds. The chitosan used in this study was extracted from the blue crap, as demonstrated in our previous study (7). The present study firstly demonstrates producing calcium oxide (CaO) powder from domestic waste eggshells (a cheap and widely available biological source in worldwide) by using a simple heat treatment process at different calcination temperatures. Then, describes the synthesis and characterization of nanometer scale bio-HAp from this CaO powder by co-precipitation method. The properties of synthesized CaO powders and bio-HAp was characterized by fourier transform infrared spectroscopy (FTIR) and dynamic light scattering (DLS) analysis. Finally, we combined bio-Hap with chitosan cryogels. The chemical structure and swelling behaviour of chitosan-HAp cryogels were demonstrated for possible tissue engineering applications.

MATERIAL AND METHODS

Material

In this study, eggshells which were collected from domestic wastes were used as starting material for the synthesis of biosynthesized HAp (bio-HAp). Phosphoric acid was obtained from Merck, Germany. The commercial HAp (com-HAp) used for the comparison of the properties of bio-HAp was purchased from Sigma Aldrich, USA. Chitosan from blue crap shells were used for the production of cryogel scaffolds. Glutaraldehyde (25%, v/v) as the crosslinker was obtained from Merck, Germany. All solution preparations and washing steps were performed by using distilled water.

Preparation of Waste Eggshells and Synthesis of CaO

Waste eggshells were first washed with tap water to remove contaminants. The cleaned eggshells were washed with distilled water and dried at 105 °C for 4 hours. The pretreated eggshells were crushed, milled and sieved to a standart powder (500 µm sieve). For CaO synthesis, powder of eggshells were calcined in an ash furnace (Protherm, Plf 130/45, Turkey) at different temperatures (400, 600, 800 and 1000 °C) for 2 hours with a heating rate of 10 °C/min. During calcination, the eggshells were converted to calcium oxide by releasing carbon dioxide (CO_2) according to following reaction:

$$CaCO_3 \rightarrow CaO + CO_2 \qquad \text{(Eq. 1)}$$

The CaO samples obtained from the eggshells were stored in an oven at 40 °C for further analysis.

Synthesis of Bio-Hap

Bio-HAp were prepared from CaO powders by co-precipitation method according to Kunjalukkal et al, 2015 (6). The calcination temperature of 800 °C was selected in order to prepare CaO powders for certainty of the complete transformation of $CaCO_3$ to CaO based on TGA results. A stoichiometric amount of CaO powder (2 grams) were weighed and hydrolysed in 250 mL of distilled water to obtain calcium hydoxide ($Ca(OH)_2$) solution as follows:

$$CaO + H_2O \rightarrow Ca(OH)_2 \qquad \text{(Eq. 2)}$$

Under continuous stirring at 1400 rpm, 1350 µL phosphoric acid solution was added drop by drop to the $Ca(OH)_2$ solution at 100 °C by using a magnetic stirrer. The expected reaction is as follow:

$$10Ca(OH)_2 + 6H_3PO_4 \rightarrow Ca_{10}(PO_4)6(OH)_2 + 18H_2O \qquad \text{(Eq. 3)}$$
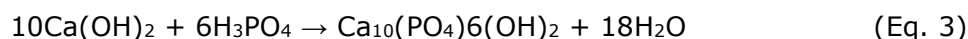
After the bubbling was finished, the mixed solution was kept on the same conditions for 2 h. The resulting solution was allowed to cool down to room temperature and the resulting precipitate was filtered out using filter paper. Wet sample was put in an oven at 40 °C for 24 h. The dried precipitate was then collected and stored.

Characterization of Synthesized CaO AND Bio-HAp

Thermogravimetric analysis, TGA/DTG of waste eggshell was carried out using Perkin Elmer Pyris 1 TGA, ABD. A total of 7.5 mg of the sample was used and TGA curve was obtained from 40 °C to 1000 °C in nitrogen atmosphere with a heating rate of 10 °C/min. FTIR (Perkin Elmer, FTIR Spectrometer Frontier ATR, USA) was used to determine the functional groups and chemical compositions of the CaO powders synthesized by the calcination of waste eggshells at different temperatures and synthesized bio-HAp at selected calcination temperature. FTIR analysis were performed at a resolution of 4 cm^{-1} in the wavelength range of 450-4000 cm^{-1}. For the characterization of particle size, the Dynamic Light Scattering (DLS) (Malvern, Nano ZS90, England) was used to measure powder particle size distribution of synthesized CaO and bio-HAp samples. The samples were dispersed in acetic acid (100% purity, Glacial).

Production of Chitosan-HAp Cryogel Biocomposites

The chitosan-HAp cryogels were synthesized at different amounts of synthesized HAp by cryogelation method. Chitosan solution (3%, w/v) was prepared in acetic acid solution (6%, v/v) and mixed on a magnetic stirrer until solution was homogenous and clear. At the end of mixing, three different ratio of synthesized HAp (1:1, 1:2, 1:3, ratio of chitosan to HAp) was added to prepared chitosan solutions. 1 mL of GA solution (3%, v/v) was added to 2 mL of prepared chitosan-HAp solution. The whole solution was immediately poured into a 2 mL plastic syringe and transferred into the cryostat. The reaction mixture was incubated in the cryostat at -16 °C for 2 h. After this period the cryogels were stored in the fridge at same conditions for 24 h. After the reaction was completed, the frozen samples in the syringe molds were thawed to room temperature and washed several times to remove the unreacted reagents. The samples were lyophilized before characterization.

Characterization of Produced Chitosan-Hap Cryogel Biocomposites

The obtained cryogels' chemical structure was analysed by FTIR in the range of 450-4000 cm^{-1}, with automatic signal gain collected in 20 scans at a resolution of 4 cm^{-1}. To determine the swelling behavior of chitosan-HAp cryogels, the samples were dried at room temperature to a constant weight (W_D). Then, dried samples were immersed in distilled water to obtain swollen cryogels. The excess water on the surface of the cryogels was removed and the samples were weighed (W_S). Swelling ratio was calculated by the following equation:

$$SR\% = ((W_S - W_D) / (W_D))*100 \qquad\qquad \text{(Eq. 4)}$$

RESULTS AND DISCUSSION

Characterization of Synthesized CaO and Bio-Hap

FTIR analysis was carried out to determine the chemical composition of the waste eggshell and CaO powders synthesized after calcination of eggshells at different temperatures. Figure 1 shows the FTIR spectra of the waste eggshell and CaO powders. The bands at between 873 and 1413 cm^{-1} were attributed to C-O bond of carbonate (CO_3) groups of eggshell. However, the CO_3 ions disappeared from the structure at high temperatures (800 and 1000 °C) during heat treatment. The intensity of the O-H stretching band observed at 3642 cm^{-1} wavelength is due to the O-H bond in $Ca(OH)_2$, which is formed during the adsorption of water by CaO (8). The peak at 2981 cm^{-1} is characteristics of free CO_2 due to the background of the measurement system or reaction process (9). Presence of these characteristic bands is a proof of the CaO powder formed.
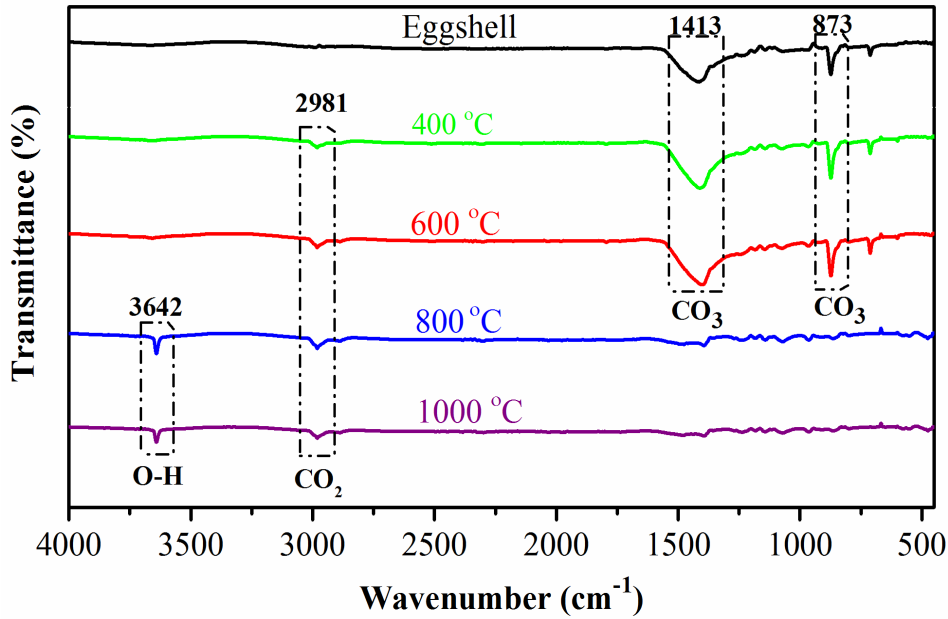
Figure 1. FTIR analysis of waste eggshell and CaO powders synthesized at 400, 600, 800 and 1000 °C.

$CaCO_3$, the main component of the eggshell, can completely decompose in CaO and CO_2 with the increase in calcination temperature (10). In this study, eggshells were calcined in an ash furnace at 400, 600, 800 and 1000 °C, respectively to evaluate the effect of calcination temperature on formation of CaO. Thermal analysis of the waste eggshell was performed to determine the optimum calcination temperature (Figure 2). The weight decrement during the heating process was determined by TGA. The CaO content in the eggshells were determined as about 49% (w/w). With the increase in temperature from 600 to 800 °C, a significant weight loss has occurred because of the CO_2 molecules moving up from the structure of eggshell. The $CaCO_3$ decomposes completely into CaO at a maximum temperature of 760 °C.

Beside the thermal analysis of waste eggshell, DLS analyser measurements were made to observe the effect of the calcination temperature on the particle size of the synthesized CaO. Figure 3 shows the variation of CaO powder size as a function of calcination temperature of eggshells. It reveals that increasing the calcination temperature results in smaller size of CaO powder which was in close agreement with the (11). At the calcination temperature of 800 the particle size was 103.5496 nm. The calcination temperature was chosen as 800 °C for the synthesis of bio-HAp.
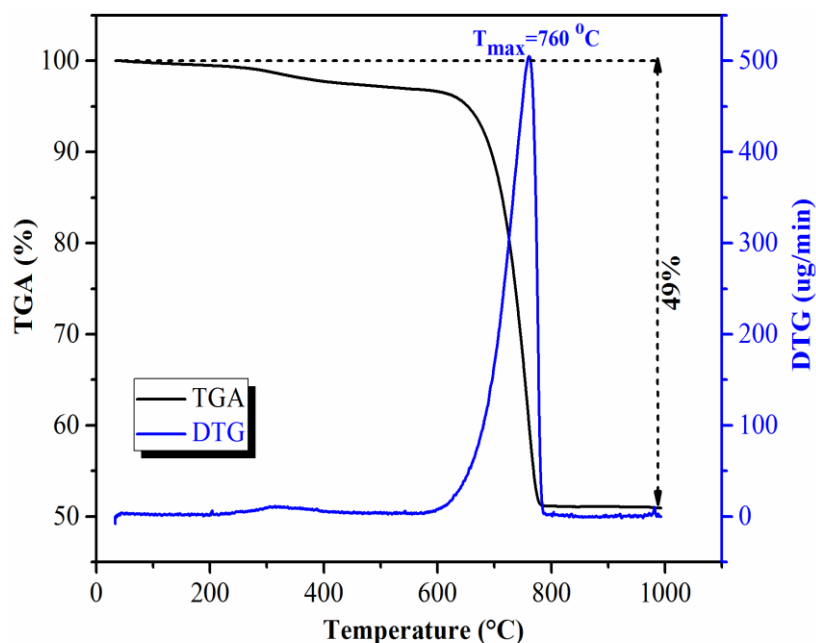
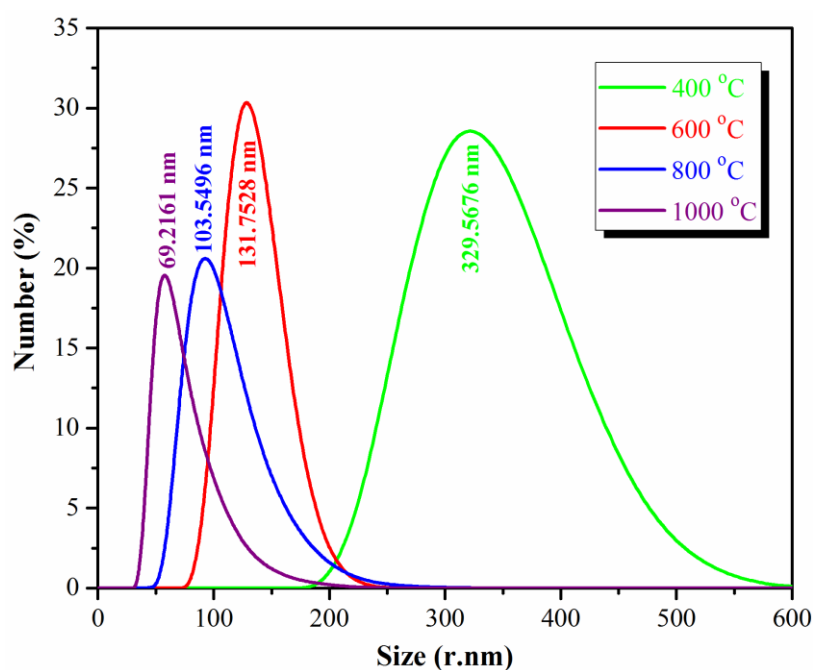**Figure 2.** TGA and DTG curves of waste eggshell.

Figure 3. Particle size distribution of CaO powders synthesized at 400, 600, 800 and 1000 °C.

Characterization of Bio-Hap

FTIR analysis was performed to compare the functional groups of bio-HAp and commercially purchased hydroxyapatite (com-HAp). The FTIR spectrum of the bio-HAp was chemically in good agreement with the spectrum of com-HAp and the FTIR spectrum reported by another study that demostrated HAp powder synthesized from hen eggshells (12). The band at 1027 cm^{-1} is the characteristic band of phosphate (PO_4) stretching vibration whereas the bands at 562 and 501 cm^{-1} are due to phosphate bending vibration (13). According to spectral data, the absorption

peak at 1412 cm^{-1} corresponds to the asymmetric stretching of carbonate ion substitution. FTIR spectra indicated that bio-HAp was successfully derived from CaO calcined at 800 °C.

The particle size distribution of bio-HAp and com-HAp samples was analysed (Figure 5). The average size of bio-HAp was 33.08 nm while the size of com-HAp was 115.98 nm. The polydispersive index (PDI) of samples were 0.462 and 0.722, respectively. This PDI value showed that the synthesized sample was homogeneous and uniform in size (14). Moreover, DLS analysis showed that the synthesized bio-HAp was in the nanometer size.
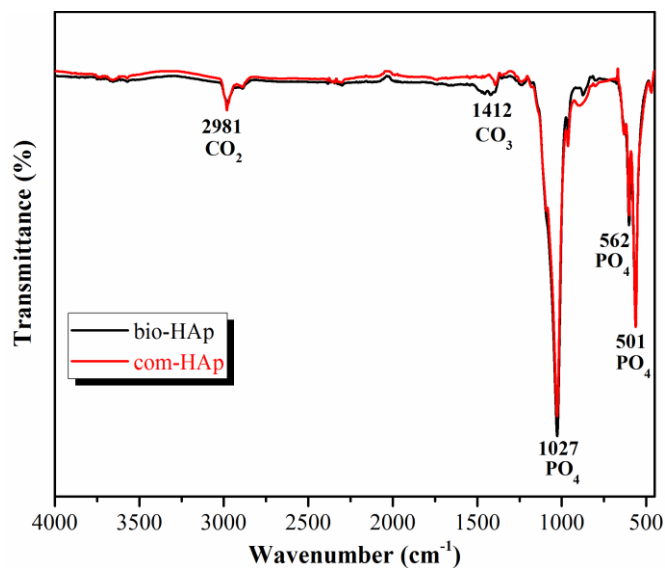

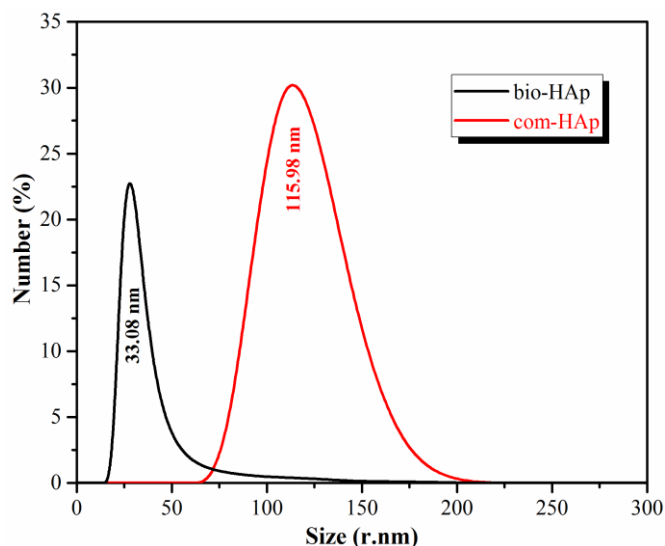**Figure 4.** FTIR analysis of com-HAp and bio-Hap.

Figure 5. Particle size distribution of com-HAp and bio-Hap.

Characterization of Chitosan-Hap Cryogels

The ratio of bio-HAp to chitosan solution was varied in this study. The amount of bio-HAp affected the chemical, physical, mechanical, morphological and porous structure of cryogels. Figure 6

shows the photograph of chitosan-HAp cryogels after cryogelation reaction is completed (in wet form) and after lyophilization (in dry form). The colour of cryogels including bio-Hap were more opaque than the plain chitosan cryogel. Also with increasing the amount of bio-HAp in the chitosan cryogels, a more smooth and elastic surface was reached.

Furthermore, FTIR analysis demonstrated the functional groups of bio-HAp, interactions between bio-HAp and chitosan, crosslinking bonds between glutaraldehyde and chitosan. The FTIR spectra of the cryogels, as shown in Figure 7, demonstrated bands corresponding to hydroxyl, phosphate and amine groups. The major absorbance bands of the spectra correspond to hydroxyapatite. Width of bands decreases with increasing bio-HAp content of cryogels (15). With the increase in the amount of bio-HAp a sharp peak was observed at near by 1050 cm^{-1}. This peak shows the interaction of chitosan with the phosphate groups of bio-HAp (16). The bands between 1550-1700 cm^{-1} are attributed to mode superposition of the hydroxyl group of bio-HAp and amide groups of chitosan (15). The hydroxyapatite phosphate bending bands are at 562 cm^{-1}. The broad peak started at 3480 cm^{-1}, gradually decreased and became narrower with the increase in the amount of bio-HAp.

At the cryogelation step, chitosan-HAp cryogels with interconnected pores were obtained. Swelling ability of a cryogel is related with the highly porous and spongy morphology of the cryogels (7). The swelling ratio results of the plain chitosan and chitosan-HAp cryogels are demonstrated in Figure 8. Plain chitosan and all chitosan-HAp cryogels showed a swelling ratio higher than 3000% in the first 5 min. It was observed that as the amount of bio-HAp in the cryogels increased the swelling ratio decreased. The decrease may be due to the decrease in the pore size of the cryogels. As the amount of bio-HAp increased the pore walls of the cryogels were filled with more bio-Hap. Plain chitosan cryogel showed the highest swelling ratio (8660.43%) after 60 minutes of swelling time.
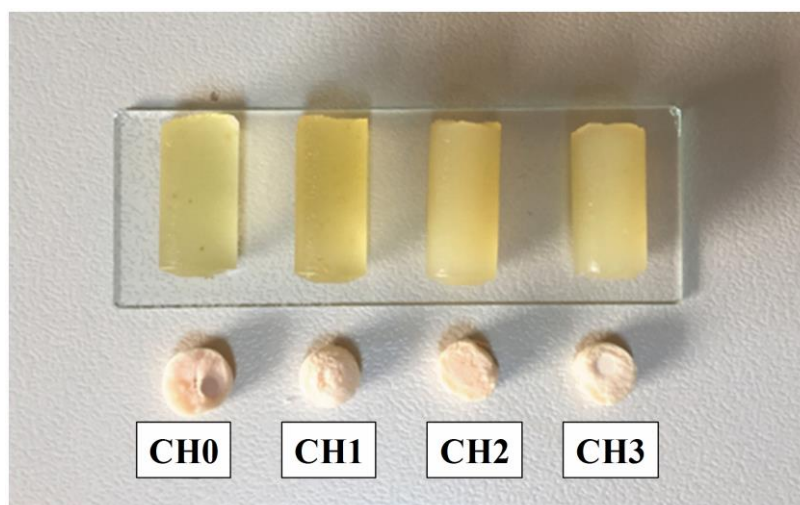

Figure 6. Photograph of blank chitosan and chitosan-HAp cryogels in wet and dry form (CH0= plain chitosan, CH1=1:1, CH2= 1:2, CH3= 1:3 (chitosan:HAp))
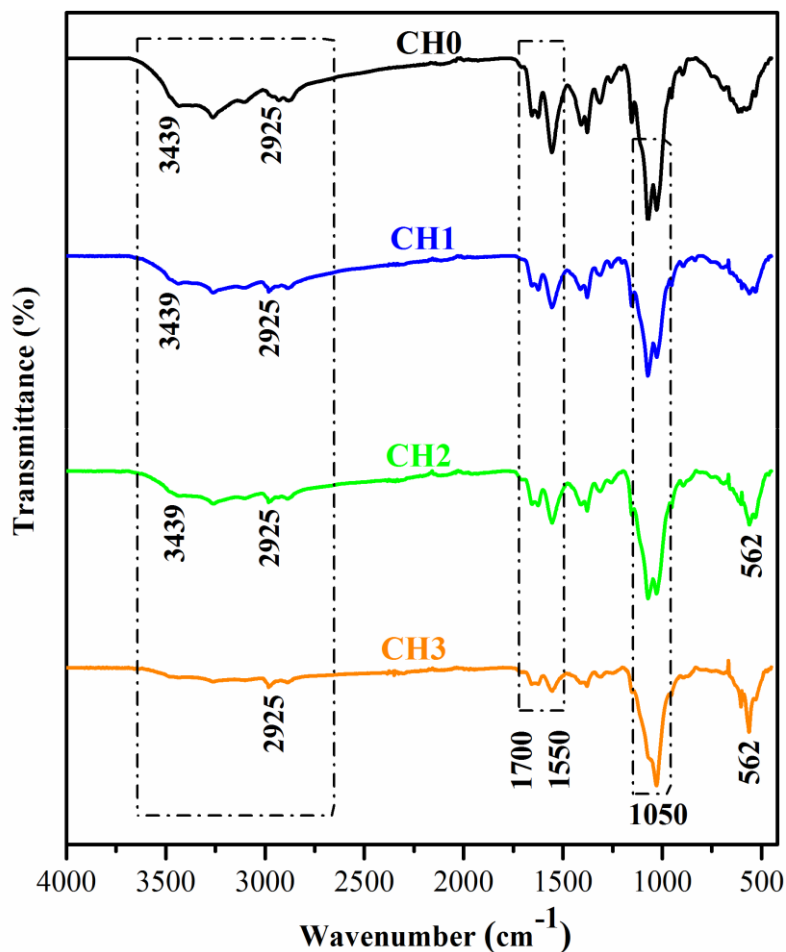
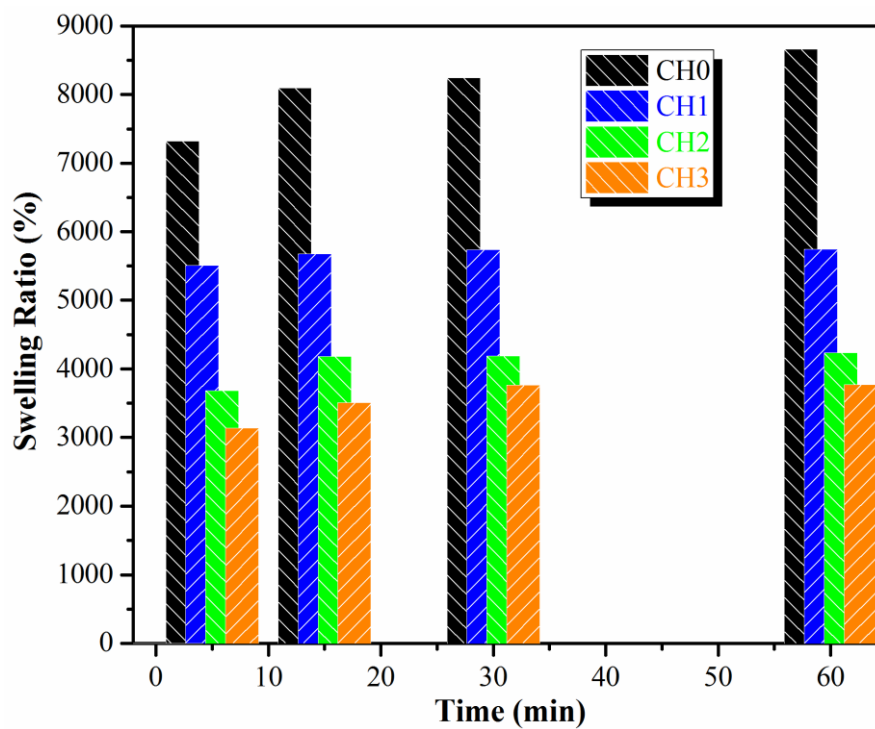**Figure 7.** FTIR analysis of plain chitosan and chitosan-HAp cryogels.

Figure 8. Swelling ratio analysis of plain chitosan and chitosan-HAp cryogels.

85

CONCLUSION

CaO powder was produced by using domestic waste eggshells through a calcination process at different temperatures. Pure bio-HAp was synthesized by co-precipitation method using the CaO powder which was calcined at 800 °C. The particle size of the synthesized bio-HAp was measured as in nano scale. FTIR analysis showed the purity of bio-HAp. This process can lead to the development of a cost effective biomaterial and can improve waste management in future. Chitosan cryogel scaffolds reinforced with bio-Hap were successfully produced for possible tissue engineering applications. Hence, from the results, it can be concluded that the synthesized bio-HAp can be economically produced from waste eggshells by a simple calcination and co-precipitation method for wide range of biomedical applications especially for tissue engineering. The bio-HAp reinforced chitosan cryogel biocomposites can be potential scaffold candidates to be used in possible tissue regeneration.

CONFLICT OF INTEREST

The authors declare that no conflict of interest occurred in this work.

REFERENCES

1. Zhou H, Lee J. Nanoscale hydroxyapatite particles for bone tissue engineering. Acta Biomaterialia. 2011 Apr; 7(7): 2769-81.

2. Brzezińska-Miecznikn J, Haberko K, Sitarz M, Bućko MM, Macherzyńska B. Hydroxyapatite from animal bones-Extraction and properties. Ceramics International. 2014 Dec; 41(3): 4841-46.

3. Rasool T, Ahmed SR, Ather I, Sadia M, Khan R, Jafri AR. Synthesis and Characterization of hydroxyapatite using egg-shell. 2015 Nov; 3: 1-6. (Digests ASME 2015 International Mechanical Engineering Congress and Exposition, Texas 2015).

4. Wu SC, Hsu HC, Hsu SK, Chang YC, Ho WF. Synthesis of hydroxyapatite from eggshell powders through ballmilling and heat treatment. Journal of Asian Ceramic Societies. 2015 Dec; 4(1): 85-90.

5. Mittal A, Teoti M, Soni RK, Mittal J. Applications of egg shell and egg shell membrane as adsorbents: A review. Journal of Molecular Liquids. Aug 2016; 223: 376-87.

6. Padmanabhan SK, Salvatore L, Gervaso F, Catalano M, Taurino A, Sannino A, Licciulli A. Synthesis and characterization of collagen scaffolds reinforced by eggshell derived hydroxyapatite for tissue engineering. Journal of Nanoscience and Nanotechnology. 2015 Sept; 14: 1-6.

7. Demir D, Öfkeli F, Ceylan S, Bölgen Karagülle N. Extraction and characterization of chitin and chitosan from blue crab and synthesis of chitosan cryogel scaffolds. Journal of the Turkish Chemical Society, Section A: Chemistry. 2016 Aug; 3(3): 131-44.

8. Witoon T. Characterization of calcium oxide derived from waste eggshell and its application as CO_2 sorbent. Ceramics International. 2011 May; 37(8): 3291-98.

9. Choudhary R, Koppala S, Swamiappan S. Bioactivity studies of calcium magnesium silicate prepared from eggshell waste by sol-gel combustion synthesis. Journal of Asian Ceramic Societies. in press.

10. Ummartyotin S, Tangnorawich B. Utilization of eggshell waste as raw material for synthesis of hydroxyapatite. Colloid and Polymer Science. 2015 Jun; 293(9): 2477-83.

11. Mornanı EG, Mosayebıan P, Dorranıana D, Behzad K. Effect of calcination temperature on the size and optical properties of synthesized ZnO nanoparticles. Journal of Ovonic Research. 2016 Apr; 12(2): 75-80.

12. Gergely G, We´ber F, Luka´cs I, To´th AL, Horva´th ZE, Miha´ly J, Bala´zsi C. Preparation and characterization of hydroxyapatite from eggshell. Ceramics International. 2009 Oct; 36(2): 803-06.

13. Chaudhuri B, Mondal B, Modak DK, Pramanik K, Chaudhuri BK. Preparation and characterization of nanocrystalline hydroxyapatite from egg shell and K_2HPO_4 solution. Materials Letterr. 2013 Jan; 97: 148-50.

14. Arsad MSM, Lee PM, Hung LK, "Morphology and particle size analysis of hydroxyapatite micro- and nano-particles," pp. 1030-1034, December 2010 (Digests CSSR 2010 Malaysia, 2010).

15. Danilchenko SN, Kalinkevich OV, Pogorelov MV, Kalinkevich AN, Sklyar AM, Kalinichenko TG, Ilyashenko VY, Starikov VV, Bumeyster VI, Sikora VZ, Sukhodub LF, Mamalis AG, Lavrynenko SN, Ramsden JJ. Chitosan-hydroxyapatite composite biomaterials made by a one step co-precipitation method: preparation, characterization and in vivo tests. Journal of Chemical, Biological and Physical Sciences. 2009 Sept; 9(3): 119-26.

16. Manjubala I, Scheler S, Bossert J, Jandt KD. Mineralisation of chitosan scaffolds with nano-apatite formation by double diffusion technique. Acta Biomaterialia. 2005 Sept; 2(1): 75-84.

Preparation and Characterization of TiO₂@SiO₂-Ag Nanospheres Photocatalyst, and Investigation of Its Photocatalytic Activity on Methylene Blue

This article was produced from a poster or oral contribution to the ICAIE Congress, 2017.

Taner Tekin[1], Derya Tekin[2] iD, Hakan Kiziltas[1],*

[1] Atatürk University, Department of Chemical Engineering, 25240, Erzurum, Turkey.
[2] Atatürk University, Department of Metallurgy and Materials Engineering, 25240, Erzurum, Turkey.

Abstract: Titanium dioxide shows a tremendous potential for the decomposition of organic pollutants under UV and visible light irradiation. In this study TiO₂ nanospheres @ mesoporous silica nanospheres (TiO₂@SiO₂) photocatalyst was synthesized by the sol-gel method. The synthesized TiO₂/SiO₂ photocatalyst was decorated by Ag nanoparticle. The decorated TiO₂@SiO₂– Ag photocatalyst by a hydrothermal method was characterized by scanning electron microscope (SEM), energy-dispersive X-ray spectroscopy (EDS) and X-ray diffraction (XRD). The SEM results show that TiO₂@SiO₂–Ag nanospheres photocatalyst was uniformly formed. The EDS analysis proves that the nanospheres photocatalyst consists of Ti, Si, O and Ag. The TiO₂@SiO₂–Ag nanospheres photocatalyst exhibited better photocatalytic performance for degradation of methylene blue under direct UV illumination.

Keywords: Titanium dioxide; Core-Shell; Silver nanoparticles; Silica spheres

Cite this: Tekin T, Tekin D, Kızıltaş H. Preparation and Characterization of TiO2@SiO2-Ag Nanospheres Photocatalyst, and Investigation of Its Photocatalytic Activity on Methylene Blue. Journal of the Turkish Chemical Society, Section B: Chemical Engineering. 1(sp. is. 1):89–96.

*Corresponding author. E-mail: h.kiziltas@atauni.edu.tr

INTRODUCTION

During the recent years, technological developments affect adversely the environment [1]. The degradation of pollutants with photocatalyst gained more interest because of its efficiency and cheapness [2]. One and most used of semiconductor photocatalysts is TiO_2 with an energy band gap because of high surface area, low toxicity and chemical stability [3].

In the last decade, researchers have studied the very different forms of TiO_2 such as nanotube [4,5], nanorods, nanowires, nanospheres. In addition, the noble metal doping is much used way to increase photocatalytic performance of TiO_2 under UV light. The photocatalytic result of hollow microspheres of TiO2 shows advance photocatalytic activity than another forms of TiO_2 [6-8].

In this study, TiO_2 nanoparticles and TiO_2/SiO_2-Ag nanocomposites were synthesized as a photocatalyst. The photocatalysts were characterized by SEM, EDS and XRD. The photocatalytic performance of the photocatalysts was investigated by decomposition of MB solution under UV light.

MATERIALS AND METHODS

Chemicals

Titanium isopropoxide (TIP; Sigma-Aldrich), hydrochloric acid (HCl; Sigma-Aldrich), ethanol (C_2H_6O; Sigma-Aldrich), Cetyltrimethyl ammoniumbromide (CTAB: Sigma-Aldrich), tetraethyl orthosilicate (TEOS; Sigma-Aldrich), ammonium hydroxide (NH_4OH; Sigma-Aldrich), Silver nitrate ($AgNO_3$; Sigma-Aldrich), sodium borohydride ($NaBH_4$; Sigma-Aldrich) and methylene blue (MB; Sigma-Aldrich) were purchased.

Experimental procedure

➢ Synthesis of TiO_2 nanoparticles

Titanium isopropoxide as a precursor dissolved in ethanol, HCl and deionized water mixture, and stirred for one hour. After adding10ml of deionized water in the mixture, the mixture was stirred for 2 hours. The formed TiO_2 nanoparticles were separated by centrifuging proses, dried with deionize water 2 times and dried at 80ºC for 2 hours.

➢ Synthesis of $TiO_2@SiO_2$ nanoparticles

0,1 g of TiO_2 and 0.25 g of CTAB was ultrasonically dissolved in the mixture of 80 ml of ethanol, 60 ml of water and 5 ml of NH_4OH for 20 minutes. 0.25 ml of TEOS was rapidly added in the mixture under the magnetic stirring. After stirring for 2 hours, the formed $TiO_2@SiO_2$

nanoparticles was separated by centrifuged process. The solid product was washed 2 times with ethanol and dried in the oven at 110°C for 18 hours. For removing the CTAB templates, the dried product was refluxed in acetone solution for 8 hours. Then, the product was filtered and dried in the oven.

➢ Synthesis of $TiO_2@SiO_2$-Ag nanoparticles

0.1 gr of synthesized $TiO_2@SiO_2$ nanoparticles was added in 100 ml of deionized water under magnetic stirring. The $AgNO_3$ solution was added and stirred towards the reduction of Ag ions upon the dropwise addition of $NaBH_4$ until the color changed to greenish yellow. The solution was stirred for 1 hour. Then formed $TiO_2@SiO_2$–Ag nanostructures were centrifuged, washed with deionized water 5 times, dried at 70°C for 2 hours, and calcined at 500°C for 2 hours.

➢ Characterization

The produced nanospheres photocatalysts were characterized by SEM, EDS and XRD. The surface morphology was investigated by SEM with coated a thin layer Au to prevent the charge problem. The composition of nanospheres was determined by EDS analysis. The structural and phase identification of the nanospheres were investigated by XRD in the 2 theta range from 20 to 80 degree.

➢ Evaluation of Photocatalytic Activity

The photocatalytic activity performance of the prepared nanospeheres photocatalysts was investigated on the decomposition of MB solution. Degradation of MB solution was performed in the jacketed reactor at room temperature. The photocatalytic experiment was carry out by 25 mg of the prepared nanospheres photocatalysts with 200 ml of a solution consisting of 20 mg. L^{-1} of MB. The MB aqueous was irritated by UV-light at 254 nm ($44W/m^2$). The saturated O_2 concentration in the reaction medium was provided by air-pump. The quantitative analysis of MB concentration was determined by withdrawing 2 ml of samples from the reactor solution and measuring in UV-vis spectrophotometer.

RESULTS AND DISCUSSION

As shown in Figure 1, the surface morphology of the prepared nanospheres was investigated by SEM. The TiO_2, $TiO_2@SiO_2$-Ag nanoparticles show spherical shape with uniform structure, as shown Figure 1a-c. The TiO_2 disorderly form and agglomeration in Figure 1a. The surface of $TiO_2@SiO_2$ nanospheres shows smoothness because of coating with thin SiO_2 layer in Figure 1b. The SEM image of the $TiO_2@SiO_2$-Ag photocatalyst demonstrates porous and rough structure, which is increasing the photocatalytic activity with more active areas.

The EDS results present the presence of Ag, O, Si and Ti in the composition of $TiO_2@SiO_2$-Ag, as shown Figure 1d.

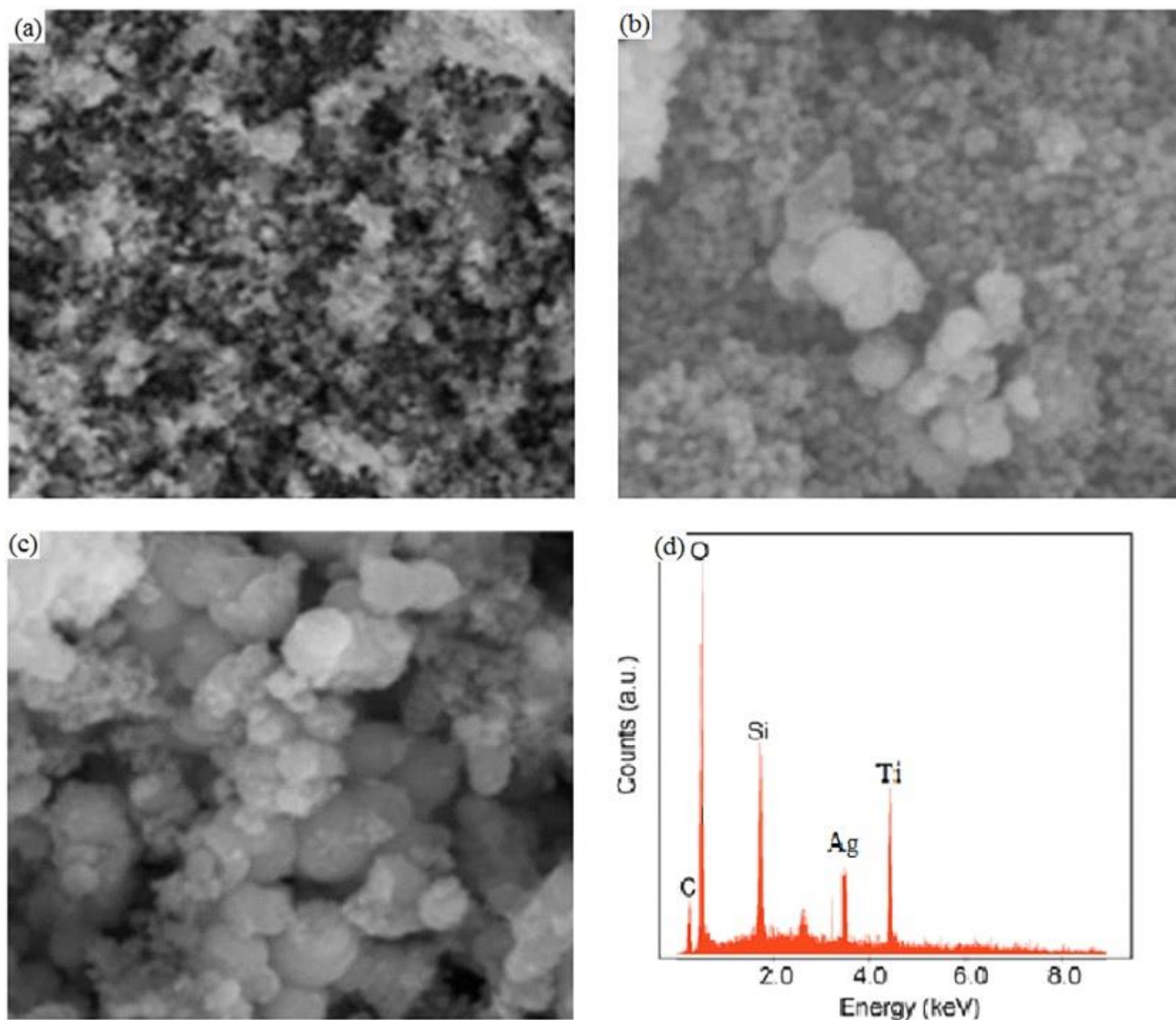**Figure 1.** SEM images of TiO_2 (a), $TiO_2@SiO_2$ (b), and $TiO_2@SiO_2$-Ag nanocomposites (c), and EDS result of $TiO_2@SiO_2$-Ag (d).

The TiO_2 and $TiO_2@SiO_2$ nanoparticles show the similar diffraction peaks with the anatase phase of TiO_2. Ag NPs on the $TiO_2@SiO_2$ nanocomposite matrix at diffraction peaks values of 38.2 and 44.2 corresponding to the (111) and (200) diffraction plans of the face centered cubic Ag crystals as shown in Figure 2.
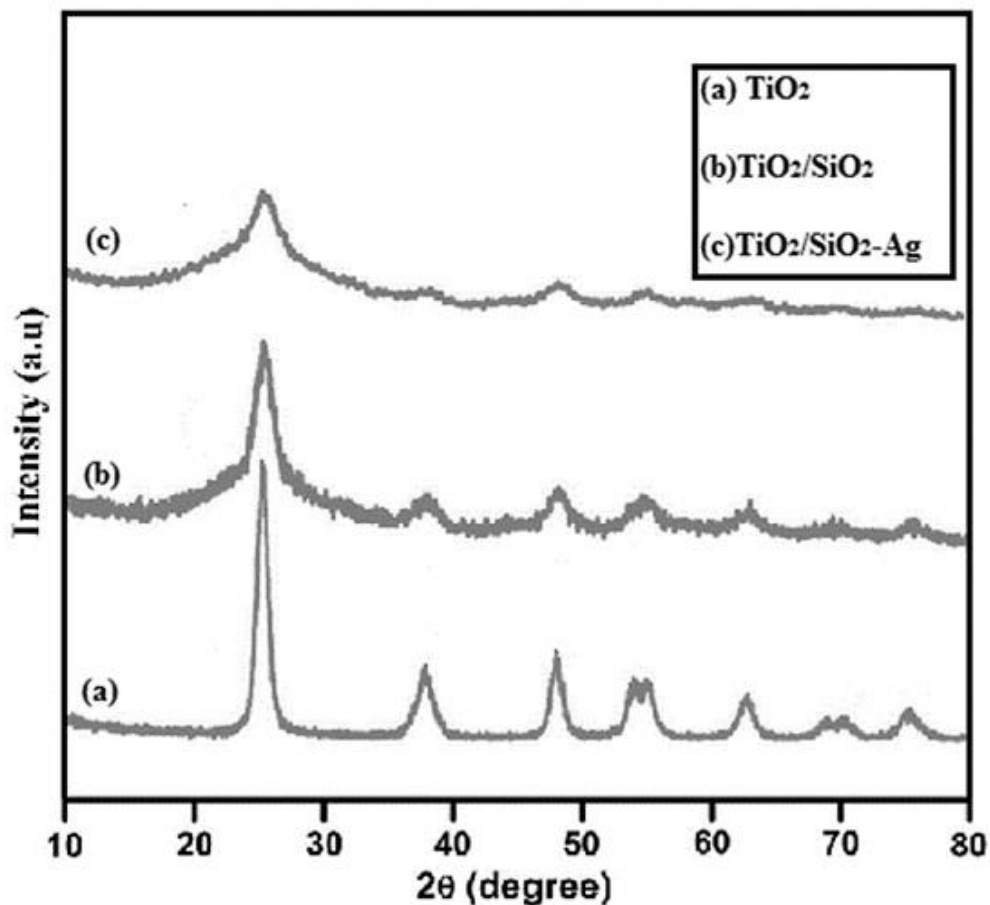
Figure 2. XRD pattern of Photocatalyst

The photocatalytic performance of $TiO_2@SiO_2$-Ag nanospheres was commentated by measuring the degradation of MB solution. Degradation of MB solution is not determined in the absent of photocatalyst or in the dark environment. The photocatalytic performance of $TiO_2@SiO_2$-Ag nanospheres is higher than commercial TiO_2 photocatalyst. The results of the degradation of MB solution for different photocatalysts are given in Figure 3.
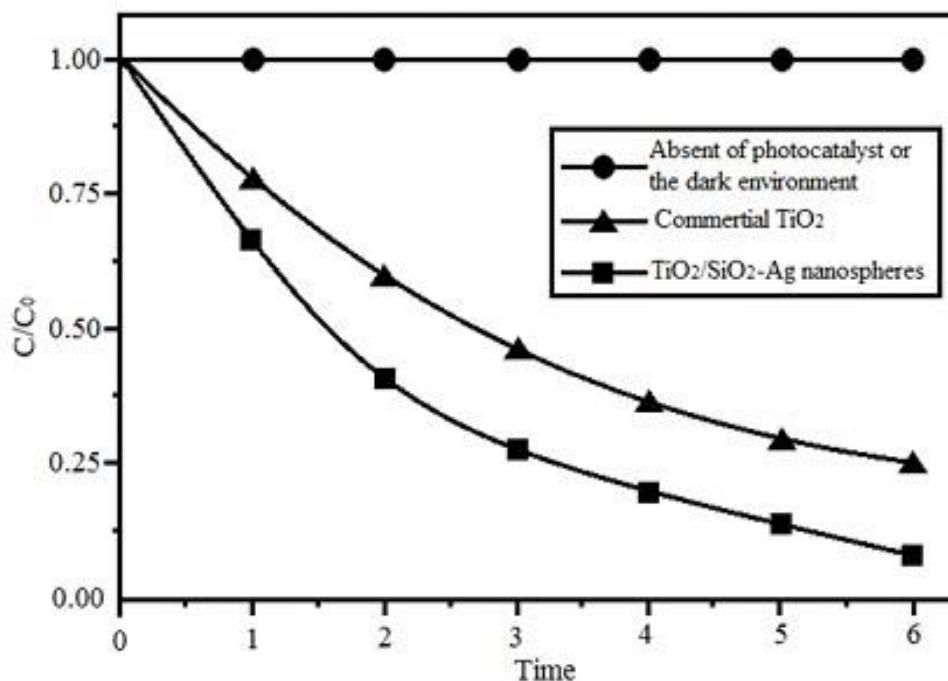
Figure 3. Degradation of MB solution

CONCLUSIONS

The TiO$_2$@SiO$_2$-Ag nanospheres were synthesized by sol-gel method. The TiO$_2$@SiO$_2$–Ag nanospheres show excellent structure and high surface area. The photocatalytic performance of the synthesized nanospheres was investigated by decomposition of Methylene Blue solution. The TiO$_2$@SiO$_2$-Ag photocatalyst showed a better photocatalytic activity then the commercial in solution of Methylene Blue.

REFERENCES

1. Ndong LBB, Ibondou MP, Gu X, Lu S, Qiu Z, Sui Q, Mbadinga SM. Enhanced Photocatalytic Activity of TiO2 Nanosheets by Doping with Cu for Chlorinated Solvent Pollutants Degradation. Industrial & Engineering Chemistry Research. 2014 Jan; 53(4):1368–1376.

2. Lam SM, Sin JC, Abdullah AZ, Mohamed AR. Photocatalytic TiO2/Carbon Nanotube Nanocomposites for Environmental Applications: An Overview and Recent Developments. Fullerenes, Nanotubes and Carbon Nanostructures. 2013 Mar; 22(5):471–509.

3. Mendonca VRD, Mourao HAJL, Malagutti AR, Ribeiro C. The Role of the Relative Dye/Photocatalyst Concentration in TiO2 Assisted Photodegradation Process. Photochemistry and Photobiology. 2013 Oct; 90(1):66–72.

4. Wang DH, Jia L, Wu XL, Lu LQ, Xu AW. One-step hydrothermal synthesis of N-doped TiO2/C nanocomposites with high visible light photocatalytic activity. Nanoscale. 2012 Sep; 4(2):576–584.

5. Singh S, Singh PK, Mahalingam H. Novel Floating Ag+-Doped TiO2/Polystyrene Photocatalysts for the Treatment of Dye Wastewater. Industrial & Engineering Chemistry Research. 2014 Sep; 53(42): 16332–16340.

6. Rayalu SS, Jose D, Mangrulkar PA, Joshi M, Hippargi G, Shrestha K, Klabunde K. Photodeposition of AuNPs on metal oxides: Study of SPR effect and photocatalytic activity International Journal of Hydrogen Energy. 2014 Mar; 39(8):3617–3624.

7. Yang X, Cui H, Li Y, Qin J, Zhang R, Tang H. Fabrication of Ag3PO4-Graphene Composites with Highly Efficient and Stable Visible Light Photocatalytic Performance. ACS Catalysis. 2013 Jan; 3(3):363–369.

8. Neppolian B, Bruno A, Bianchi CL, Ashokkumar M. Graphene oxide based Pt–TiO2 photocatalyst: Ultrasound assisted synthesis, characterization and catalytic efficiency Ultrasonics Sonochemistry. 2012 Jan; 19(1):9–15.